A PHYSICAL AND NUMERICAL MODEL STUDY OF THE STATE OF STRESS AND DEFORMATION ASSOCIATED WITH LARGE SCALE FRACTURE ROUGHNESS

STEPHEN DOUGLAS BUTT

A PHYSICAL AND NUMERICAL MODEL STUDY OF THE STATE OF STRESS AND DEFORMATION ASSOCIATED WITH LARGE SCALE FRACTURE ROUGHNESS

by

© Stephen Douglas Butt, B. Eng.

A thesis submitted to the School of Graduate Studies

in partial fulfilment of the requirements for the degree of

Master of Science

Department of Earth Sciences

Memorial University of Newfoundland

St. John's, Newfoundland

1994

ISBN 0-315-91633-8

Canada

Abstract

The focus of this research study was to quantify the influence of a single large scale fracture roughness asperity on the fracture stiffness and displacement, the local stress field in adjacent wall rock and on the mode and patterns of any induced secondary fractures under various states of applied stress. This was accomplished through the use of a discrete fracture numerical modelling code and experiments on an instrumented high strength concrete model of a fracture plane in a stiff biaxial loading frame.

Initial numerical modelling was completed to determine a suitable asperity morphology for the physical model. Laboratory experiments were conducted on test specimens to determine the material characteristics of the intact concrete and the simulated fracture for input into the numerical model and to measure the 0 to 40 kHz acoustic emission signature of induced fracturing. Nonlinear numerical modelling was completed to predict internal stresses in the concrete model during two normal and two shear loading cycles and to predict modes and patterns of secondary fracturing. The concrete sample was subsequently tested under three normal and three shear loading cycles. Strain gauges cast into the concrete model measured the internal strain field. Displacement transducers mounted on the model measured average fracture displacements and an accelerometer monitored acoustic emissions. The sample macroscopically failed at the peak of the final shear loading cycle and was impregnated with a low viscosity resin to enable "post mortem" analysis of secondary fracturing.

Results of the study confirmed that the large scale asperity had a significant influence on the local stress field and that several forms of enhanced fracture porosity were associated with plastic and brittle deformation near the asperity. Comparisons between the numerically predicted and experimentally measured stress fields showed that the uniformity of fracture mating about the asperity and secondary fracturing significantly influenced the measured strain field and the accuracy of the numerical predictions. Finally, measured patterns of induced secondary fracturing were very similar to those predicted from results of the numerical modelling.

Acknowledgements

The completion of the research outlined in this thesis has involved the guidance, support and assistance of numerous individuals and organizations whom I would now like to acknowledge. First of all, I would like to thank my supervisor, Professor John Gale, who provided the initial concept for and directed the research. Professor Gale provided guidance, feedback and also assisted in the assembly and testing of the physical model. I would like to thank Alison Pye, Research Assistant, for assistance throughout all stages of laboratory work during this investigation, including development of the high strength concrete mix and assembly and testing of all concrete models. I would like to thank Peter Lemessurier, Research Engineer, for assistance during assembly and testing of the physical model, particularly for his help in resin injection. I would like to thank fellow graduate students Graham Dillabough, Richard Schaefer and James Slade for assistance during testing of the physical model. I would like to thank Austin Bursey, Engineering Technician, for all of his technical advice and for the loan of data acquisition equipment. Finally, I would like to thank Michelle von Schilling who assisted in data reduction, in the preparation of figures and who proofread the text.

I would like to thank the Government of Newfoundland and Labrador, Department of Education and the School of Graduate Studies for providing me with much welcomed financial support, in the form of two Atlantic Accord Graduate Fellowships, without which I could not have completed this thesis.

Finally, this thesis study was part of an overall research project, headed and directed by Dr. J. E. Gale, examining the impact of fractures on enhanced hydrocarbon recovery from fractured reservoirs and was funded by Supply and Services Canada for Center for Mineral and Energy Technology, Shell Canada Research, Hibernia Management Development Corporation, Fracflow Consultants Inc. and Imperial Oil Limited with additional funding provided by an NSERC operating grant to Dr. J. E. Gale. Thanks are extended to these organizations for funding this research.

Table of Contents

Abstract ii
Acknowledgements iii

List of Figures vii
List of Tables xi
List of Symbols and Abbreviations xii

Chapter 1 - Introduction
- 1.1 Statement of Problem 1
- 1.2 Research Scope and Objectives 2
- 1.3 Previous Research 3

Chapter 2 - Numerical Modelling
- 2.1 Finite Element Code 14
- 2.2 Finite Element Mesh Geometry 15
- 2.3 High Strength Concrete and Simulated Fracture 18
- 2.4 Experimental Determination of Material Properties 19
  - 2.4.1 Concrete Elastic Constants and Fracture Stiffnesses 19
  - 2.4.2 Concrete Strength 24
  - 2.4.3 Acoustic Emission Signature of Brittle Deformation 25
- 2.5 Predictive Numerical Modelling 28

Chapter 3 - Biaxial Physical Modelling
- 3.1 Construction of Physical Model 43
- 3.2 Experimental Procedure and Data Reduction 48
- 3.3 Analysis of Biaxial Testing Results 53
  - 3.3.1 Normal Loading Cycles 53
  - 3.3.2 Shear Loading Cycles 65
- 3.4 Post Mortem Sectioning 76

Chapter 4 - Discussion, Conclusions and Recommendations
- 4.1 Discussion of Results 80
- 4.2 Comparison of Physical Measurements to Numerical Predictions 83
- 4.3 Conclusions 91
- 4.4 Recommendations for Future Work 93

Bibliography 95

Appendix A - Vertical and Horizontal Stress Results From Numerical Modelling of Large Scale Fracture Roughness 99

Appendix B - Design, Testing and Calibration of MUGS Strain Measurement System
B-1 MUGS System Design and Operation 108
B-2 Testing of MUGS System 111
B-3 Strain Gauge Calculation Procedure 112

Appendix C - Numerical Loading Control Software Algorithm 115

Appendix D - Strain Gauge Correction Procedures
D-1. Filtering of MUGS Strain Gauge Records 117
D-2. Removal of Self Warming Response From HP Strain Gauge Records 119

Appendix E - Strain Gauge Positions in the Physical Model 122

Appendix F - Tabulated Strain Gauge and Numerical Modelling Data 125

List of Figures

Figure 1-1. Asperity morphology, adapted from Scholtz (1990) 7

Figure 1-2. Stress field near a rough fracture undergoing right lateral shear 7

Figure 1-3. Results of a photoelastic study of natural rough joint surfaces 8

Figure 1-4. Experimentally observed failure modes of high angled asperity during non dilatant shear 13

Figure 1-5. Experimentally observed failure mode of high angled asperity during dilatant shear 13

Figure 2-1. Finite element mesh geometry and boundary conditions for large scale roughness model 16

Figure 2-2. Final large scale roughness morphology used for both predictive numerical modelling and physical model 17

Figure 2-3. Position of instrumentation on intact and fractured 152 mm diameter samples 26

Figure 2-4. Axial and diametrical strain recorded during nondestructive uniaxial compression loading of intact 152 mm diameter sample 26

Figure 2-5. Normal stress versus normal closure curves from nondestructive uniaxial testing of fractured 152 mm diameter sample 27

Figure 2-6. Plots of uniaxial stress and acoustic emission counts versus uniaxial strain recorded during destructive testing of intact 152 mm diameter sample 27

Figure 2-7(a). Mean stress contours for the first modelled normal loading cycle 31

Figure 2-7(b). Maximum shear stress contours for the first modelled normal loading cycle 32

Figure 2-8(a). Mean stress contours for the second modelled normal loading cycle 33

Figure 2-8(b). Maximum shear stress contours for the second modelled normal loading cycle 34

Figure 2-9(a). Mean stress contours for the first modelled shear loading cycle at 2 MPa normal stress 36

Figure 2-9(b). Maximum shear stress contours for the first modelled shear loading cycle at 2 MPa normal stress 37

Figure 2-10(a). Mean stress contours for the second modelled shear loading cycle at 8 MPa normal stress 38

Figure 2-10(b). Maximum shear stress contours for the second modelled shear loading cycle at 8 MPa normal stress 39

Figure 2-11. Tensile stress contours for the modelled shear loading cycles at peak shear 40

Figure 2-12. Plots of major and minor principal stress vectors at peak shear 40

Figure 2-13. Mode, orientation and location of predicted secondary fractures at peak shear 42

Figure 3-1. Geometry of concrete coupons with respect to final simulated fracture and positions of strain gauges on the coupons 44

Figure 3-2. Construction of physical model 46

Figure 3-3. Plots of normal stress versus normal displacement for each of the three normal cycles and the normal loading portions of the shear loading cycles 54

Figure 3-4(a). Contours of vertically oriented strain recorded during the first normal loading cycle 56

Figure 3-4(b). Contours of horizontally oriented strain recorded during the first normal loading cycle 57

Figure 3-5(a). Contours of vertically oriented strain recorded during the second normal loading cycle 60

Figure 3-5(b). Contours of horizontally oriented strain recorded during the second normal loading cycle 61

Figure 3-6(a). Contours of vertically oriented strain recorded during the third normal loading cycle 62

Figure 3-6(b). Contours of horizontally oriented strain recorded during the third normal loading cycle 63

Figure 3-7. A schematic diagram proposing that non uniform fracture mating at the right hand asperity bend caused by the asymmetrical strain patterns observed during normal loading 64

Figure 3-8. Plots of shear stress versus shear displacements for each of the three shear loading cycles. Plotted above the curve for the third shear cycle is the square root of the AE measured during that cycle 65

Figure 3-9(a). Contours of vertically oriented strain recorded during the shear portion of the first shear loading cycle 69

Figure 3-9(b). Contours of horizontally oriented strain recorded during the shear portion of the first shear loading cycle 70

Figure 3-10(a). Contours of vertically oriented strain recorded during the shear portion of the second shear loading cycle 72

Figure 3-10(b). Contours of horizontally oriented strain recorded during the shear portion of the second shear loading cycle 73

Figure 3-11(a). Contours of vertically oriented strain recorded during the shear portion of the third shear loading cycle 74

Figure 3-11(b). Contours of horizontally oriented strain recorded during the shear portion of the third shear loading cycle 75

Figure 3-12. A schematic diagram proposing the basic fracture behaviour which resulted in the characteristic strain patterns observed during the second and third shear cycles 77

Figure 3-13. Sketches of profile sections through the resin impregnated sample after macroscopic shear failure 79

Figure 4-1. Comparison of the predicted stresses at τ = 4.60 MPa and the measured strains at τ = 7.8 MPa for the second shear loading cycle for (a) horizontal orientation and (b) vertical orientation 87

Figure 4-2. Mohr-Coulomb failure diagram explaining why the model did not macroscopically as anticipated, even though both predicted and measured maximum compressive stresses exceeded the uniaxial compressive strength of the concrete 90

List of Tables

Table 2-1. Values of Young's Modulus and Poisson's Ratio determined from first loading cycle of intact cylindrical sample 22

Table 2-2. Normal stiffness values determined over linear intervals of normal stress versus closure curves 22

Table 2-3. Shear stiffness values determined over linear intervals of shear stress versus shear displacement curves at normal stresses of 2 MPa and 8 MPa 23

Table 2-4. Approximate shear stiffness determined over normal stress intervals 23

Table 2-5. Stress increments and material properties used during numerical simulation of first and second normal loading cycles 30

Table 2-6. Stress increments and material properties used during numerical simulation of first and second shear loading cycles 35

List of Symbols and Abbreviations

AE	Acoustic Emissions
ASTM	American Society for Testing of Materials
ISRM	International Society for Rock Mechanics
$E_{material}$	Young's Modulus of material (e.g. steel, concrete, epoxy)
JCS	Joint Wall Compressive Strength
JRC	Joint Roughness Coefficient
K_{normal}	Normal stiffness of fracture
$K_{tangential}$	Tangential stiffness of fracture
kHz	Kilohertz
LVDT	Linear Voltage Displacement Transducer
$\nu_{material}$	Poisson's Ratio of material (e.g. steel, concrete, epoxy)
MPa	MegaPascal
ϕ	Internal angle of friction
ϕ_r	Residual friction angle of fracture
σ_N	Fracture normal stress
σ_{max}	Major principal stress
σ_{mean}	Mean stress
σ_{min}	Minor principal stress
T	Shear strength of fracture, Barton-Bandis failure criterion
τ	Shear stress on mean fracture plane
τ_{max}	Maximum shear stress - solid rock
μm	Micrometer (micron)
$\mu\epsilon$	Microstrain

Chapter 1 - Introduction

1.1 Statement of Problem

Deformation within the upper brittle region of the Earth's crust often results in the formation of fractures. Fractures come in at least two forms; joints, which have little or no shear displacement, and faults, which can have appreciable shear displacement (Price, 1966). Joints result from the action of tensile stresses and usually occur in groups called sets with approximately regular spacing and orientation. Faults more often occur as single features along which considerable displacement can be accommodated. Fractures serve as major pathways for fluid movement through rock masses, particularly in those rocks with low matrix permeability, as evidenced by observed hydrothermal alteration of wall rock adjacent to fractures and by the presence of fracture infilling vein minerals and associated fluid inclusions. All fractures have some degree of roughness or deviation from a smooth plane. This roughness can result in stress fields that are locally heterogeneous. These stress fields may influence the permeability of adjacent wall rock by the creation of subsidiary fractures or the dilation of existing fractures. This, in turn, will control the movement of fluids transported along fractures into the adjacent wall rock and influence possible sites of hydrothermal mineralization or hydrocarbon accumulation.

This study involves numerical and physical modelling of a single idealized large scale roughness asperity to determine the influence of this feature on the local stress

field, the modes and positions of induced secondary fractures and the overall effect on fracture stiffness and displacement. Results of this work may, in turn, be used to infer the potential influence of large scale fracture roughness on adjacent wall rock permeability.

1.2 Research Scope and Objectives

Numerical modelling of the idealized large scale fracture roughness was conducted using geometric scales and material properties that approximated those planned for the proposed physical model. This was done to evaluate proposed morphologies for the fracture plane. Preliminary laboratory experiments were conducted to determine the material properties of the concrete used to form the physical model and the simulated fracture surface. These material properties were then incorporated into numerical models to provide a detailed prediction of the physical model behaviour. Modification of material properties during these simulations was accomplished through the use of residual stress files and was conducted to approximate the nonlinear response of the concrete and simulated fracture.

The final fracture morphology was incorporated into a concrete model for biaxial testing. The concrete mix was designed to produce high strength, small grain size and low porosity. The simulated texture of the fracture was achieved by casting a woven geotextile between successive concrete pours. Strain gauges were cast into the concrete to delineate the strain field surrounding the fracture asperity at progressive stages of

applied normal and shear stress and an accelerometer was attached to the sample to monitor the acoustic emissions generated by microcracking and secondary fracturing. Finally, at peak shear stress, a low viscosity resin was injected into the fracture plane to preserve the state of secondary fracturing, which was mapped during a post mortem sample sectioning.

The objective of this investigation was to accurately delineate the state of stress associated with large scale fracture roughness using combined numerical and physical models, to determine the modes and timing of secondary fracturing with respect to the applied stress field, and to evaluate the overall influence of a single large scale roughness asperity on fracture stiffness and displacement.

1.3 Previous Research

Previous numerical, laboratory and field investigations on the effects of large scale fracture roughness on the stress and deformation in adjacent wall rock have been conducted by three main groups of researchers. These include rock mechanics scientists specifically examining the stresses and deformation induced by fracture roughness, structural geologists studying the initiation, growth and evolution of natural fractures and engineers studying rough contacts between steel, rock and/or concrete. Because of this, the terminology used to describe fracture morphology and deformation is quite varied. This review, however, adopts a single nomenclature which is used consistently throughout this investigation.

All fracture surfaces display some variation from an ideal planar surface, usually referred to as roughness. Joint roughness is largely controlled by the grain size of the intact rock as the propagating discontinuity often follows grain or crystal boundaries. Fault roughness is a product of formation and growth since many faults are created by the formation of en echelon tensile or shear fractures which are then crosscut by connecting fractures, forming a characteristic asymmetric sawtooth pattern (Segall and Pollard, 1983; Petit, 1987; Deng et al., 1986). Lee et al. (1990) studied joint profiles with Joint Roughness Coefficients (Barton et al. 1985) values ranging from 0 to 20 and concluded that they were fractal surfaces, i.e. they had similar degrees of roughness at all scales of measurement. Power et al. (1987) completed a similar study of fault profiles which indicated that roughness was attenuated parallel to the direction of shear, probably resulting from frictional wear of opposing fault surfaces with accumulated displacement. In either case, it can be concluded that all fractures have some degree of roughness.

Large scale roughness refers to fracture surface variation which is greater than the scale of the width of the fracture. Small scale roughness, on the other hand, refers to variation which is at the same scale or smaller than the width of the fracture and plays an important role in rock friction (Byerlee, 1978). Large scale roughness features of joints are often referred to as asperities (Goodman, 1976) while, on fault planes, they are commonly referred to as jogs (Scholtz, 1990). The difference is mainly one of mechanical emphasis; asperity simply refers to general roughness, while a jog refers to

a kink in a fault which can impede slip or otherwise accumulate stress. Since asperity is a more generic term and is more commonly used in engineering studies, it is used in this investigation to refer to large scale roughness features.

The basic morphology of the asperity is adopted from Scholtz's (1990) categorization of fault jogs since his terms impart a mechanical as well as a morphological connotation. Regions of the asperity that form a non zero angle to the mean fracture plane are referred to as bends, while regions of the asperity that are parallel to the mean fracture plane are referred to as steps. This morphology is given in Figure 1-1. Bends that are compressed due to the orientation of the applied stress field are referred to as restraining, while those that are extended are referred to as releasing. Restraining bends are significant since they must be either overridden or sheared through to enable continued shear displacement and are associated with increased compressive normal stresses. Releasing bends are often associated with increased tensile stresses and may show dilation.

Stress heterogeneity near rough fractures has been observed or inferred in numerous experimental and field investigations. Fishman (1990) used a photoelastic technique to study the state of stress near a rough fracture with idealized high angle asperities undergoing shear. As shown in Figure 1-2, he identified alternating zones of compression and tension along the restraining bend of each asperity. This stress pattern significantly influences the mode of asperity failure, as is discussed later in this section. Hyett and Hudson (1990) cast impressions of natural rough joint surfaces using a

photoelastic material and subjected these reassembled models to various shear and normal loads. Under normal loading, they observed significant stress concentrations at intermittent points of contact between the joint surfaces. With increasing normal load, these concentrations were reduced as the fracture surfaces deformed and the contact area increased. Under shear loading, significant stress concentrations were observed at restraining bends. These observations are detailed in Figure 1-3.

Observations of small fault zones in the French Alps (Gammond, 1987) show similar results. These fault zones show evidence of pressure solution along the faces of restraining bends and vein precipitation along dilated releasing bends. Pressure solution is a form of diffusive mass transfer (Groshong, 1988; White and Knipe, 1978; Kerrich and Allison, 1978) where material in a highly stressed zone (typically 30 MPa to 100 MPa normal stress), is dissolved by a pore fluid and precipitated in regions of available pore space, in this case dilated releasing bends at other locations along the fault.

Scholtz (1990) has reviewed numerous recent earthquakes and observed that both restraining and releasing jogs have served as the epicentres of earthquakes, as the terminations of seismic rupture, and as the loci of aftershock activity. In fact, he concluded that few modern earthquakes have not been influenced in some way by the presence of fault jogs. Segall and Pollard (1980) examined the theoretical stress field around restraining and releasing fault offsets (a form of jog where there is no fracture trace between parallel segments). Their results show increased mean stresses and maximum shear stresses near restraining offsets and reduced mean stresses and maximum

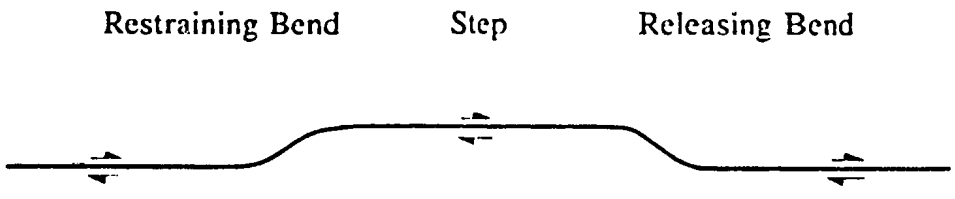

Figure 1-1. Asperity morphology, adapted from Scholtz (1990). Note that while Scholtz used the term "jog" to describe large scale deviation from the mean fracture plane, the term "asperity" is used throughout this study.

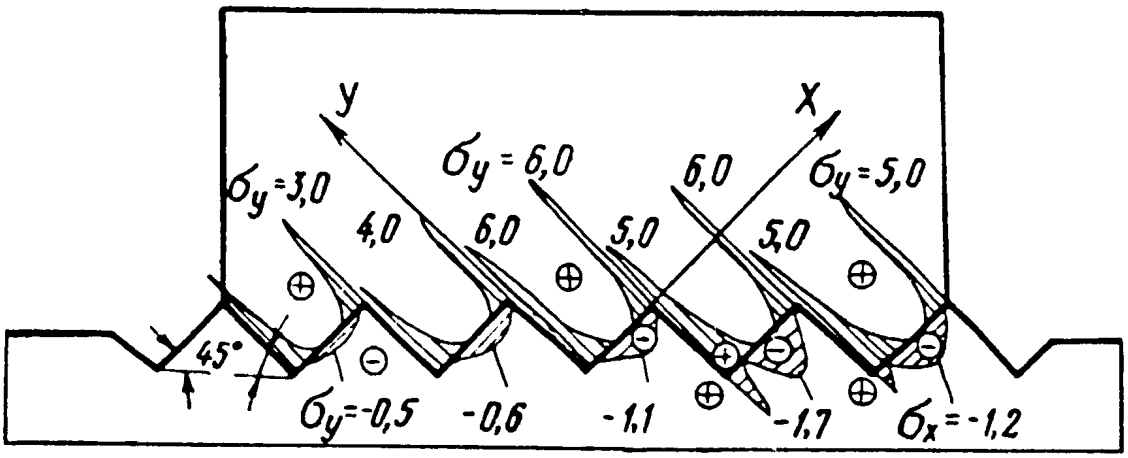

Figure 1-2. Stress field near a rough fracture undergoing right lateral shear. Note the alternating zones of tension and compression associated with the idealized high angle asperities. (Taken from Fishman, 1990).

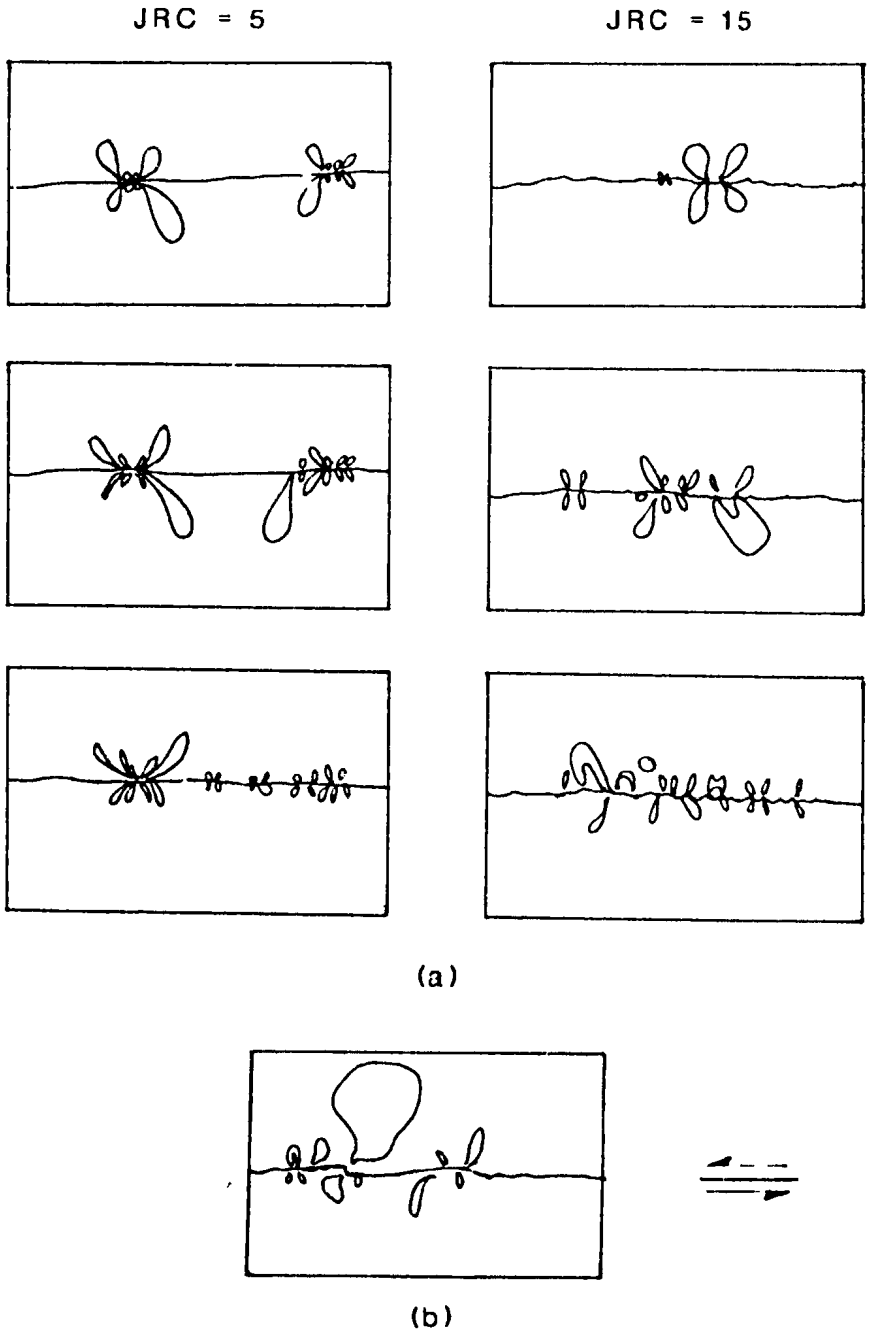

Figure 1-3. Results of a photoelastic study of natural rough joint surfaces where (a) the normal load is increased (going down the page) for fractures with two degrees of roughness and (b) the applied load is inclined at 60° to the mean fracture plane. Note that these diagrams are sketched from photographs presented in Hyett and Hudson (1990) and represent the outer trace of the first photoelastic fringe.

shear stresses near releasing offsets. Predicted secondary fracturing patterns are dominantly conjugate shears for the restraining offset and dominantly tensile fractures for the releasing offset. Sibson (1986) has reviewed previous field and theoretical studies of brecciation processes active during seismic faulting and reached similar conclusions.

Field reconnaissance by Erickson and Wiltschko (1991) to the Lewis Thrust in the front ranges of the Rocky Mountains highlighted alternating sections of the hanging wall that were dominated by contractional and then extensional deformational features. Contractional features included secondary thrusting on the large scale and pressure solution seams on the small scale, while extensional features included secondary normal faults on the large scale and extensional fractures on the small scale. Subsequent analytical modelling indicated that the observed deformational patterns were consistent with variations of shear strength (and hence slip) along the fault. In the region ahead of a stronger portion of the thrust (termed a "patch"), mean stresses are increased relative to background levels and corresponding contractional features are formed and vice versa for the region just behind the patch. Although the existence of this "patch" was only inferred and never identified, it was acting as a restraining bend because it was impeding uniform slip along the fault. The deformational patterns observed give insight into plausible secondary fracturing patterns associated with large scale roughness and suggest that the regions in front of a restraining bend would be dominated by contractional features and regions behind it would be dominated by extensional features.

Several researchers have conducted experiments on rough rock/steel interfaces to examine failure modes of idealized high angle asperities. Handanyan et al. (1990) sheared triangular, spherical and rectangular asperity models (each with bend angles $\geq$ 45°) to failure under nondilatant conditions. They cast their models using a high strength dental material having properties similar to a medium strength igneous rock. They found that combinations of shear fractures oriented parallel to the mean fracture plane and tensile fractures oriented approximately normal to the loaded bend face propagate across the asperity (Figure 1-4). Fishman (1990) carried out dilational shear experiments on models made from gypsum, using the same fracture morphology as in his photoelastic study mentioned earlier. He observed that asperities failed by rotation after a tension crack had propagated across the base of the asperity (Figure 1-5). Fishman also derived equations predicting shear strength and dilatancy as functions of rock crush strength, asperity dimensions and applied shear and normal stresses. It appears that the observed differences in modes of asperity failure between these two studies are related to dilational constraints; rotation of fractured asperities is easier under dilated conditions and increased pore volume. Both of these studies suggest plausible modes of asperity failure during shear. Aydan et al. (1990) conducted finite element modelling of rock asperities similar to those above, and predicted the development of zones of high shear and tensile microcrack density on both sides of the loaded asperity face.

Finally, modes of asperity failure have been studied by Barton et al. (1985) within the context of fracture shear strength, similar to the work of Fishman (1990) above.

They have recognized that large scale fracture roughness increases shear strength through asperity interlock. At low fracture normal stress, asperities are overridden at peak shear strength while they are bypassed by secondary fracturing at higher normal strength. They have incorporated these observations into an empirical shear strength model, known as the Barton-Bandis failure criterion, which is given as:

$$T = \sigma_N \tan (JRC \log(JCS/\sigma_N) + \phi_r) \quad (1\text{-}1)$$

where T is the fracture shear strength (MPa) and σ_N is the applied fracture normal stress (MPa). ϕ_r is the residual or minimum friction angle of the fracture material and represents the basic friction between the smooth fracture surfaces adjusted for saturated conditions. JRC is the Joint Roughness Coefficient and is a dimensionless constant indicating the degree of fracture roughness and ranges from 0 to 20, with 20 being the roughest. JCS is the Joint Wall Compressive Strength and is a measure of the strength of the fracture wall. JCS is equal to the uniaxial compressive strength of the intact rock for an unweathered fracture and decreases with the degree of weathering. Both JRC and JCS are determined from simple tests which can be done on exposed joint surfaces in the field or laboratory. The basis of this failure criterion is the concept of progressive mobilized shear strength, where successive components of fracture strength are utilized and then exceeded as the fracture displaces. The first component of shear strength mobilized is residual friction. When the shear stress on the fracture exceeds the frictional shear strength, the fracture displaces and roughness is mobilized. Peak shear

strength is achieved when roughness asperities are bypassed, as discussed above. Normally, both large and small scale roughness are incorporated into the value of JRC. However, when a single large scale roughness asperity is present on the fracture plane, the angle of this asperity with the mean fracture plane is added to the residual friction value to determine the ultimate fracture shear strength.

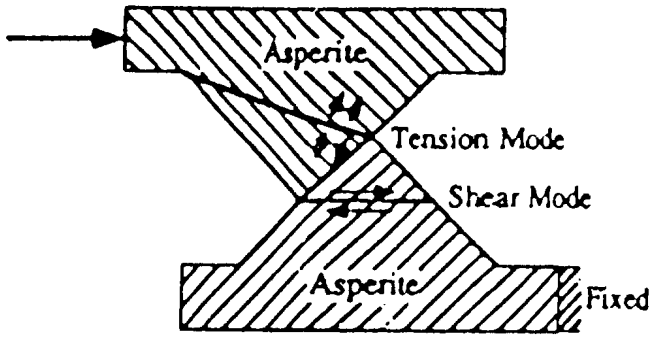

Figure 1-4. Experimentally observed failure modes of high angled asperity during non dilatant shear. (Taken from Handanyan et al., 1990).

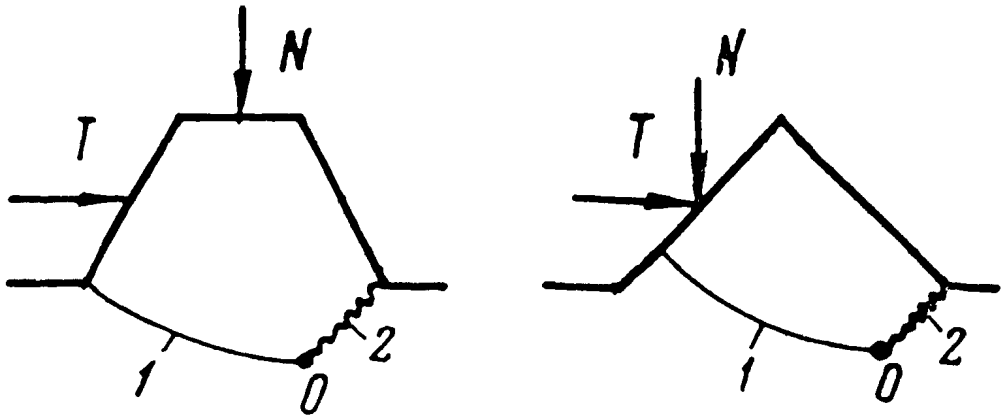

Figure 1-5. Experimentally observed failure mode of high angled asperity during dilatant shear. Note that 1 is a tensile secondary fracture, 2 is a zone of crushing and 0 is the point of asperity rotation. (Taken from Fishman, 1990).

Chapter 2 - Numerical Modelling

Finite element modelling in this study had two objectives. First of all, initial numerical modelling was conducted to evaluate several proposed large scale roughness morphologies for the physical biaxial experiment. This modelling was completed for a range of normal and shear fracture stresses and friction angles using material properties estimated from standard tables and previous experimental work. Once the fracture morphology was selected, preliminary experiments were done on test samples to determine the exact material properties. Finally, these material properties were used in detailed predictive modelling of the proposed physical experiment to enable direct comparison between numerical and subsequent experimental results.

2.1 Finite Element Code

The finite element code used in this investigation is described by Gale (1975) and was modified for this study to run under SUN Fortran. The modelling code uses a plane strain formulation to model intact rock and the joint element of Goodman, Taylor and Brekke (1968) to model fractures. Model solutions are provided by an iterative process with convergence to user specified tolerances. Residual stresses for the plane strain elements can be included as model input in the form of a restart file. This feature can be used to approximate an initial stress state or to modify material properties during loading to simulate nonlinear material behaviour.

2.2 Finite Element Mesh Geometry

Preliminary finite element models were developed to evaluate several proposed large scale roughness morphologies for this investigation. These proposed morphologies were based on typical asperity dimensions and bend angles observed in natural fracture profiles and included single, symmetrical asperities with bend angles of 9°and 18° and widths ranging from 5 to 8 cm. Only single asperities were considered because of the concern of interaction between multiple asperities and the increased complexity in interpreting subsequent results.

Finite element mesh dimensions and geometry were based on a vertical cross section through the biaxial shear frame sample box and fractured sample as shown in Figure 2-1. The plane strain formulation of the modelling code was considered suitable for this mesh geometry because most of the concrete model is constrained from deforming in the out of plane direction by the steel sample box. Only the portion of the model immediately adjacent to the fracture is not constrained. The mesh was rotated 45° from the orientation shown, as indicated by the global axes. This simplified application of the boundary conditions by forcing all nodal restraints and loads to be parallel to the global axes. Roller boundary constraints were applied where the sample box is restrained by reaction members in the biaxial frame. The elastic constants of the steel, concrete and epoxy were estimated from standard tables (Beer and Johnston, 1981; Goodman, 1989, 1976) and were E_{steel} = 200 GPa, $E_{concrete}$ = 33 GPa, E_{epoxy} = 40 GPa, ν_{steel} = 0.27 and $\nu_{concrete} = \nu_{epoxy}$ = 0.25, while the fracture stiffnesses were approximated from previous experimental work (Atkinson, 1987) and were $K_{normal} = K_{tangential}$ = 25 GPa/m.

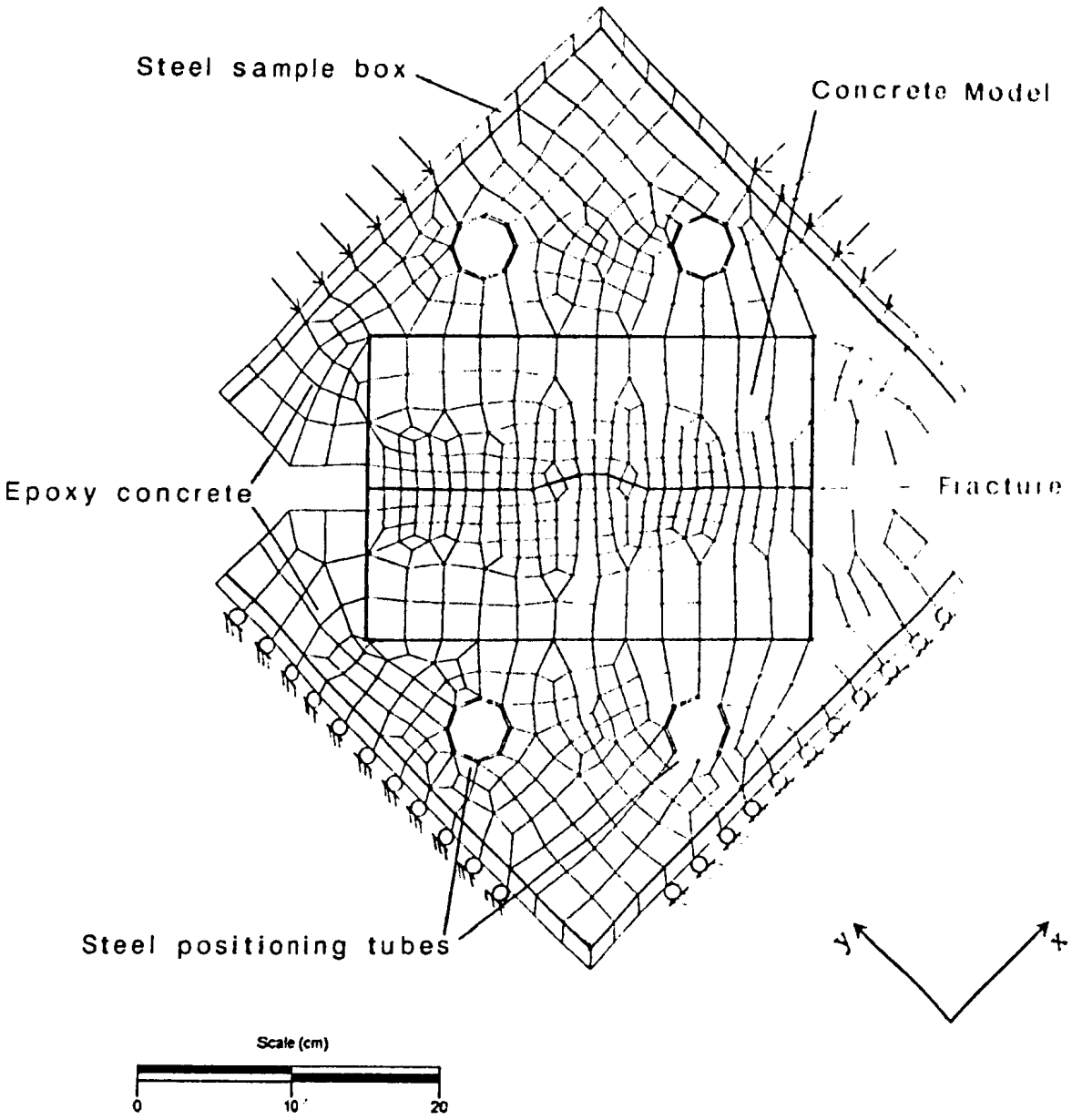

Figure 2-1. Finite element mesh geometry and boundary conditions for large scale roughness model. Note orientation of global coordinate axis with respect to the mesh.

Each of the preliminary finite element models was evaluated using two different loading procedures. In the first procedure, shear stresses on the mean fracture plane were increased over the range τ = 3 to 5 MPa while the normal stress on the mean fracture plane remained constant at σ_N = 5 MPa and the friction angle of the fracture was held constant at 40°. In the second procedure, normal and shear stresses on the mean fracture plane were held constant, at values of σ_N = 3 MPa and τ = 5 MPa, and the friction angle of the fracture was incrementally reduced from 40° to 20°. Based on these model studies, the large scale roughness morphology shown in Figure 2-2 was selected for the biaxial experiment. Numerical results indicated that this asperity morphology could generate significant secondary fracturing (given the capacity of the biaxial loading frame) and produce strain patterns suitable for measurement using electrical resistance strain gauges.

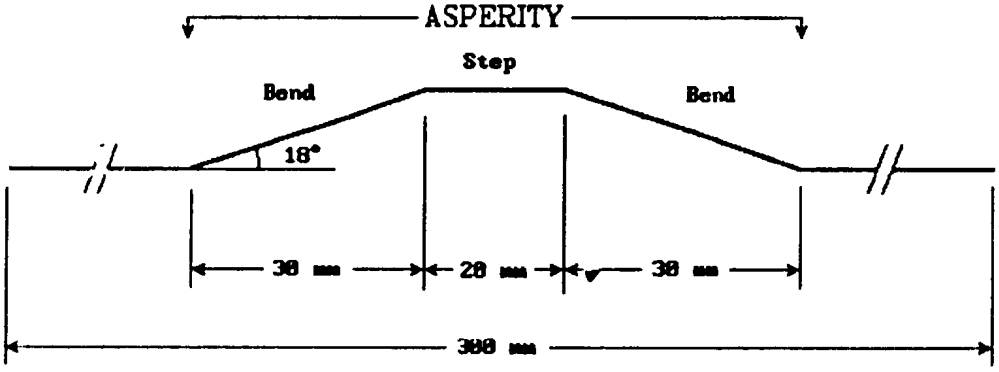

Figure 2-2. Final large scale roughness morphology used for both predictive numerical modelling and the physical model.

2.3 High Strength Concrete and Simulated Fracture

The physical biaxial experiment required a material that had strength, elasticity and texture similar to natural rock. This was done to ensure that the behaviour observed in the laboratory would be similar to that which would be expected from natural fractures at comparable scales. High strength concrete was a suitable candidate because of it's high uniaxial compressive strength (50 to 100 MPa), correspondingly low tensile strength (5 to 10 MPa) and brittle behaviour. However, since internal model deformation was to be measured using electrical resistance strain gauges, the maximum size of the concrete aggregate was limited. Berwanger's (1968) study of the suitability of electrical resistance strain gauges to measure concrete deformation found that the active gauge length of the strain gauges should be at least 2.7 times the maximum aggregate size to homogenize the gauge response over the soft matrix and stiffer aggregate. Cost and the scale of the physical model limited the gauge length of the strain gauges to 240 mils and hence a maximum aggregate size of 2.2 mm.

The resulting high strength concrete mixture (developed by the Engineering Geology Group for this study and similar investigations) used two grades of commercial silica sand as aggregate and silica fume as an admixture to increase strength. Silica sand grades #00 and #2 were used as aggregate, providing a maximum aggregate size of 1.8 mm. A superplasticizer was added to the mix water to increase the slump of the wet concrete and extend its working time. This mixture required considerable internal vibration during pouring to remove entrained air and improve compaction. The final cured concrete had the grain size and texture of a fine grained intrusive igneous rock.

This concrete material was used in all concrete samples and models tested during this investigation.

Natural rough fractures were simulated by placing a woven geotextile between successive lifts of concrete. When cured, the concrete lifts were separated, the geotextile was removed and the concrete blocks carefully reassembled. The simulated fracture texture was similar to a natural fracture in that opposing fracture surfaces were largely in contact at asperity tips with abundant pore space in between. This type of texture has been shown experimentally to closely approximate the mechanical behaviour of natural fractures (Atkinson, 1987).

2.4 Experimental Determination of Material Properties

Several intact and fractured test samples were cast using the concrete mixture and procedures described in the previous section. Laboratory tests were conducted on these samples using the appropriate ASTM and ISRM standards and procedures. The results of these tests enabled accurate determination of (1) the elastic constants of the intact concrete and the normal and shear stiffnesses of the simulated fracture over the range of applied loads available in the biaxial loading apparatus, (2) the age dependent strength of the concrete and (3) correlation between acoustic emissions and inferred brittle deformation.

2.4.1 Concrete Elastic Constants and Fracture Stiffnesses

Two 152 mm diameter concrete cylinders were cast with an approximate length

to diameter ratio of 2. One sample was intact while the other had a simulated fracture perpendicular to the core axis. These samples were instrumented as shown in Figure 2-3 and nondestructively tested in uniaxial compression under load control. The intact cylinder was loaded to 40 MPa, where the load was held and then removed. Strain gauges attached to the sample recorded the average axial and diametrical strain (Figure 2-4). Straight lines fitted to linear portions of these stress-strain curves were used to determine values of Young's Modulus and Poisson's Ratio for the intact concrete over the normal stress range of 0 to 8 MPa, as given in Table 2-1. Note the hysteresis during unloading, indicating that some permanent deformation has occurred. Since the accelerometer did not record any significant acoustic emissions during this loading, we can conclude that this deformation is not the result of brittle fracturing but some other inelastic deformation, possibly creep.

The fractured cylinder was tested under two complete loading cycles of 15 MPa and one half cycle to 12.5 MPa. The closure of the fracture under these loading cycles was measured as the difference between the averaged displacement of two of the circumferential LVDTs (the third LVDT showed anomalous displacement, likely due to slight eccentric loading of the sample, and was ignored in the analysis) and the intact LVDT (Figure 2-3). Normal stress versus fracture closure curves for these tests are given in Figure 2-5. Normal stiffnesses were calculated for approximately linear portions along these curves, again over the normal stress range of 0 to 8 MPa, as given in Table 2-2. Note that the closure curves for the second and third loading cycles are nearly parallel with the unloading curve of the first loading cycle, indicating that the fracture

was well seated during the initial loading cycle. The only acoustic emissions recorded during this test were associated with this initial fracture seating.

A 200 mm by 200 mm by 300 mm rectangular concrete block was cast and allowed to cure for 90 days. The concrete block had a simulated fracture running fully along it's length and midway up it's height, dividing the block into two equal sections. The simulated fracture had no large scale roughness, only the small scale roughness produced by the texture of the geotextile. Schmidt hammer rebound and tilt tests were conducted on the sample following the procedures outlined in Barton et al. (1985). Analysis of the results showed a residual friction angle of 29°, a JCS value of 52.4 MPa and a JRC value of 3.0. These values were incorporated into a modified Barton-Bandis fracture deformation model (Gale et al., 1993) to simulate shear cycles at 2 and 8 MPa of normal stress after three initial normal loading cycles. From the resulting shear stress versus shear displacement curves, values of shear stiffness over approximately linear regions of the displacement curves were calculated, as given in Table 2-3.

During normal loading, shear stresses of approximately 30% of the normal stress are resolved onto the faces of the 18° asperity bends. To account for this, it was necessary to estimate values of shear stiffness for the fracture over a range of normal loads. Using shear stiffness values from Table 2-3, a linear relationship was derived to estimate the shear stiffness as a function of the applied normal stress. This relationship was used to calculate the shear stiffness values given in Table 2-4.

Table 2-1. Values of Young's Modulus and Poisson's Ratio determined from the first loading cycle of the 152 mm diameter intact concrete cylinder.

Stress interval (MPa)	Young's Modulus (GPa)	Poisson's Ratio
0.0 to 2.0	60.0	0.408
2.0 to 8.0	48.6	0.330

Table 2-2. Normal stiffness values determined over linear intervals of normal stress versus normal closure curves.

Loading cycle	Stress interval (MPa)	Normal Stiffness (GPa/m)
	0.0 to 0.5	9
F	0.5 to 1.0	25
I	1.0 to 2.0	83
R	2.0 to 5.0	273
S	5.0 to 8.0	1500
T	8.0 to 5.0	3400
	5.0 to 2.0	3400
S	0.0 to 0.5	22
E	0.5 to 1.0	250
C	1.0 to 2.0	3400
O	2.0 to 5.0	3400
N	5.0 to 8.0	3400
D	8.0 to 5.0	3400
	5.0 to 2.0	3400

Table 2-3. Shear stiffness values determined over linear intervals of shear stress versus shear displacement curves at normal stresses of 2 and 8 MPa.

Normal stress	Stress interval (MPa)	Shear Stiffness (GPa/m)
2	0.00 to 0.54	102
	0.54 to 0.84	39
M	0.84 to 1.03	14
P	1.03 to 1.23	3
a	1.23 to 1.50	3
8	0.00 to 2.09	406
	2.09 to 2.94	166
M	2.94 to 3.70	74
P	3.70 to 4.20	28
a	4.20 to 4.60	8

Table 2-4. Approximate shear stiffnesses determined over normal stress intervals. Note that this was done to accommodate shear stresses resolved onto the asperity bends during normal loading.

Normal Stress interval (MPa)	Shear Stiffness (GPa/m)
0.0 to 0.5	25
0.5 to 1.0	51
1.0 to 2.0	102
2.0 to 5.0	254
5.0 to 8.0	406
8.0 to 5.0	254
5.0 to 2.0	102

2.4.2 Concrete Strength

Two intact concrete cylinders were tested to failure to determine the age dependent uniaxial compressive strength of the concrete. Each cylinder was poured from a different concrete batch, but the same concrete mix, materials and procedures were used to cast each cylinder. One cylinder was 76 mm in diameter while the other was 152 mm in diameter. Note that the 152 mm diameter cylinder was the intact 152 mm diameter cylinder nondestructively tested earlier (Section 2.4.1) to 40 MPa. Both cylinders had an approximate length to diameter ratio of 2 and were tested under displacement control with approximately the same loading rate of 1 MPa per minute. The 76 mm diameter cylinder was tested after curing 40 days and yielded a uniaxial compressive strength, normalized to an exact length to diameter ratio of 2 (ASTM Standard D 2938-86), of 52.7 MPa. The 152 mm diameter sample was tested after curing 116 days, yielding a normalized strength of 68.7 MPa. While normal concrete reaches over 95% of it's maximum strength after curing 28 days, the curing of high strength concrete is slower, usually requiring 90 days to reach this same percentage strength (CPCA handbook, 1991). Thus, given the cured ages of each of the failed test specimens, we can conclude that the maximum uniaxial compressive strength of this concrete is approximately 70 MPa.

Most high strength concretes have tensile strengths approximately 5% to 10% of their uniaxial compressive strength (CPCA handbook, 1991). Since the concrete mixture used here has much smaller than normal aggregate size (with a much higher aggregate surface area to volume ratio), and internal vibration was used to expel most entrained air,

we can assume that the concrete used in this study will have a tensile strength at the upper end of this range. Thus the tensile strength is estimated to be approximately 7 MPa.

2.4.3 Acoustic Emission Signature of Brittle Deformation

An accelerometer attached to the intact 152 mm cylinder recorded acoustic emissions as the sample was loaded to failure (Section 2.4.2). Figure 2-6 plots both the applied uniaxial stress and acoustic emission count over 30 second intervals versus the axial strain recorded using an LVDT mounted between the platens of the loading frame. (Note that the square root of the acoustic emission count is given, as opposed to the actual value. This was done to attenuate the high AE rate recorded at the peak and to highlight the AE rates recorded before and after the peak, which would be difficult to view on a graph of straight AE values.) There is good correlation between the intensity (or rate) of acoustic emissions and inferred macroscopic deformation within the sample; acoustic emissions are very sparse in the linear elastic portion of the loading curve, but begin to rise in intensity as the sample enters the nonlinear plastic region of the curve where brittle microcracks begin to form (Jaeger and Cook, 1976). Emissions are highest, understandably, at sample failure which was observed by the formation of conjugate shear fractures across the length of the sample.

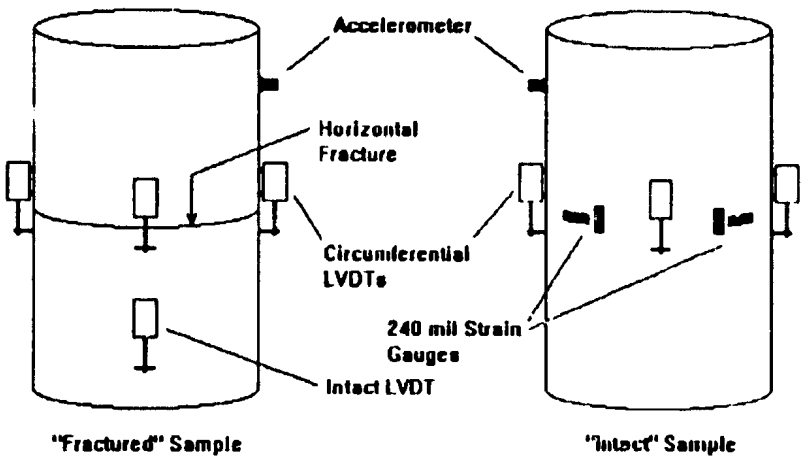

Figure 2-3. Position of instrumentation on intact and fractured 152 mm diameter samples.

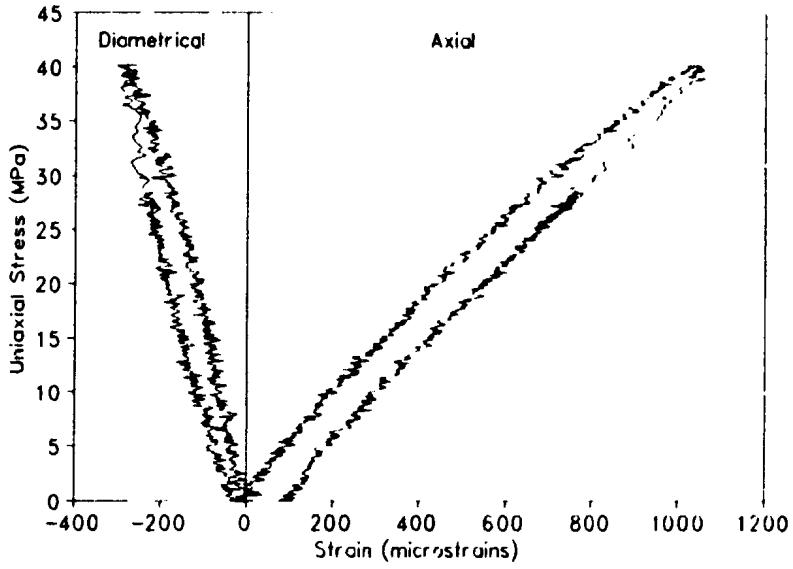

Figure 2-4. Axial and diametrical strain recorded during nondestructive uniaxial compression loading of intact 152 mm diameter sample.

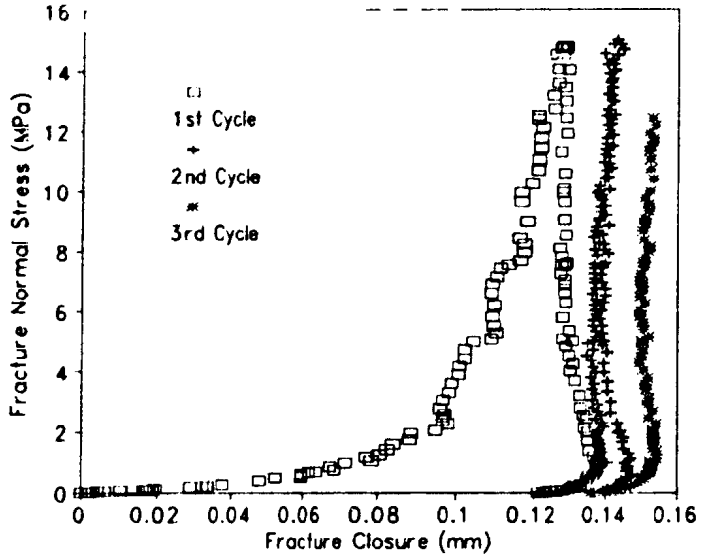

Figure 2-5. Normal stress versus normal closure curves from nondestructive uniaxial testing of fractured 152 mm diameter sample.

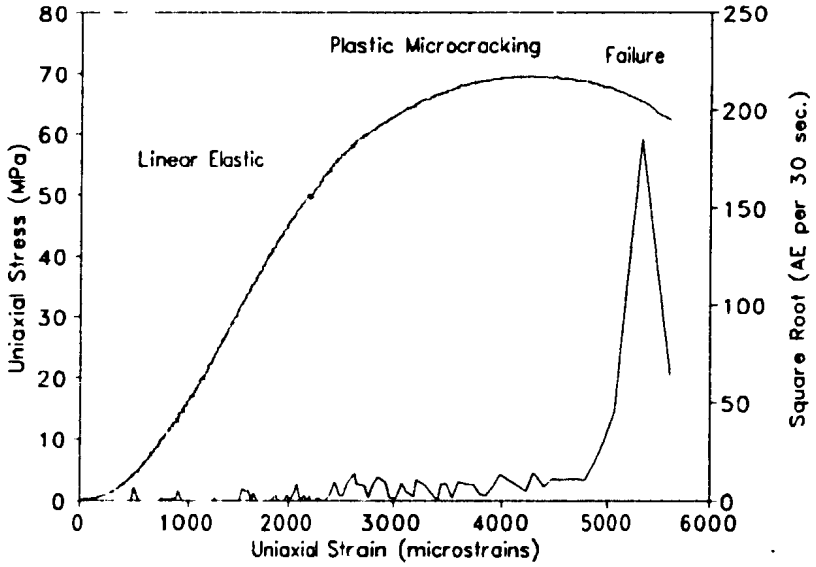

Figure 2-6. Plots of uniaxial stress and acoustic emission counts versus uniaxial strain recorded during destructive testing of intact 152 mm diameter sample.

2-5. Predictive Numerical Modelling

Numerical simulations of proposed loading cycles were achieved using a nonlinear modelling approach, where the model was loaded in small increments. Stress dependent material properties, determined in the preceding section, were modified at the start of each load increment and the stress state at the end of the previous increment was incorporated as a residual stress block (Section 2.1). This forced material properties in the numerical model to conform to experimentally determined values throughout the loading path. For example, to increment the numerical model from an applied fracture normal stress of 5 to 8 MPa, the mesh boundary loads would be assigned to resolve a normal stress of 8 MPa onto the mean fracture plane and the elastic constants of the concrete and the fracture stiffnesses would be assigned the appropriate values for the normal stress range of 5 to 8 MPa. The stresses determined for the plane strain elements at the end of the 5 MPa loading step would be included as a residual stress block. When run, the model would simulate a stress increment from 5 to 8 MPa, using the material and fracture properties independently determined for that normal stress range. Throughout this nonlinear modelling, the friction angle of the fracture remained constant at 40°. Finally, no residual stresses were passed between successive loading cycles, so each loading cycle began in an initially unstressed condition.

Stresses within the concrete model were presented as plots of major and minor principal stress trajectories, as contoured values of mean stress and maximum shear stress, and as horizontally and vertically oriented stresses. The mean stress, σ_{mean}, was calculated as $\frac{1}{2}(\sigma_{max}+\sigma_{min})$, where σ_{max} and σ_{min} are the maximum and minimum principal

normal stresses respectively, while maximum shear stress, τ_{max}, was calculated as $\frac{1}{2}(\sigma_{max}-\sigma_{min})$. The horizontally and vertically oriented stresses are provided for direct comparison to the strains measured in the subsequent physical model.

Two normal loading cycles to 8 MPa normal stress were simulated. Only two cycles were modelled since there would be no change in material properties beyond the second cycle and all subsequent results would be identical. Table 2-5 summarizes the stress increments and material properties used during the first and second simulated normal loading cycles. Contoured values for σ_{mean} and τ_{max} from the results of both cycles are given in Figures 2-7 and 2-8. Relatively increased mean stresses and increased maximum shear stresses are observed in the area of the asperity, particularly above the step and below the junctions of the bends with the planar fracture. These portions of the asperity are acting as stress concentrators. (Stress concentrations are also observed at the ends of the fracture, but these are associated with the contact between the concrete model, the epoxy concrete and a free surface, as shown in Figure 2-1, and will be ignored.) However, the magnitude and extent of these concentrations are greater for the first loading cycle where the normal stiffnesses are much lower. This indicates that as the fracture stiffens from repeated closure cycles, the more it behaves like the surrounding intact material and the less the asperity acts as a stress concentrator. The differences in stress state on the upward and falling sides of the loading curve result from the nonlinear behaviour imposed on the fracture by the procedures used in modelling; this reflects the natural closure hysteresis observed in the laboratory (Figure 2-5).

Analysis of the complete normal loading data sets indicates that the maximum

normal stresses generated near the asperity do not exceed 13 MPa and that no tensile stresses are generated. Given this, no secondary fracturing is expected to occur during any normal loading cycles in the biaxial experiment. Figures A-1 and A-2 in Appendix A present contoured values of horizontal and vertical stress for comparison with the physical experiment measurements.

Table 2-5. Stress increments and material properties used during numerical simulation of first and second normal loading cycles.

		Concrete		Fracture	
Normal Cycle	Normal Stress (MPa)	Young's Modulus (GPa)	Poisson's Ratio	Normal Stiffness (GPa/m)	Shear Stiffness (GPa/m)
	0.5	60.0	0.408	9	25
F	1.0	60.0	0.408	25	51
I	2.0	60.0	0.408	83	102
R	5.0	48.6	0.330	273	254
S	8.0	48.6	0.330	1500	406
T	5.0	48.6	0.330	3400	254
	2.0	48.6	0.330	3400	102
S	0.5	60.0	0.408	22	25
E	1.0	60.0	0.408	250	51
C	2.0	60.0	0.408	3400	102
O	5.0	48.6	0.330	3400	254
N	8.0	48.6	0.330	3400	406
D	5.0	48.6	0.330	3400	254
	2.0	48.6	0.330	3400	102

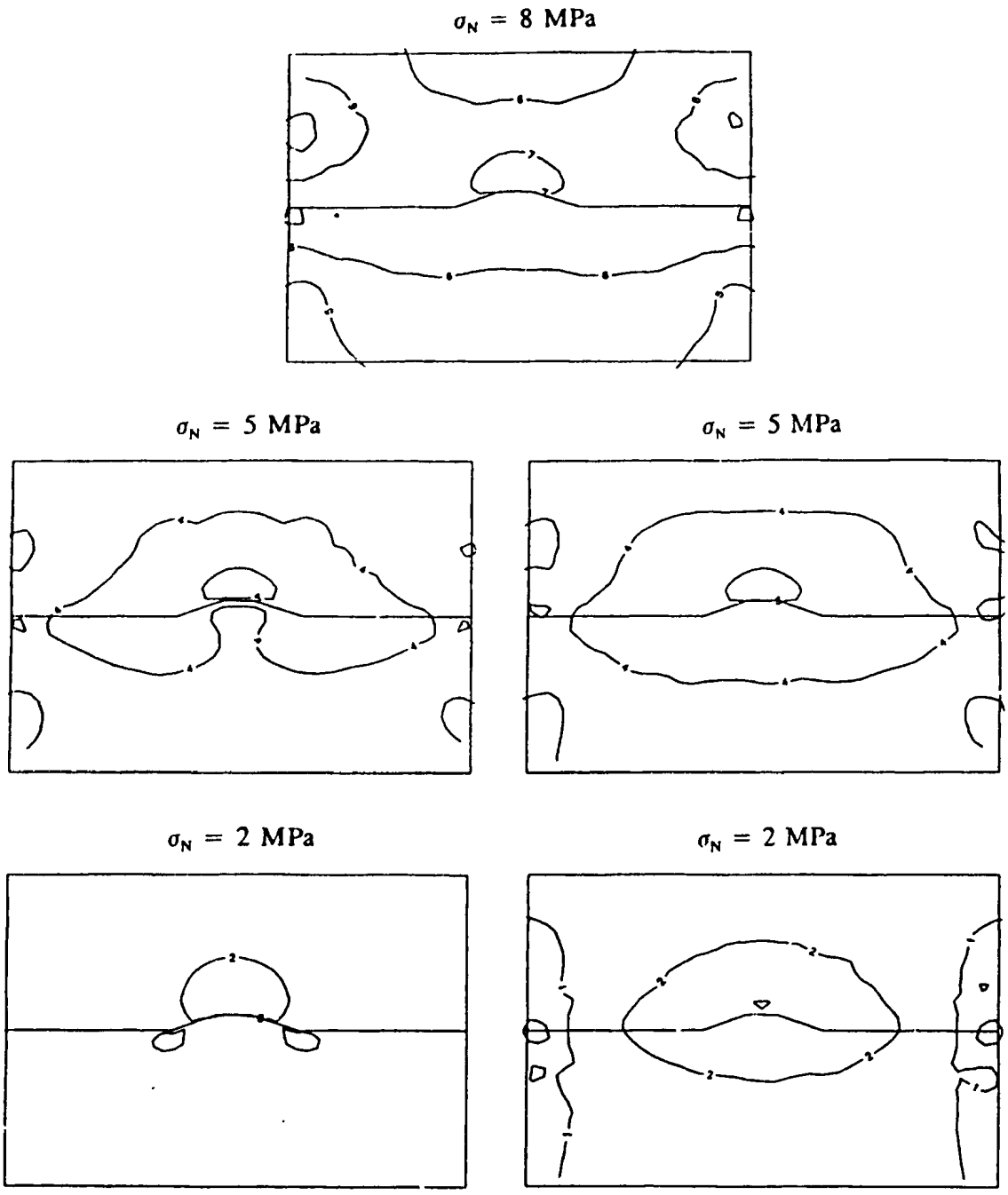

Figure 2-7(a). Mean stress contours for the first modelled normal loading cycle. Compressive stresses are positive and the contour interval is 1 MPa. The stress path is clockwise and the size of the stress field is 300 mm by 200 mm.

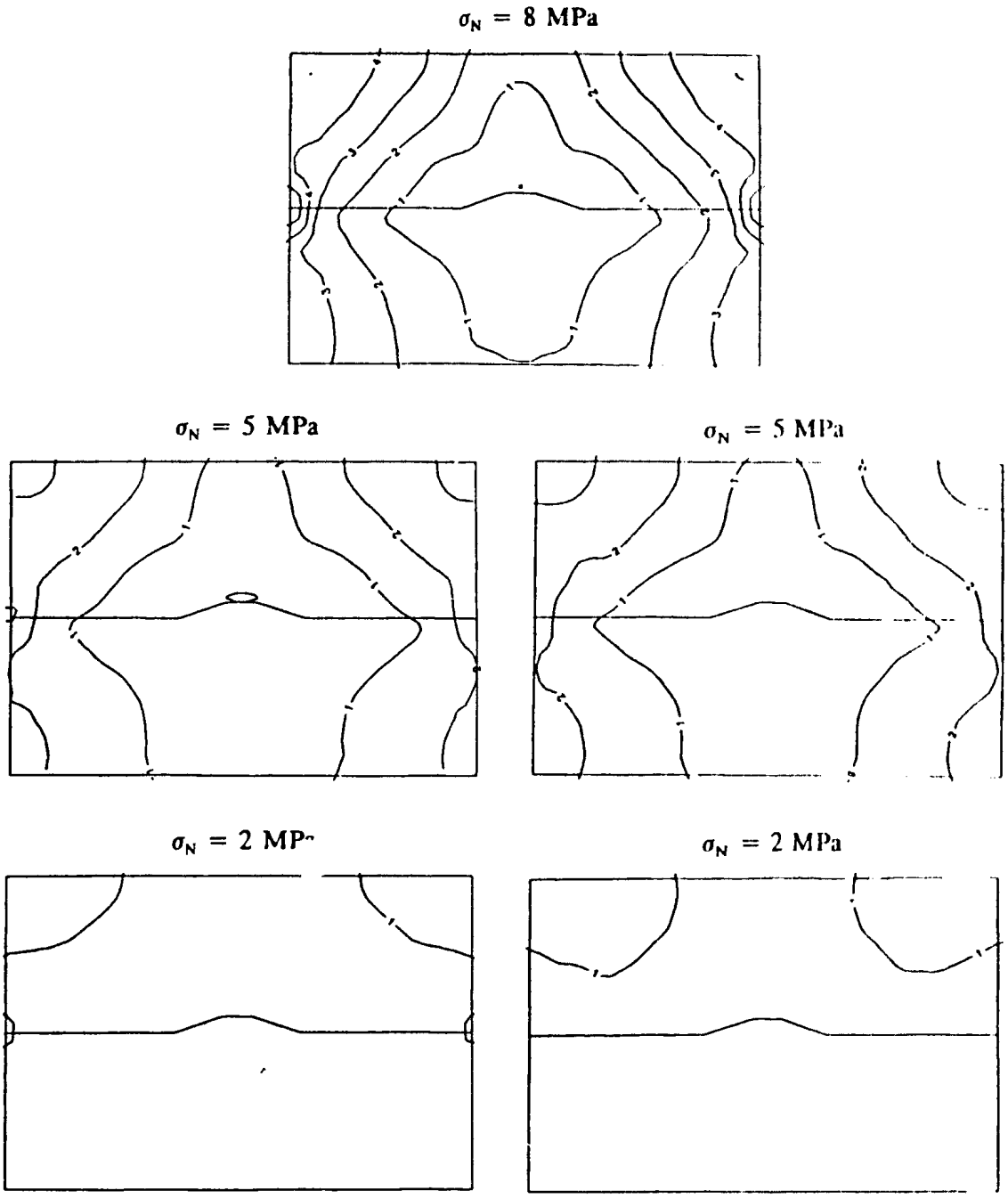

Figure 2-7(b). Maximum shear stress contours for the first modelled normal loading cycle. The stress path is clockwise, the size of the stress field is 300 mm by 200 mm and the contour interval is 1 MPa.

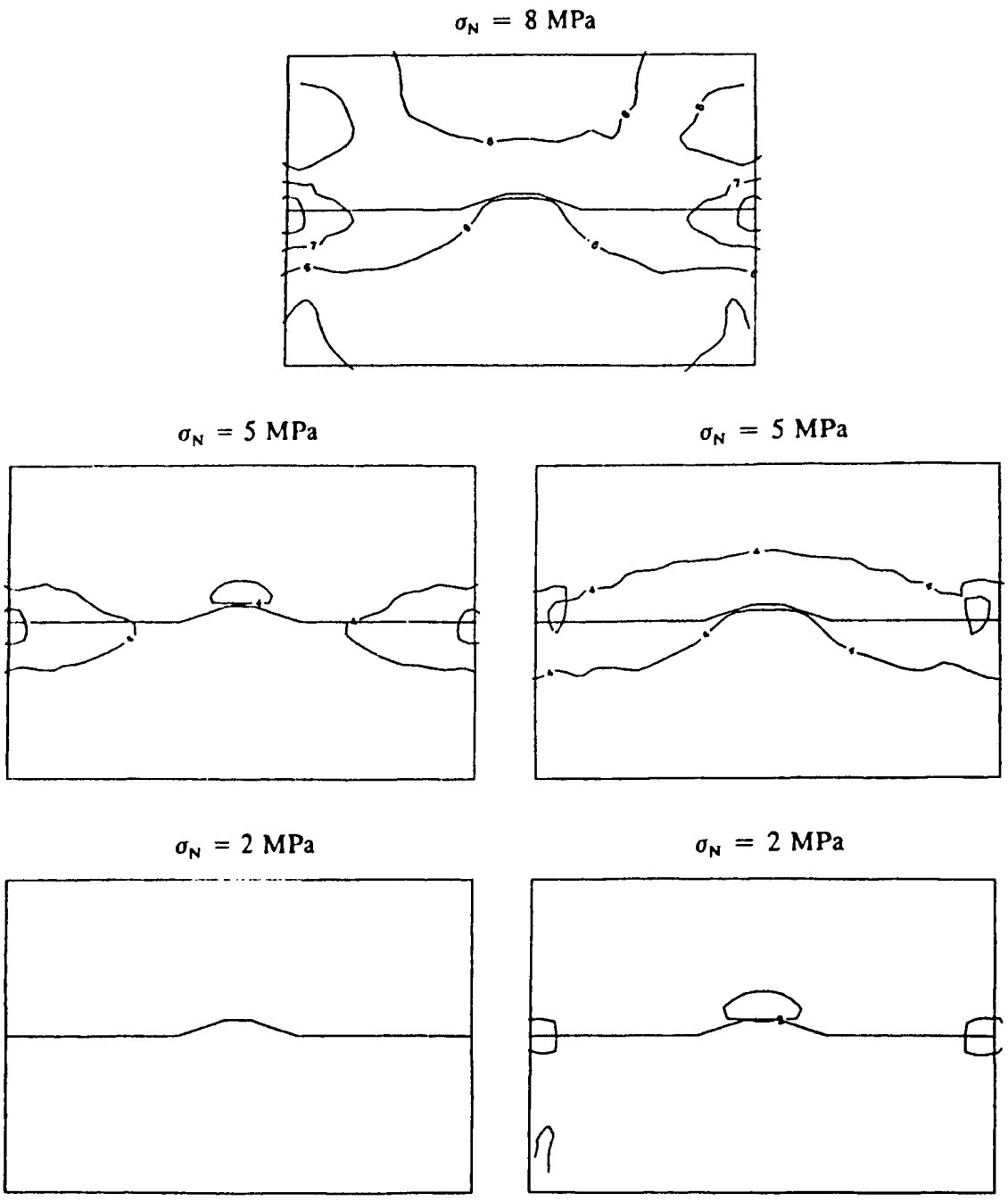

Figure 2-8(a). Mean stress contours for the second modelled normal loading cycle. Compressive stresses are positive and the contour interval is 1 MPa. The stress path is clockwise and the size of the stress field is 300 mm by 200 mm.

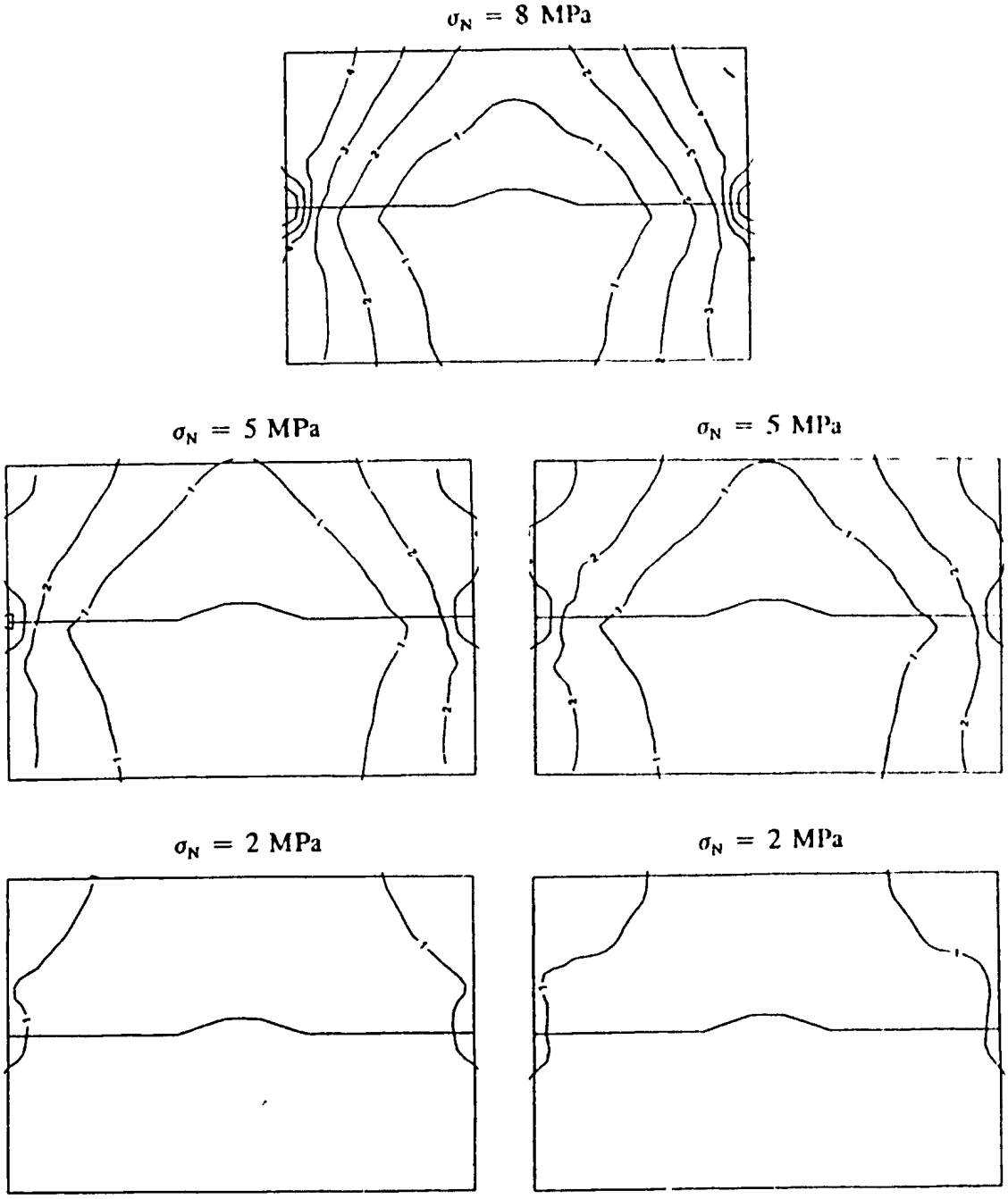

Figure 2-8(b). Maximum shear stress contours for the second modelled normal loading cycle. The stress path is clockwise, the size of the stress field is 300 mm by 200 mm and the contour interval is 1 MPa.

Table 2-6 summarizes the stress steps and material properties used during the first and second simulated shear loading cycles. The residual stress conditions used at the start of each shear cycle were the stress state of the second normal loading cycle at the appropriate normal load. Figures 2-9 and 2-10 present contours of mean stress and maximum shear stress for these cycles. These results show two important trends: (1) the progressive development of increased normal compressive and shear stresses at the asperity restraining bend and (2) the development of zones of tension above the junction of the step and the releasing bend and below the junction of the restraining bend and the

Table 2-6. Stress increments and material properties used during numerical simulation of first and second shear loading cycles.

		Concrete		Fracture	
Normal Stress	Shear Stress (MPa)	Young's Modulus (GPa)	Poisson's Ratio	Normal Stiffness (GPa/m)	Shear Stiffness (GPa/m)
2	0.54	48.6	0.330	3400	102
	0.84	48.6	0.330	3400	39
M	1.03	48.6	0.330	3400	14
P	1.23	48.6	0.330	3400	3
a	1.50	48.6	0.330	3400	3
8	2.09	48.6	0.330	3400	406
	2.94	48.6	0.330	3400	166
M	3.70	48.6	0.330	3400	74
P	4.20	48.6	0.330	3400	28
a	4.60	48.6	0.330	3400	8

planar fracture. These zones of tension are difficult to distinguish in Figures 2-9 and 2-10, but they are highlighted on the contours of tensile stress in Figure 2-11 and on the plots of principal stress trajectories in Figure 2-12. These trends indicate that the

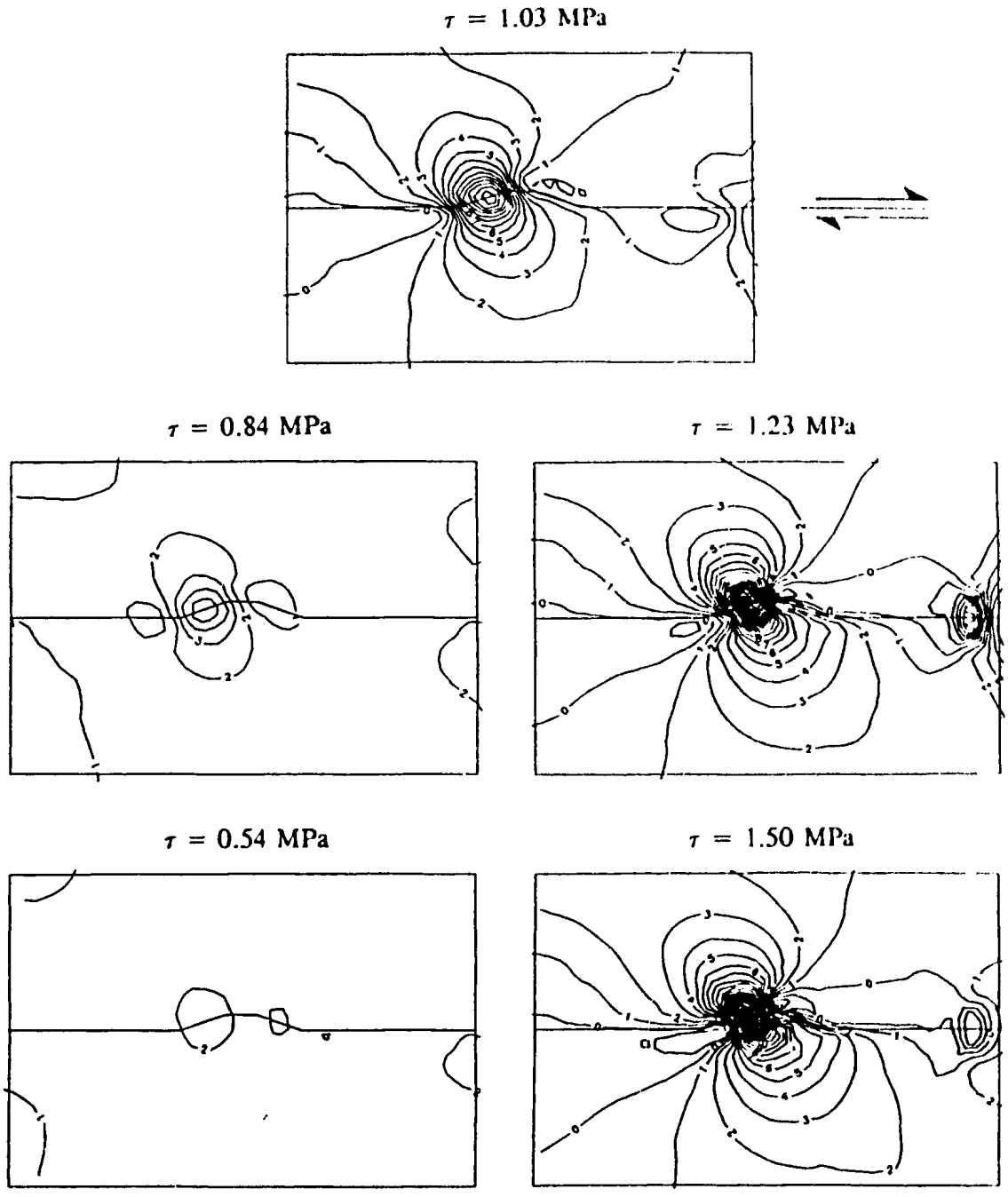

Figure 2-9(a). Mean stress contours for the modelled shear loading cycle at 2 MPa normal stress. Compressive stresses are positive, the size of the stress field is 300 mm by 200 mm and the contour interval is 1 MPa.

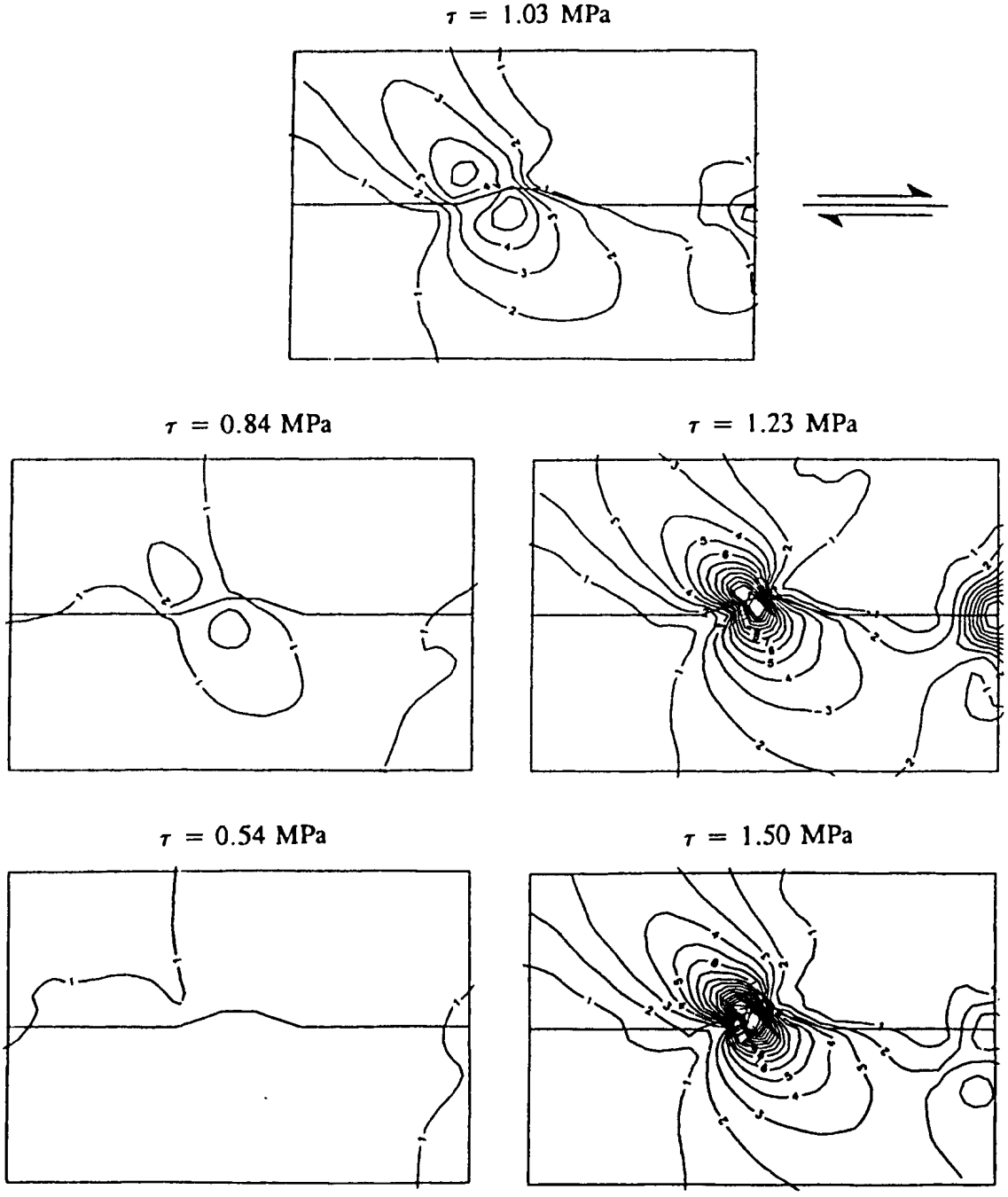

Figure 2-9(b). Maximum shear stress contours for the modelled shear loading cycle at 2 MPa normal stress. The size of the stress field is 300 mm by 200 mm and the contour interval is 1 MPa.

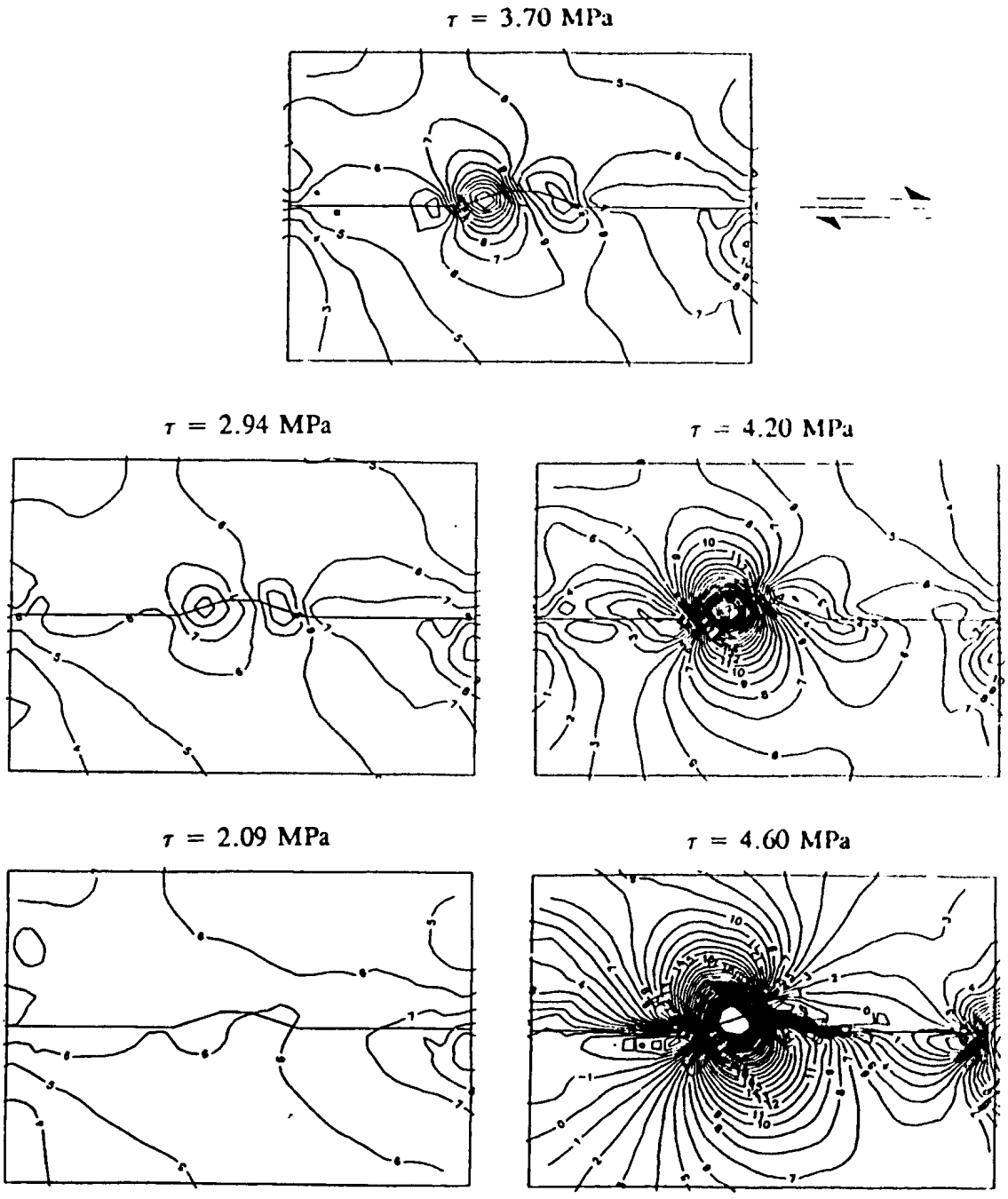

Figure 2-10(a). Mean stress contours for the modelled shear loading cycle at 8 MPa normal stress. Compressive stresses are positive, the size of the stress field is 300 mm by 200 mm and the contour interval is 1 MPa.

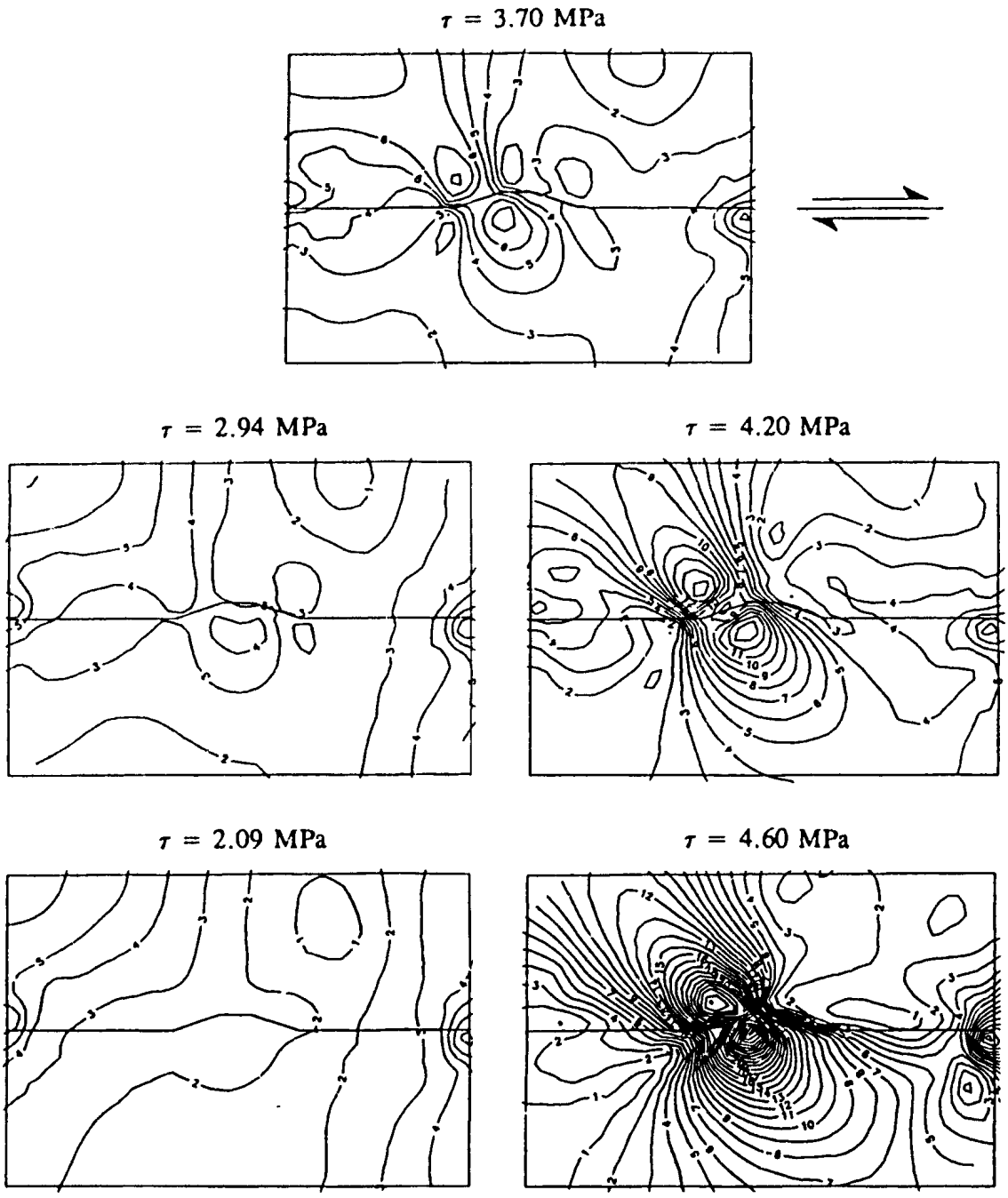

Figure 2-10(b). Maximum shear stress contours for the modelled shear loading cycle at 8 MPa normal stress. The size of the stress field is 300 mm by 200 mm and the contour interval is 1 MPa.

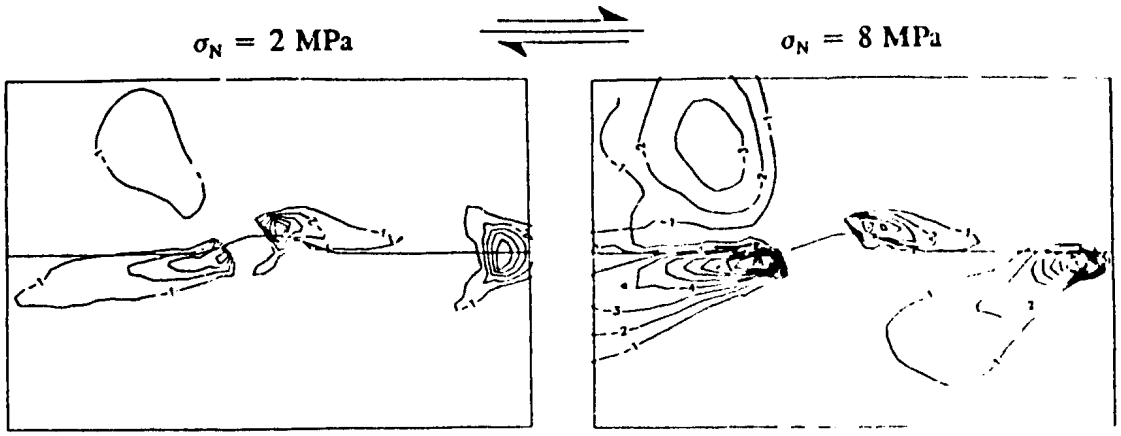

Figure 2-11. Tensile stress contours for the modelled shear loading cycles at peak shear. The size of the stress field is 300 mm by 200 mm and the contour interval is 1 MPa.

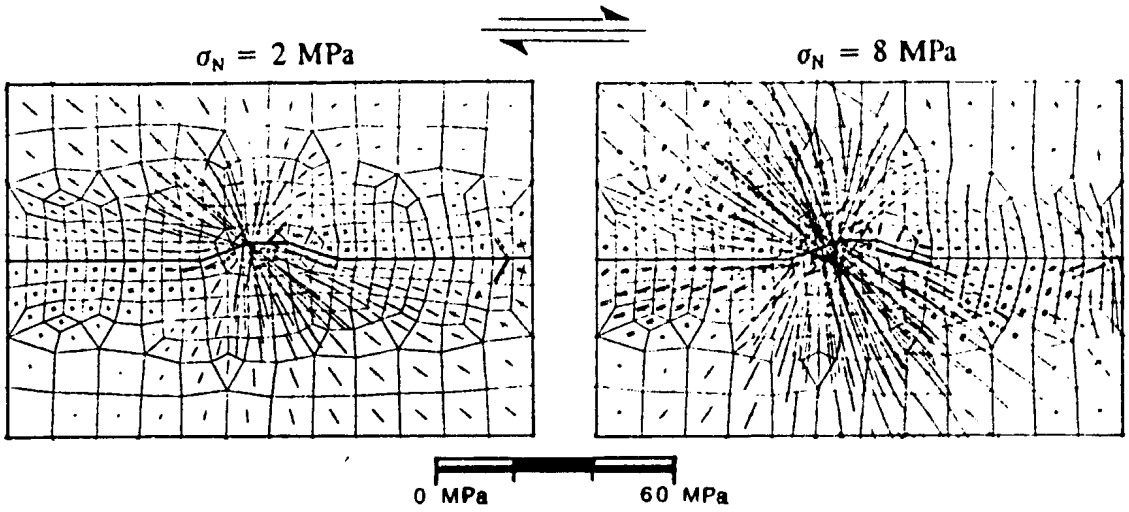

Figure 2-12. Plots of major and minor principal stress vectors at peak shear. The size of the stress field is 300 mm by 200 mm. Double hachure marks indicate tensile stress.

restraining bend is impeding slip along the fracture and is acting as a significant stress concentrator for both normal and shear stresses. Tensile stresses are generated along the fracture where regions of high shear stiffness are preceded or followed by regions of lower shear stiffness.

Analysis of stress magnitudes indicate that, at peak shear for the shear cycle at 2 MPa fracture normal stress, the maximum predicted compressive stresses were approximately 60 MPa and the largest tensile stresses were approximately 4 MPa. Under these conditions, both compressive shear and tensile microcracks would be expected to form in the physical model (refer to Figure 2-6 and the region of plastic microcracking) but because the maximum compressive strength of the concrete (Section 2-4) would not be exceeded, macroscopic sample failure would probably not occur. At peak shear for the 8 MPa normal stress shear cycle, the maximum predicted compressive stress was 92 MPa and the maximum predicted tensile stress generated was 13 MPa. Under these stress conditions, macroscopic shear failure of the physical model would almost certainly occur. Based on the principal stress trajectories shown in Figure 2-12 and the stress patterns observed, the location, mode and orientation of induced secondary fractures were predicted, as shown in Figure 2-13. For these predictions, conjugate shears were placed where the maximum compressive stresses are predicted to occur and are oriented at approximately 30° (i.e. $45°-\phi/2$, where ϕ=internal friction angle and is assumed to be 30°) to the maximum principal stress trajectory and, similarly, tensile fractures were placed in regions where tensile stresses were predicted to occur and are oriented perpendicular to the maximum tensile stress trajectory.

Figures A-3 and A-4 in Appendix A provide contours of horizontal and vertical stresses generated during both shear cycles for comparison to the experimental results.

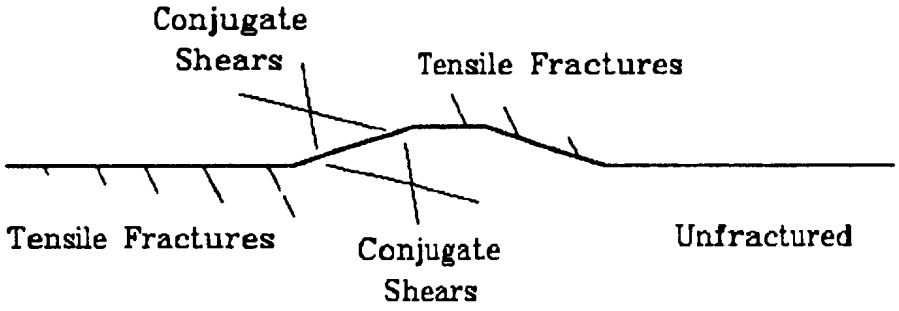

Figure 2-13. Mode, orientation and location of predicted secondary fractures at peak shear.

Chapter 3 - Biaxial Physical Experiment

A 300 mm by 200 mm by 200 mm concrete model, containing a fabricated fracture plane, was constructed. This fracture plane matched the large scale roughness morphology that was numerically modelled in the preceding chapter. Strain gauges were cast into the model, both parallel and perpendicular to the mean fracture, to measure internal strains. LVDTs were mounted on the four corners of the model to measure average normal and shear fracture displacements as the model was subjected to three normal loading and three shear loading cycles. An accelerometer was mounted on the model to monitor acoustic emissions generated by any fracturing induced during testing. At peak shear of the final shear loading cycle, a low viscosity resin was injected into the fracture plane to preserve the state of fracture porosity which was then examined during a "post mortem" sample sectioning.

3.1 Construction of Physical Model

A 152 mm concrete cylinder was cast and four 90 mm by 130 mm by 12 mm thick slabs or "coupons" were cut from it. Thirty nine vertically oriented and twenty nine horizontally oriented single strain gauges (gauge length = 240 mils), and twenty strain gauge rosettes (gauge length = 60 mils) were bonded to these coupons, as shown in Figure 3-1. Vertically oriented refers to a direction perpendicular to the mean fracture plane and horizontally oriented refers to a direction which is parallel to the mean fracture plane. All gauges and lead wires were coated with the manufacturer's recommended

waterproof coatings to protect them during casting of the physical model. Appendix E provides the coordinates of the strain gauge positions in the physical model.

The procedures used in model construction and placement into the sample box and frame are shown schematically in Figure 3-2. Two coupons were glued along the centre line of a wooden form (Figure 3-2a) which was then filled with concrete and internally vibrated. A woven geotextile was placed on the wet concrete and an aluminum plate (Figure 3-2b), having a raised portion with the final asperity dimensions, was pressed firmly into the geotextile forming one side of the simulated rough fracture. After curing

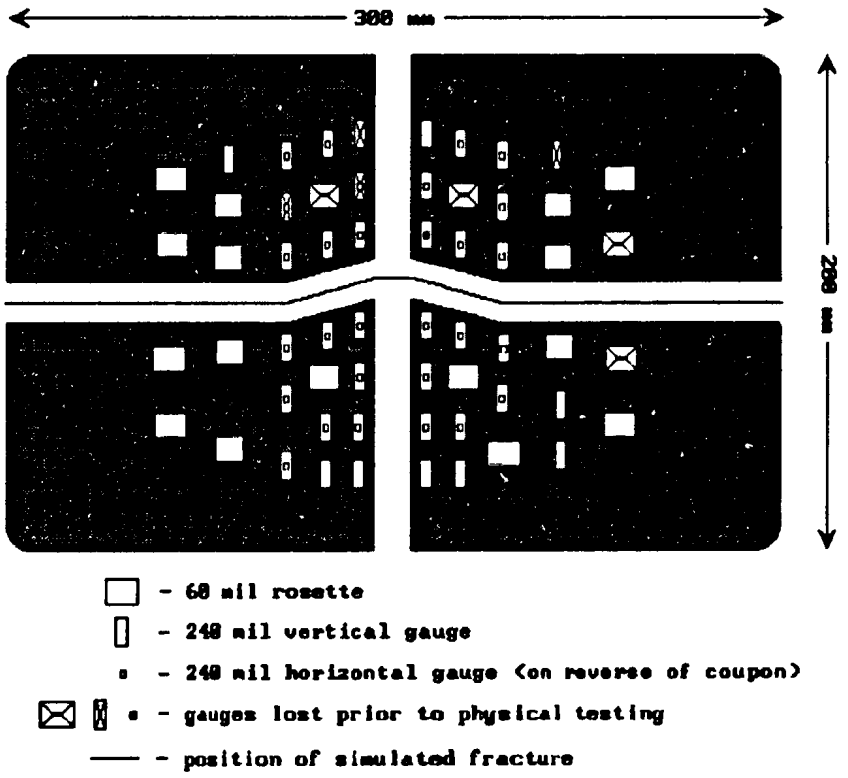

Figure 3-1. Geometry of concrete coupons with respect to final simulated fracture and approximate positions of strain gauges on the coupons.

4 days, the aluminum plate was removed and an upper concrete form was attached to the lower form (Figure 3-2c). The remaining coupons were then hung along the center line of this form, which was then filled with concrete and vibrated. The inside corners of both wooden forms were fitted with a concave wooden moulding to produce smoothly rounded edges and corners in the physical model to minimize stress concentrations.

After curing 28 days, the concrete model was removed from both forms and the upper and lower halves of the model were separated. The geotextile was removed and the two halves were carefully reassembled (Figure 3-2d). The resulting fracture was correlated, or mated, on the large scale by the asperity but not correlated at the small scale due to the texture of the geotextile fabric (Atkinson, 1987). Three gear clamps were then strapped around the model to hold it firmly together and prevent damage to the fracture surface. A 3 mm deep trench was ground into the sample along the outside trace of the fracture and the sides were then ground back to form 45° bevels (Figure 3-2d). This bevelled trench was used as a smooth seat for an inflatable packer that surrounded the outer fracture trace and sealed the fracture during permeability tests (related to a parallel research program not described in this thesis) and subsequent resin impregnation.

The model was cast into one half of the steel sample box using a mixture of high strength epoxy resin, fine and coarse silica sand and 4 mm to 8 mm diameter granite aggregate. After curing two days, the upper half of the steel sample box was bolted to the lower half using machined aluminum plates. The assembly was then turned over and the remaining half of the concrete model was cast into the other side of the sample box

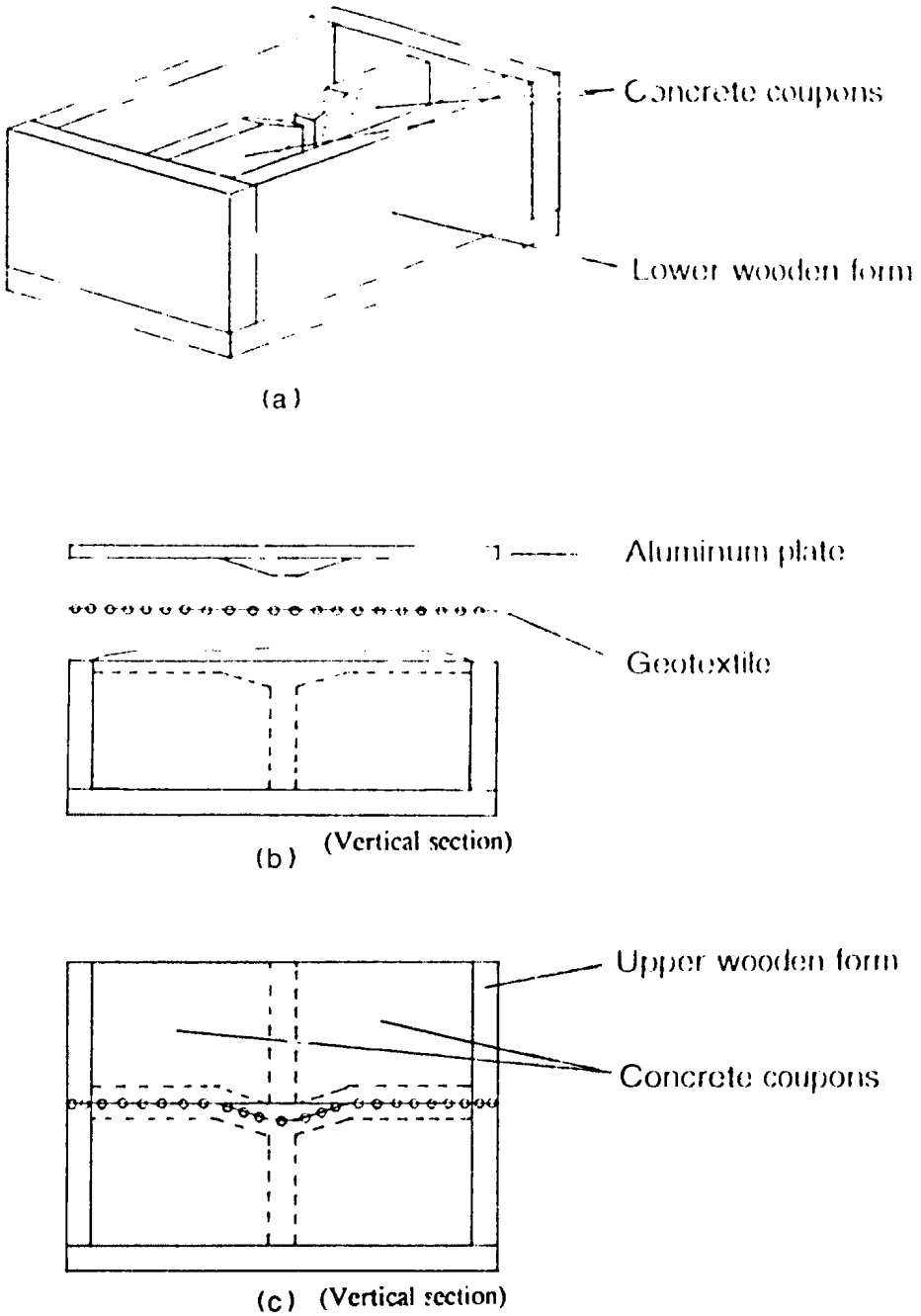

Figure 3-2. Construction of physical model showing (a) placement of coupons in lower wooden form, (b) mounding of wet concrete in lower form and pressing of geotextile into concrete using shaped aluminum plate to cast lower block, (c) placement of upper wooden form onto lower form and position of coupons in upper form to cast lower block (continued on next page...)

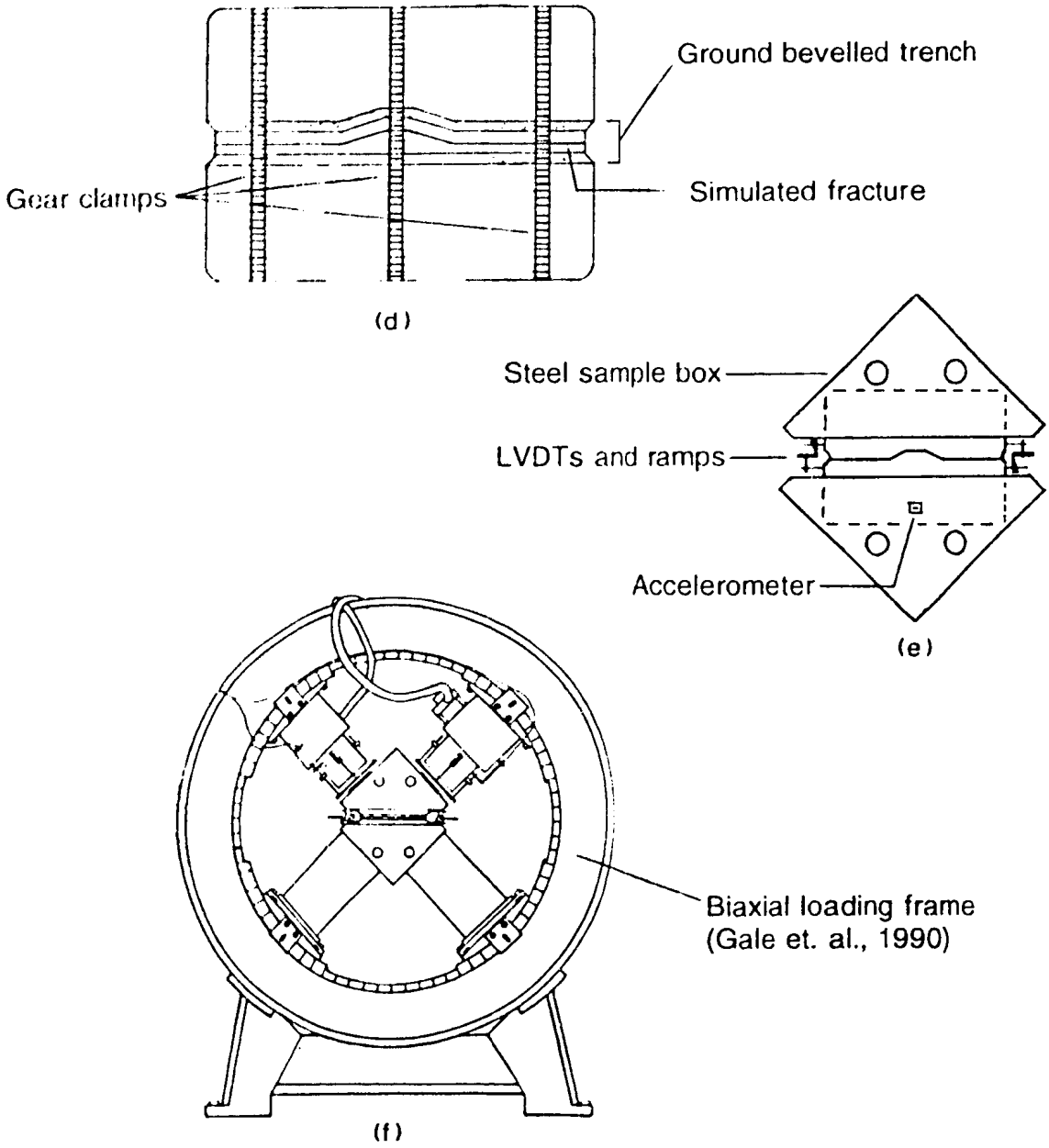

Figure 3-2. (...continued) (d) reassembled model after forms and geotextile removed, showing position of ground trench and ramps surrounding fracture trace, (e) position of model in steel sample box and (f) placement of steel sample box and model in biaxial frame.

(Figure 3-2e). The sample box was then placed into the biaxial loading frame using a small crane, the aluminum plates removed and the gear clamps ground off. The physical model was now ready for testing (Figure 3-2f).

3.2 Experimental Procedure and Data Reduction

A total of three normal and three shear loading cycles were conducted with load/displacement control provided by a MTS servo-controlled hydraulic system. All three normal loading cycles and the first shear cycle were conducted under load control, where the load applied by each actuator was varied by the frame operator using precision potentiometers. By changing the load applied by each actuator, the operator was able to apply the desired levels of normal and shear stress on the mean fracture plane. The final two shear cycles, however, were performed under displacement control using a PC based control program which modified the displacement produced by each actuator to maintain the desired normal and shear stress conditions. The control algorithm for this program is described in Appendix C. This arrangement provided excellent control of the stresses on the mean fracture plane and, more importantly, because the rate of travel of each piston was controlled, the control algorithm prevented large and potentially destructive shear displacements from occurring after peak shear strength was reached. Such controlled failure of the sample would not be possible under load control. Both loading arrangements maintained the desired stress on the fracture plane and did not restrict fracture normal displacement. Hence, the fracture plane was free to either close or dilate in response to the applied normal and shear loads.

Of the eighty eight strain gauges cast into the physical model, nine were lost prior to testing (Figure 3-1) due to disturbance during model fabrication or later due to gauge overheating. Of those gauges lost, one was horizontally oriented, four were vertically oriented and four were strain gauge rosettes. The remaining gauges were read using the in house designed MUGS strain gauge system (described in detail in Appendix B) and two HP 3497A data acquisition units. As mentioned earlier, additional electronic sensors were used to record loads, displacements and acoustic emissions during testing. First, load cells were mounted in line with each hydraulic actuator to measure the loads applied to the mean fracture plane. Secondly, an arrangement of eight LVDTs and eight machined steel wedges were mounted on the corners of the concrete model to measure fracture deformation (Figure 3-2e). Displacement data from these LVDTs were used to calculate overall fracture normal and shear displacement, and the rotation of the two halves of the model with respect to each other. (Refer to Gale et al. (1990) for a detailed description of the theory behind the use of the inclined plane approach as used with these sample LVDTs.) Finally, acoustic emissions (AE) generated by induced fracturing were monitored using an accelerometer with a 0 to 40 kHz frequency range. The accelerometer was fixed to a steel clamp and glued, using a quick setting epoxy, to the outside of the sample box (Figure 3-2e).

During testing, most of the data from the above instrumentation were acquired automatically using an 80386 IBM compatible microcomputer interfaced to a Keithley 500A Data Acquisition and Control unit. Data acquisition was accomplished using software written in a multitasking software environment named ViewDAC developed

specifically for the Keithley system (Keithley Asyst, 1992). The software stored instrumentation data in computer files at regular intervals, performed real time data analysis and displayed and graphed pertinent information on the computer screen. This enabled immediate assessment and monitoring of the test in progress to ensure that it was proceeding correctly.

During testing, a number of technical problems arose which complicated subsequent data analysis. First, the applied voltage used by the MUGS strain gauge system had to be reduced from its normal level of 10 V DC to 1.5 V DC to eliminate strain gauge overheating problems. As a result, the data recorded by the MUGS system during all loading cycles were much noisier than initially expected. This problem was overcome by applying a low pass convolution filter (Telford et al., 1990), with a minimum wavelength cutoff of 20000 seconds, to each strain gauge data record. This significantly reduced the noise and improved the data quality. An example of this procedure is given in Appendix D.

A second problem was associated with the strain gauges which were wired to the two HP data acquisition units. Due to wiring errors, no data from these gauges were recorded for the first normal loading cycle. During the second normal loading cycle, the data were masked by nonlinear strain gauge warming responses. The data from the second normal cycle, however, were recovered by determining the gauge self heating curve independently for each strain gauge data record and numerically subtracting this curve from the raw data record. The self heating curve for each gauge was determined by fitting a curve of the form $f(t) = At^b$ to the raw data set so that the curve was

coincident to and parallel with the beginning and ending regions of raw data curve. This was considered to be an acceptable approach since the beginning and ending regions of unmasked strain gauge data records were approximately constant and plotted as horizontal lines on graphs of strain gauge value versus elapsed time. Constants A and b were determined using an itterational technique on a computer spreadsheet and an example is provided in Appendix D.

A third problem involved heterogeneity and inconsistency in the strains recorded by the strain gauge rosettes. This probably occurred because the gauge length of the 60 mil strain gauge rosettes was less than the minimum value suggested by Berwanger (1968) as reported in Section 2-3 or because of thermal interaction between the closely spaced rosette strain elements. It was assumed that some of the strain gauge data would be useable, but post test analysis indicated that most strain gauge rosette data were inconsistent when compared to strains measured by adjacent 240 mil single gauges. Thus the rosette data were not used in the analysis of the experimental results. Fortunately, most of the strain gauge rosettes, as shown in Figure 3-1, were not located in regions of maximum strain which occurred near the asperity.

A fourth and final problem encountered was the "bumping" of the LVDTs mounted on the four corners of the model during manipulation of the sample packer and packer retainer. This resulted in the recording of erroneous displacements. These bumps were identified in and removed from each LVDT data record and consisted of those data which occurred when the packer retainer was being adjusted and which were uncorroborated at other LVDT locations. Care was taken not to remove legitimate

displacement jumps, such as those due to fracture creep or sudden frictional slip, which were not associated with any recorded packer or retainer manipulation.

Once all the load, displacement and strain data were corrected and reduced to physical units, they were presented as graphs of fracture normal stress versus normal displacement, graphs of shear stress versus shear displacement and as contoured plots of internal strain overlain on a cross section perpendicular to the fracture plane and parallel to the shear direction. Note that contour lines on these diagrams are not labelled and instead the original data values used to generate the contour plots are included at their actual locations. Appendix F provides tables of the strain values recorded during the physical experiment, as well as approximate stresses (calculated using the procedure outlined below) and numerically predicted stresses for comparison.

Preliminary analysis of the internal strains revealed that permanent strain in the physical model was significant relative to the total strain recorded. Therefore, all the contoured strain fields presented have been reset to zero strain at the start of each loading cycle. Thus, the strains presented only represent the strain accumulated during the individual loading cycle, not the total accumulated strain. Examination of these strain fields indicates that strains are very small, typically less than 0.1%. At that strain level, we can assume that the deviation of the principal stress and strain orientations is not significant and that the internal stress field produced during each loading cycle has a size and shape very similar to the measured strain field. For comparison between laboratory and numerical model results, an approximate conversion factor of 20 $\mu\epsilon$ per 1 MPa stress (calculated using Young's Modulus data from Table 2-1) was used to estimate stress

values from internal strain measurements. However, since the concrete used to construct the physical model is relatively weak in tension, this rationale is not valid for tensile strains, where tensile fracturing would probably occur at low strain levels. As well, this conversion factor was estimated from compressive tests only and would not be applicable for tensile strains. Therefore, no stresses are assigned to tensile strains.

3.3 Analysis of Biaxial Testing Results

3.3.1 Normal Loading Cycles

Figure 3-3 is a plot of the normal stress versus mean normal fracture displacement recorded for the three normal loading cycles and for the normal loading portions of the three shear cycles. The displacements for each loading cycle have been referenced to the initial reading at the beginning of each cycle and hence each cycle is referenced to zero displacement (Figure 3-3). The maximum normal stress applied during the first normal loading cycle was 13.8 MPa but, after a sustained burst of AE (numbering in the hundreds of counts per 10 second interval) was encountered, the load was quickly reduced to 13.4 MPa. This stress level was then the maximum normal stress applied for the remaining normal loading cycles. The three shear cycles were conducted at constant fracture normal stresses of 2, 8 and 10 MPa, respectively. The abrupt jump in normal stress (from 8.2 to 8.9 MPa) shown at the peak of the second shear cycle was due to an operator error and was only applied for a few seconds.

Analysis of the normal displacement curves for the three normal loading cycles indicates that permanent closure was greatest for the first cycle and that the closure

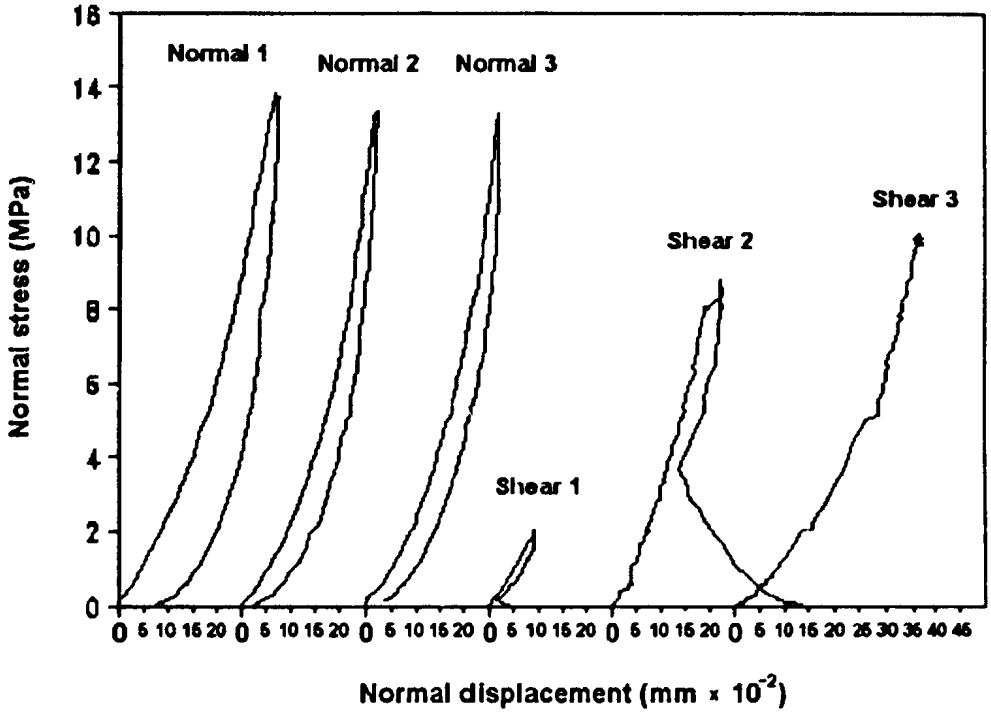

Figure 3-3. Plots of normal stress versus normal displacement for the three normal loading cycles and the normal loading portions of the shear loading cycles.

behaviour for the second and third cycles was nearly identical. These observations indicate that the fracture was predominantly seated during the first normal loading cycle, a situation consistent with the normal closure behaviour observed from testing of the 152 mm diameter fractured cylinder in Section 2-4. These results validate the assumption, made during predictive numerical modelling, that normal closure behaviour for the second and subsequent normal cycles would be the same.

Analysis of the normal displacement curves for the shear cycles shows that the application of normal load for the second and third shear cycles was more irregular than during all previous cycles. This is most likely the result of the control algorithm for

displacement control (Section 3-2) which induced slight fluctuations in the applied fracture loads. Further analysis revealed an unexpected result, namely the abrupt change in slope occurring on the unloading portions of the curves for the first and second shear cycles. These changes in slope indicate that the fracture began to close during the removal of normal load. This suggests that some portion of the shear displacement applied during these shear cycles was accommodated by dilatant climbing of the asperity restraining bend. During unloading, frictional shear strength of the fracture at the compressed asperity bend decreased until it was exceeded and the fracture began to slide back down the bend. This scenario is consistent with observed fracture dilation during the shear portion of the second shear loading cycle, as is discussed later.

Analysis of the internal strains recorded during normal loading indicate that the symmetrical stress patterns predicted by the numerical modelling did not occur. In contrast, measured strain patterns are highly asymmetrical surrounding the asperity, but are consistent between successive cycles. Figure 3-4 presents plots of (a) vertical and (b) horizontal strain recorded during the first normal loading cycle. These results show an overall increase in strain magnitude with increasing normal load, with the highest strains recorded immediately above and below the asperity bend. At maximum applied normal stress, vertical strains are greatest directly above the asperity bend while horizontal strains are greatest directly below it. This pattern indicates that the ϵ_1 direction is more vertically oriented (as opposed to horizontally oriented) just above the asperity bend and more horizontally oriented just below it. At peak normal load, a tensile zone appears in the upper left hand corner of the horizontal strain field which then

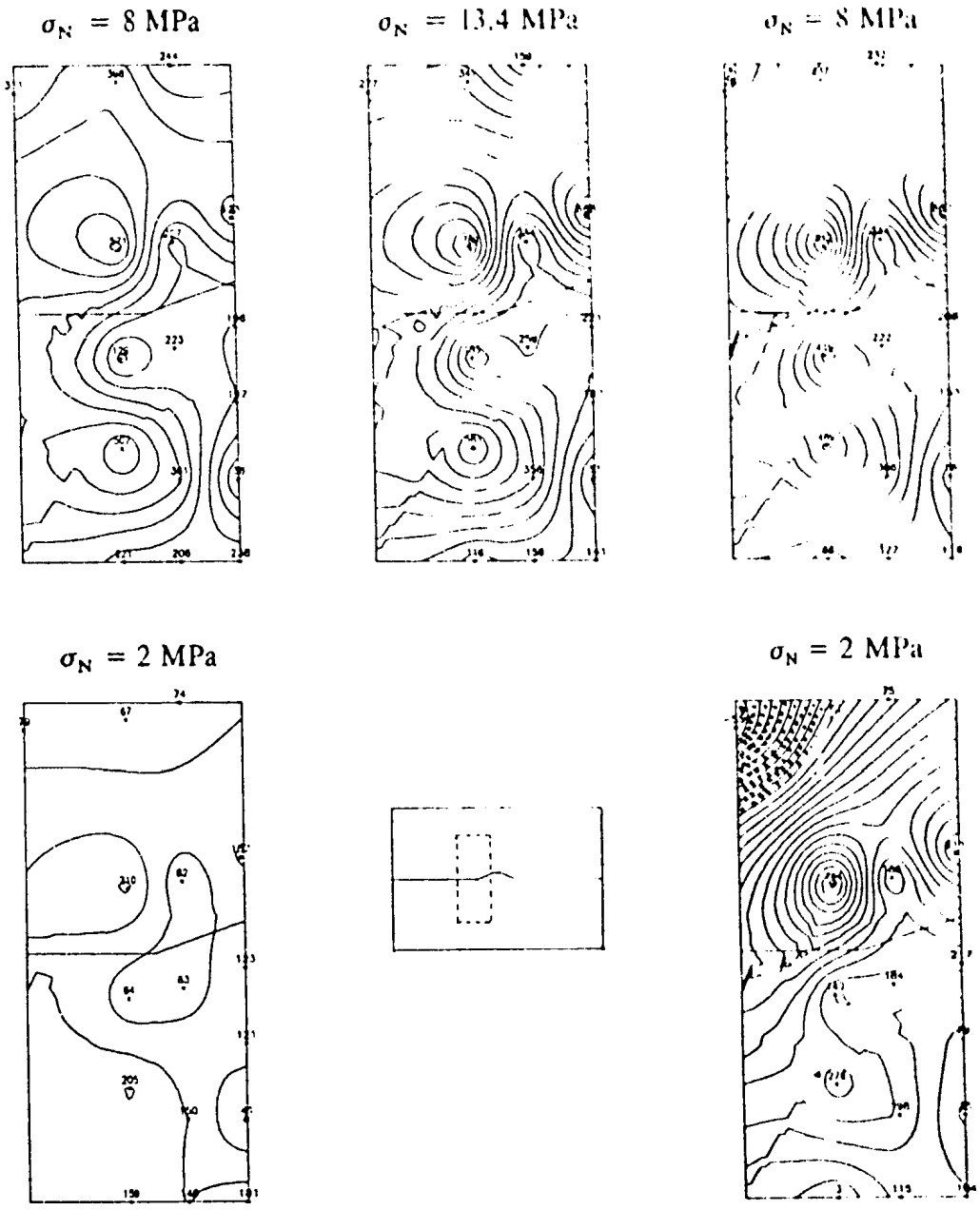

Figure 3-4 (a). Contours of vertically oriented strain recorded during the first normal loading cycle. The loading path is clockwise and the contour interval is 50 $\mu\epsilon$. Stipples indicate tensile strains and the size of the strain field is 37 mm horizontal by 146 mm vertical. The position of the strain field in the concrete model is as indicated in the inset.

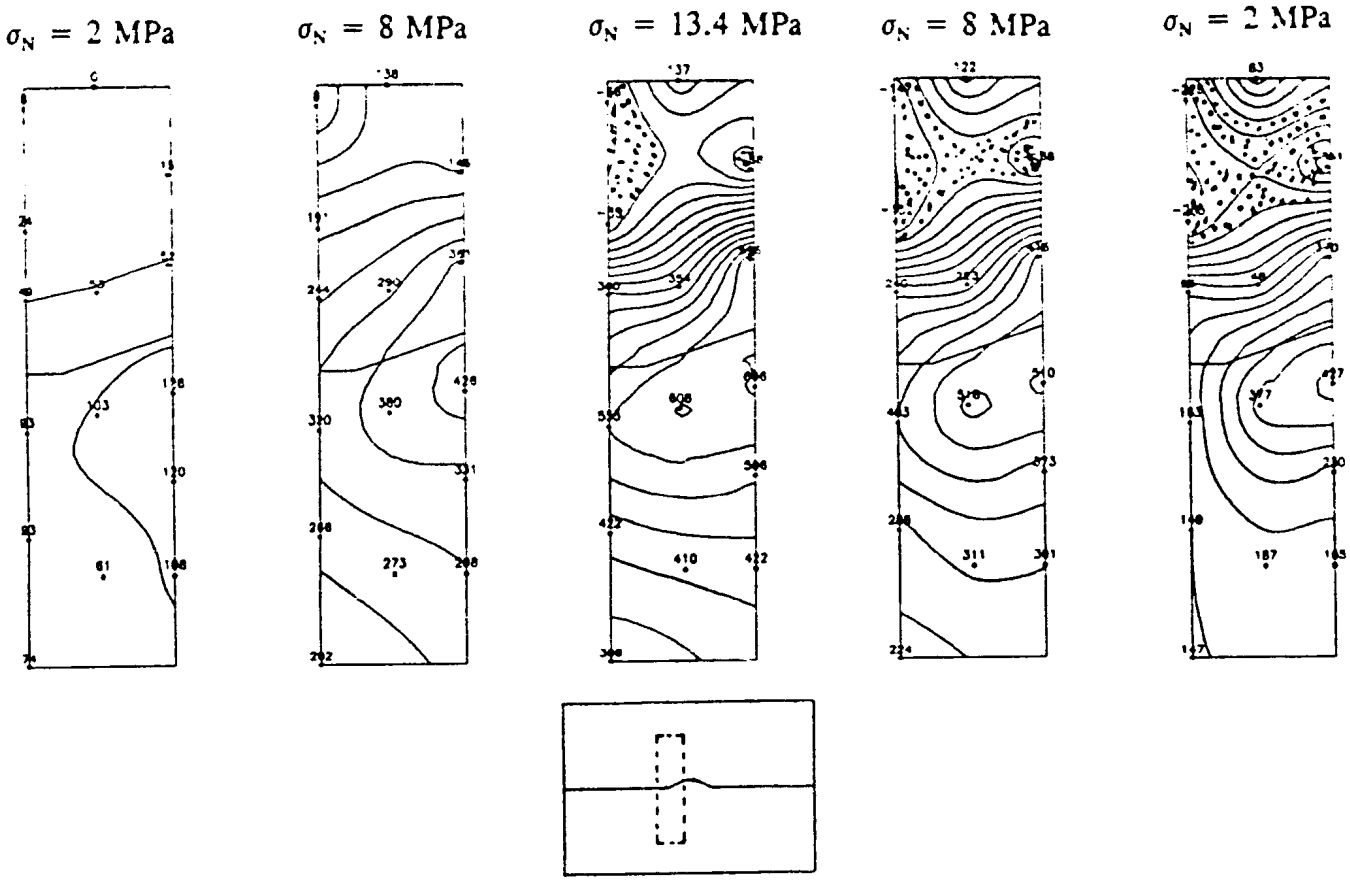

Figure 3-4 (b). Contours of horizontally oriented strain recorded during the first normal cycle. The loading path is from left to right and the contour interval is 50 $\mu\epsilon$. Stipples indicate tensile strain and the size of the strain field is 66 mm horizontal by 145 mm vertical. The position of the strain field in the concrete model is as indicated in the inset.

increases in magnitude during unloading. A similarly positioned tensile zone is observed initiating and growing in the vertical strain field during the unloading portion of the cycle. Since a sustained AE burst occurred concurrently with this, it is probable that induced tensile fracturing may have occurred at the peak load which then dilated as the normal load on the fracture was removed. Finally, during unloading, a large portion of the strains observed at peak normal load are preserved which indicates that there was significant plastic strain in the sample. For example, in the vertical strain field compressive strains immediately above the asperity bend are approximately three times larger at 2 MPa normal stress on the unloading portion of the cycle than at 2 MPa normal stress on the loading portion of the cycle. This result is not entirely unexpected, since a similar permanent set was observed during uniaxial testing of the intact 152 mm diameter cylinder in Section 2-4; refer to Figure 2-4 and note that the axial strain at 2 MPa axial stress on the unloading portion of the curve is approximately three times the axial strain recorded at 2 MPa on the loading portion of the cycle. Analysis of the strains recorded at σ_N = 8 MPa on the loading portion of the cycle indicates approximate stress values of 29 MPa directly above the asperity bend and 21 MPa directly below. These are considerably higher than the corresponding stresses of 7 and 6 MPa predicted by the numerical model for that load cycle and fracture normal stress (Figure A-1 in Appendix A).

Strain contour plots for the second and third normal loading cycles (given in Figures 3-5 and 3-6) show the strain field on both sides of the asperity and highlight it's pronounced asymmetry. Both loading cycles show approximately the same strain patterns

and magnitudes, an observation that is consistent with their similar normal displacement curves (Figure 3-3). These figures show the initial presence and growth of horizontal and vertical tensile zones below the right hand asperity bend and the growth of compressive zones above the asperity and below the left hand bend. Compressive strains were greatest at peak normal load. In both cycles, the maximum vertical strains occurred below the toe of the left hand bend, with corresponding approximate stresses of 30 MPa during the second cycle and 35 MPa during the third cycle. Similarly, the maximum horizontal strains for both cycles occurred above the asperity step, with corresponding approximate stresses of 28 MPa during the second cycle and 23 MPa during the third cycle. During unloading, the observed permanent set at the end of both the second and third cycles was less pronounced than at the end of the first normal loading cycle. Tensile strains generally increased throughout the loading cycle and, after the peak stress, new tensile zones were formed in the upper left hand corner of the vertical strain field and in both upper corners of the horizontal strain field. These observations were consistent with non uniform mating of the fracture on the right hand asperity bend, as is schematically shown in Figure 3-7. This schematic indicates that as the applied normal load increases, compressive stresses increase to the left of the asperity and tensile stresses increase to the right.

σ_N = 13.4 MPa

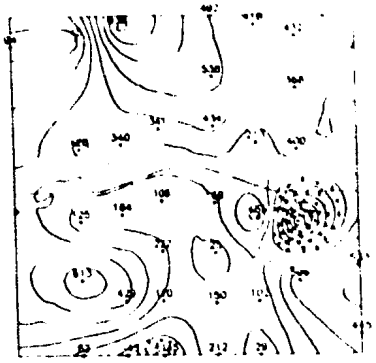

σ_N = 8 MPa

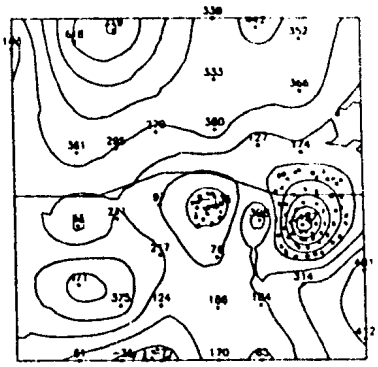

σ_N = 8 MPa

σ_N = 2 MPa

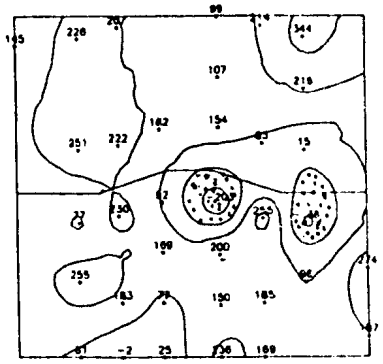

σ_N = 2 MPa

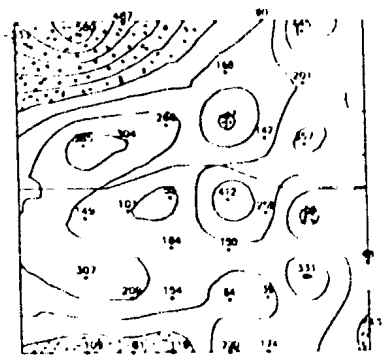

Figure 3-5 (a). Contours of vertically oriented strain recorded during the second normal loading cycle. The loading path is clockwise and the contour interval is 100 $\mu\varepsilon$. Stipples indicate tensile strains and the size of the strain field is 155 mm horizontal by 150 mm vertical.

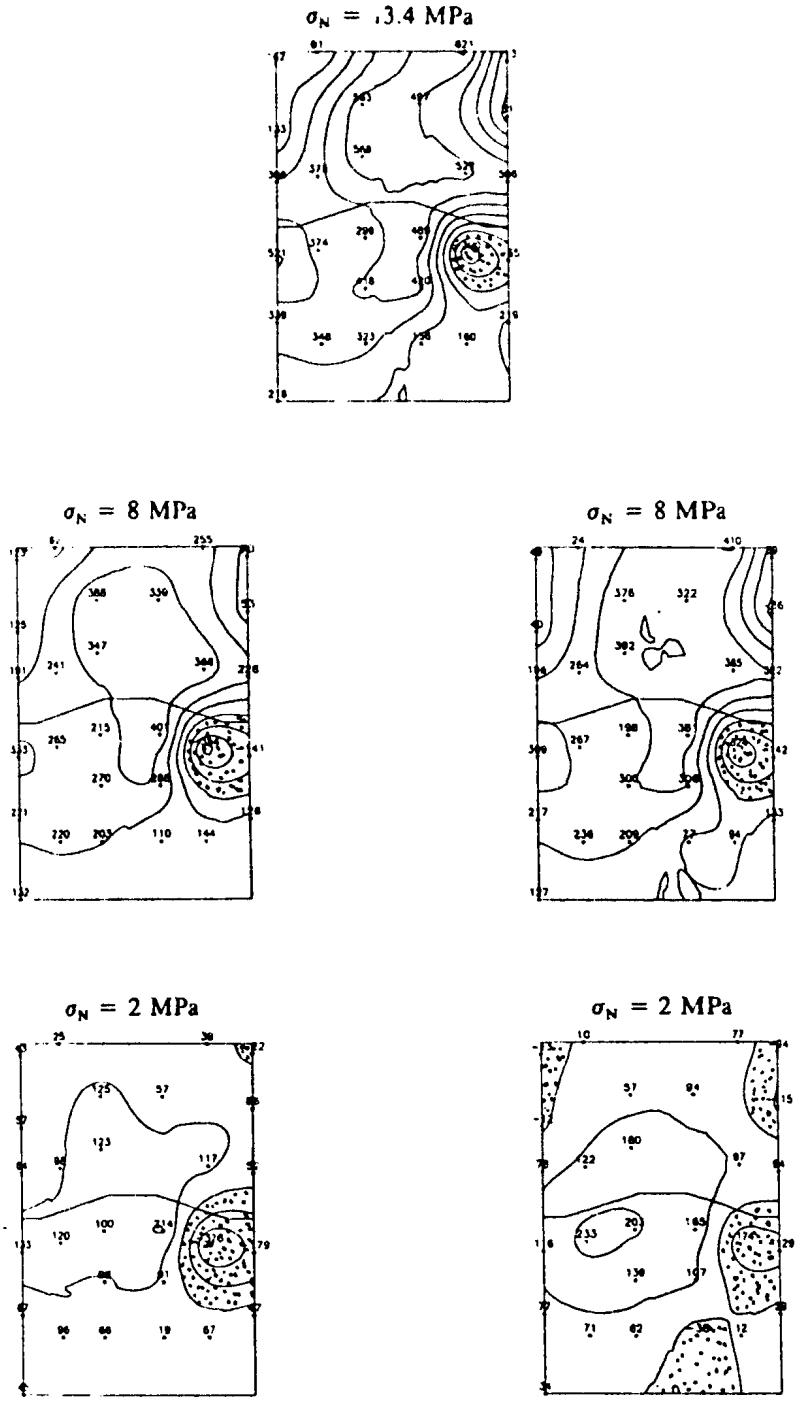

Figure 3-5 (b). Contours of horizontally oriented strain recorded during the second normal loading cycle. The loading path is clockwise and the contour interval is 100 $\mu\epsilon$. Stipples indicate tensile strains and the size of the strain field is 99 mm horizontal by 146 mm vertical.

σ_N = 13.4 MPa

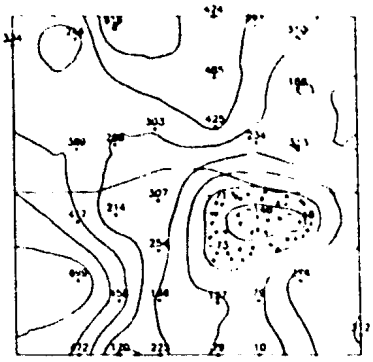

σ_N = 8 MPa

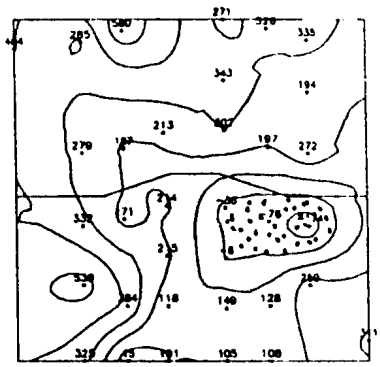

σ_N = 8 MPa

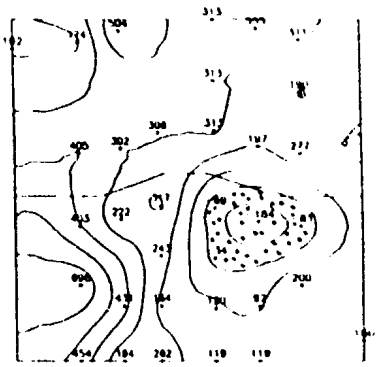

σ_N = 2 MPa

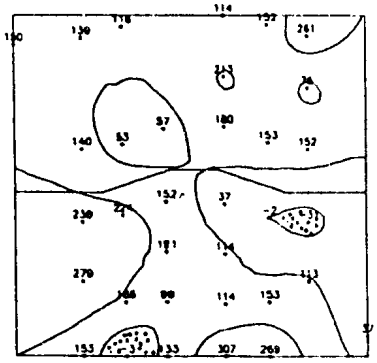

σ_N = 2 MPa

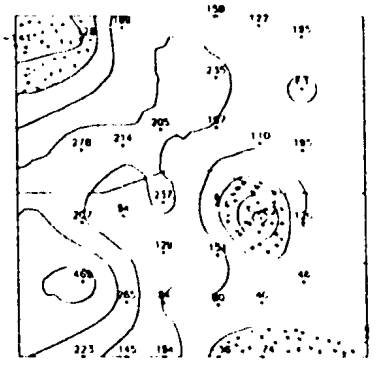

Figure 3-6 (a). Contours of vertically oriented strain recorded during the third normal loading cycle. The loading path is clockwise and the contour interval is 100 $\mu\varepsilon$. Stipples indicate tensile strains and the size of the strain field is 155 mm horizontal by 150 mm vertical.

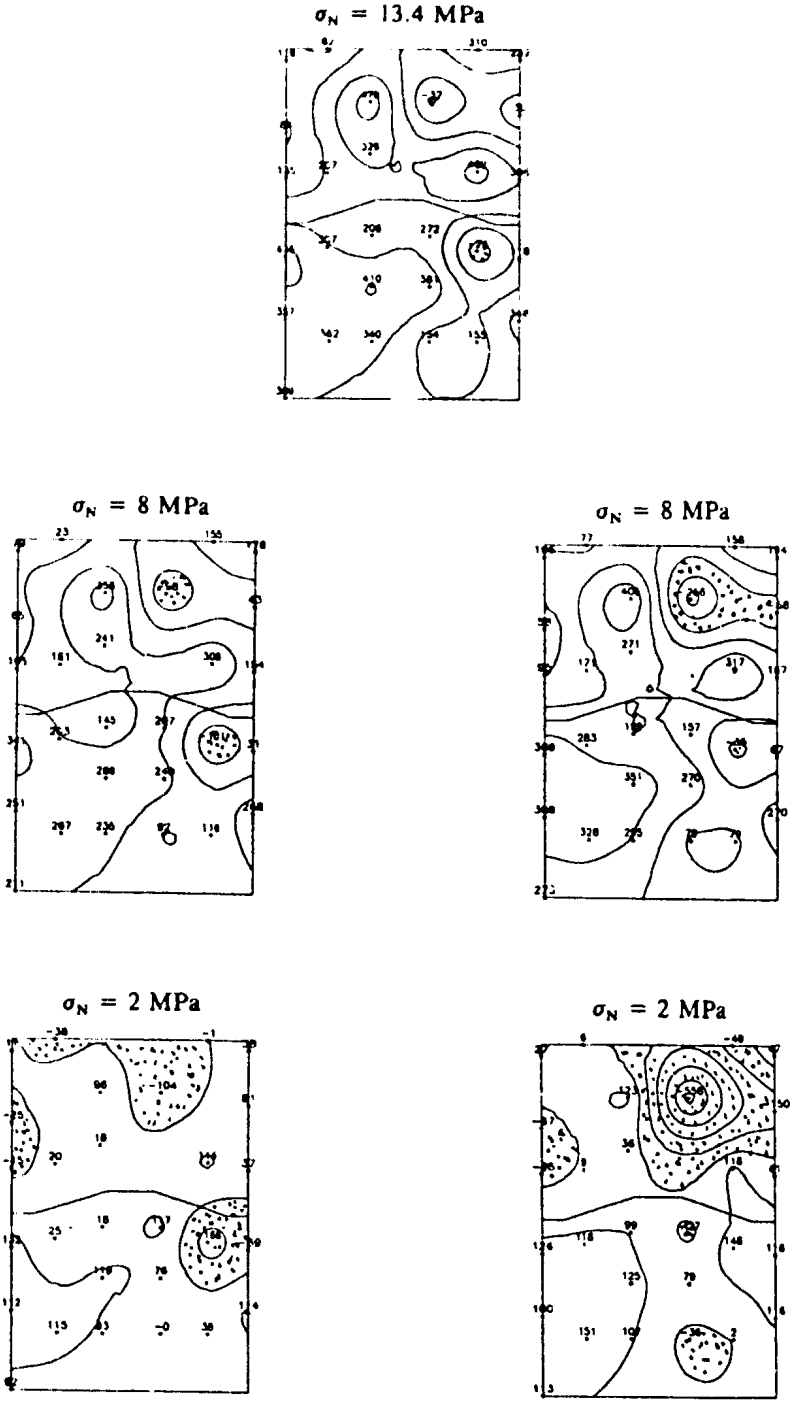

Figure 3-6 (b). Contours of horizontally oriented strain recorded during the third normal loading cycle. The loading path is clockwise and the contour interval is 100 $\mu\epsilon$. Stipples indicate tensile strains and the size of the strain field is 99 mm horizontal by 146 mm vertical.

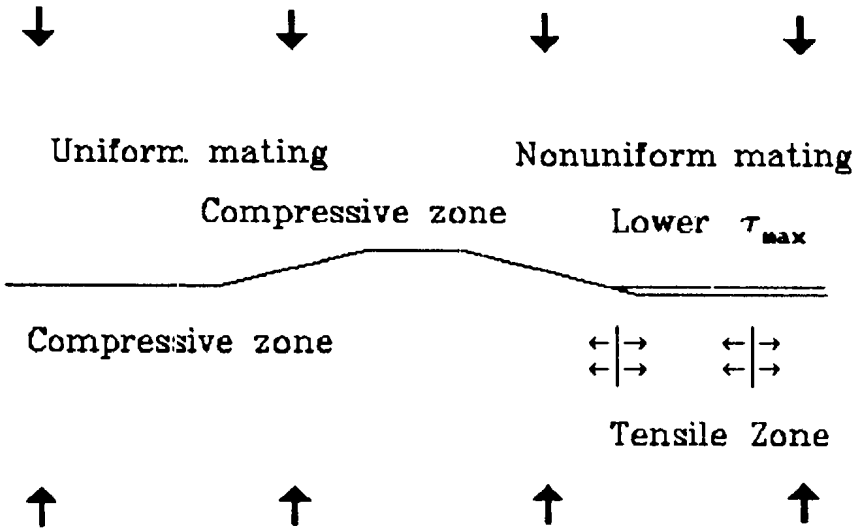

Figure 3-7. A schematic diagram proposing that non uniform fracture mating at the right hand asperity bend caused the asymmetrical strain patterns observed during normal loading.

3.3.2 Shear Loading Cycles

Figure 3-8 plots shear displacement versus shear stress for the three shear loading cycles conducted at constant fracture normal stresses of 2, 8 and 10 MPa, respectively.

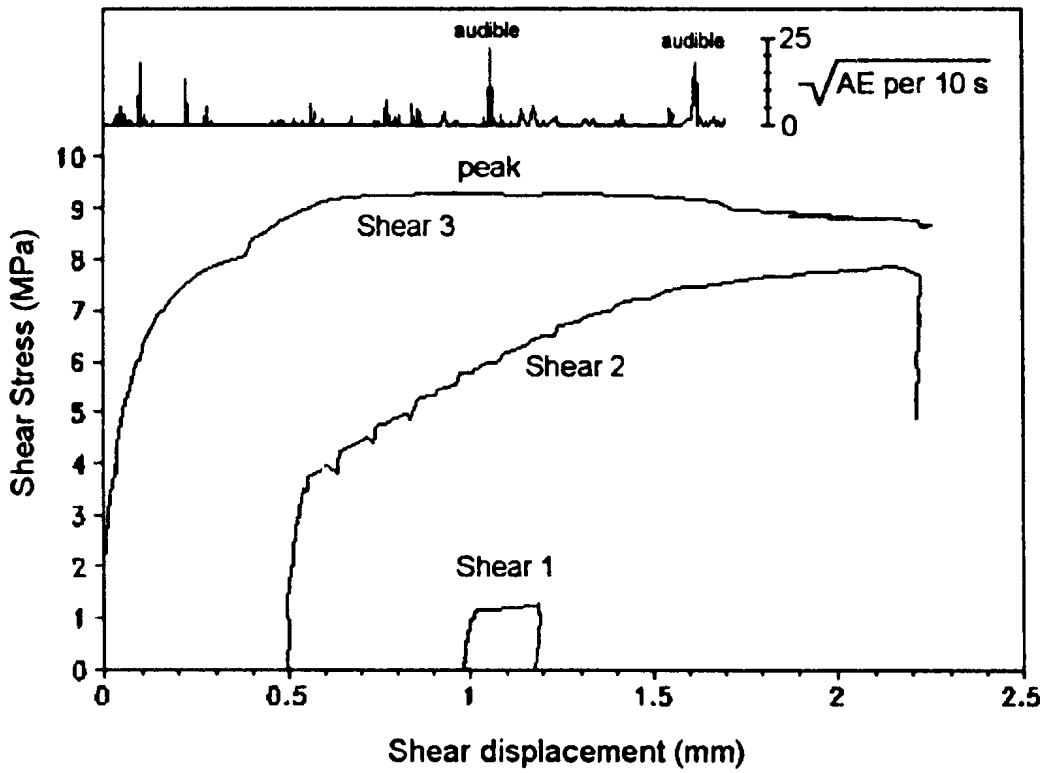

Figure 3-8. Plots of shear stress versus shear displacement for the three shear loading cycles. Plotted above the curve for the third shear cycle are the square root of the AE measured during that cycle.

(Note that the curves in Figure 3-8 have been artificially separated for clarity by beginning at 0.5 mm intervals.) These curves indicate that displacements during shear loading were more complex than during normal loading. Each shear cycle followed a unique deformational path which, as subsequent analysis indicated, was the product of

the loading procedure, the applied normal stress and the loading history. During the first shear cycle, most of the 200 μm total shear displacement occurred as a result of a very small increase in shear stress at τ = 1.21 MPa. It is likely that the fracture began to slip rapidly when frictional shear strength was exceeded (since this shear test was conducted under load control with no control over the rate of actuator movement) until it was stopped at the restraining bend. Visual inspection of the fracture after slip confirmed that there was a tight fit at the restraining bend and dilated porosity at the releasing bend with no visible induced secondary fracturing. Analysis of shear stress magnitude when slip occurred indicates a mobilized friction angle of 31°, which is in good agreement with a friction angle of 33° predicted by the Barton-Bandis shear strength criteria (Equation 1-1, using the Barton-Bandis parameters determined in Section 2-4, namely JRC = 3.0, JCS = 52.4 MPa and ϕ_r = 29°) for the small scale fracture roughness.

During the second shear cycle, significant shear displacement began at τ = 3.8 MPa. This indicates a drop in mobilized friction angle to 25° and suggests that primary small scale roughness was no longer contributing to mobilized shear strength and that friction along the planar fracture regions had fallen to it's residual value. This could have resulted from damage to the fracture surface caused by shear slip during the first shear loading cycle or from dilation effects associated with displacement up the restraining bend. Initial shear displacement was characterized by a series of abrupt periodic slips, as indicated by sharp drops in the shear stress. This stick slip type of behaviour (Brace and Byerlee, 1966) was probably enhanced by the slow, controlled rate of shear displacement which impeded the quick recovery of drops in shear stress

associated with slipping. This behaviour stopped at τ = 5.5 MPa. At τ = 7.2 MPa, there was an abrupt decrease in the slope of the curve. Shear stress continued to increase to 7.8 MPa which was the maximum shear stress that could be applied by the loading frame at the given constant normal load (Gale et al., 1990). The sample was then visually inspected and unloaded. The visual inspection identified a small shear crack near the face of the restraining bend and a vertical tensile crack at the top of the restraining bend. No AE was produced which could have identified the time of formation of these cracks, but they probably coincided with the abrupt change in slope, and hence decrease in shear strength, observed at τ = 7.2 MPa.

During the third shear cycle, initiation of shear displacement occurred gradually over the stress range τ = 3.0 to 7.0 MPa. This differs from the initiation of shear displacement in both previous shear cycles, which were characterized by sharp breaks in the slopes of their shear displacement curves (Figure 3-3). Between τ = 7.0 and 9.0 MPa the shear displacement curve had an approximately linear slope. At τ = 9.2 MPa, the curve became almost horizontal, indicating that the fracture was stably sliding up the restraining bend. Macroscopic sample failure occurred at τ = 9.25 MPa after the fracture had displaced an additional 400 μm. Failure was preceded by a short sustained interval of AE and occurred concurrently with an audible bang and an AE burst of 499 counts per 10 second interval, as shown in Figure 3-8. The fracture was allowed to displace further to ensure that the peak had been reached, during which one other large AE burst and audible bang were recorded. The fracture then came to rest at a residual shear strength of 8.56 MPa and was resin impregnated and left to cure overnight with

the load on the sample being maintained. Macroscopic failure of the sample at τ = 9.25 MPa provides a mobilized friction angle of 43°, which corresponds to the sum of the 25° residual friction angle determined from the second shear loading cycle and the 18° angle of the restraining bend. Once again, this indicates that small scale roughness did not significantly contribute to mobilized shear strength.

Analysis of internal strains during these shear cycles confirmed that each loading cycle followed a unique deformational path. At the start of the first shear cycle, as shown in Figure 3-9, both vertical and horizontal strain fields were similar to those at previous normal cycles at 2 MPa normal stress. As shear stress increased to 1 MPa, both vertical and horizontal strains surrounding the restraining bend increased and there was growth of tensile zones above and below the releasing bend. After shear slip at τ = 1.23 MPa, however, compressive strains in the region surrounding the restraining bend decreased and a new vertical tensile zone developed at it's base. The measured strains indicate that the approximate compressive vertical stresses above the restraining bend were 11 MPa before slip and 8 MPa after slip, and horizontal stresses below the restraining bend correspondingly changed from 4 MPa to 2 MPa. This pattern indicates that when shear slip occurred, overall compressive strain was partially relieved and the compression of the restraining bend placed the region just below it into tension. This post slip strain pattern was preserved during shear unloading, indicating that it was permanent.

Strain plots for the second shear cycle, given in Figure 3-10, show the growth of both vertical and horizontal compressive strain zones surrounding the restraining bend

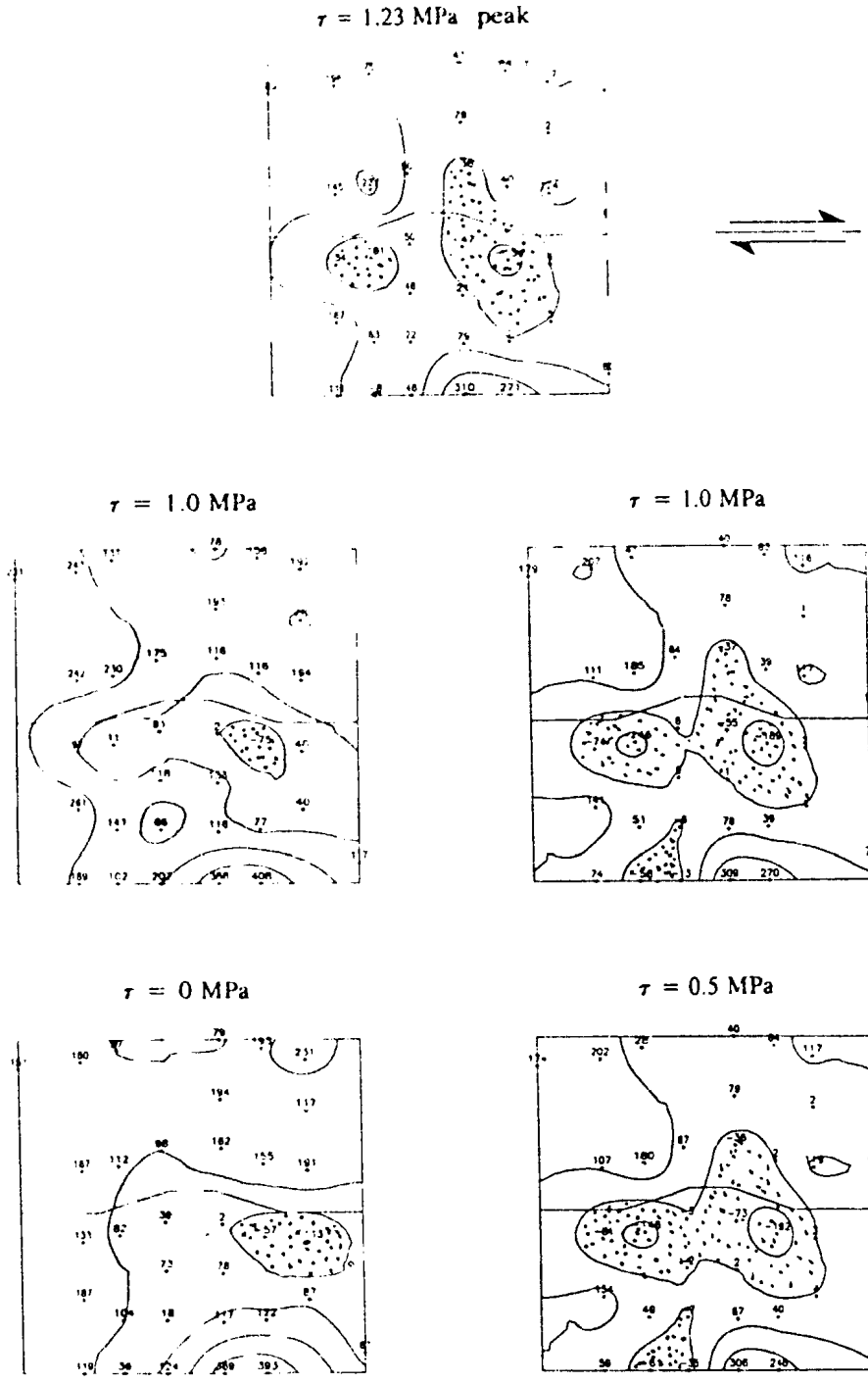

Figure 3-9 (a). Contours of vertically oriented strain recorded during the shear portion of the first shear loading cycle. The loading path is clockwise, the contour interval is 100 $\mu\epsilon$ and the shear sense is as indicated. Stipples indicate tensile strains and the size of the strain field is 155 mm horizontal by 150 mm vertical.

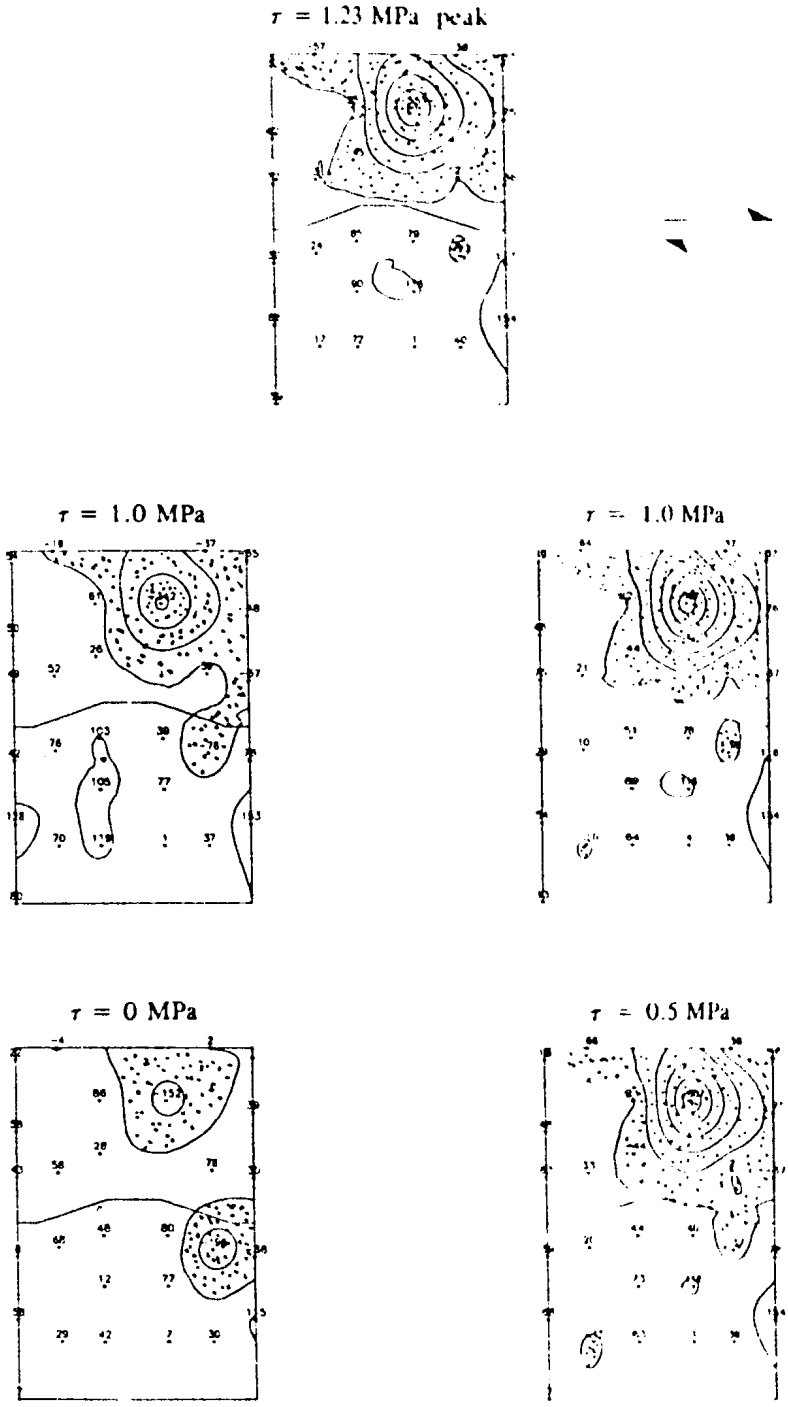

Figure 3-9 (b). Contours of horizontally oriented strain recorded during the shear portion of the first shear loading cycle. The loading path is clockwise, the contour interval is 100 $\mu\epsilon$ and the shear sense is as indicated. Stipples indicate tensile strains and the size of the strain field is 99 mm horizontal by 146 mm vertical

as shear stress was increased. At peak shear, the maximum vertical and horizontal strains occur below the loaded face of the restraining bend and have approximate corresponding stresses of 60 and 89 MPa, respectively. Vertical strains show the growth of a pre-existing tensile zone beneath the releasing bend and horizontal strains show the initiation and growth of tensile zones above both the restraining and releasing bends. The greatest increase in both compressive and tensile strains occurred during the interval from τ = 7 to 7.8 MPa. This was associated with the change in slope of the shear displacement curve (Figure 3-8) and the probable formation of the observed tensile and shear cracks. During this transition, the maximum compressive vertical strain moved from above to below the restraining bend, indicating a local rotation of the ϵ_1 direction towards the horizontal. Although predictive numerical modelling suggested that the sample should have macroscopically failed during this shear cycle, it did not. The cause of this discrepancy will be proposed during later discussion of these results.

Figure 3-11 provides plots of the strain fields observed during the third and final shear cycle. These results indicate that at the start of normal loading, the fracture was partially displaced up the restraining bend, most likely an artifact of large shear displacement with only partial recovery during the second shear cycle. This is evident from the vertical strain contours at τ = 1 MPa, which show a large compressive zone above the restraining bend and a large tensile zone below the releasing bend. The magnitude of strains in the vertical compressive zone initially increased with increasing shear stress, resulting in a computed stress change of approximately 91 to 104 MPa over the interval τ = 1 to 6 MPa. From τ = 6 to 8 MPa, however, this pattern is reversed,

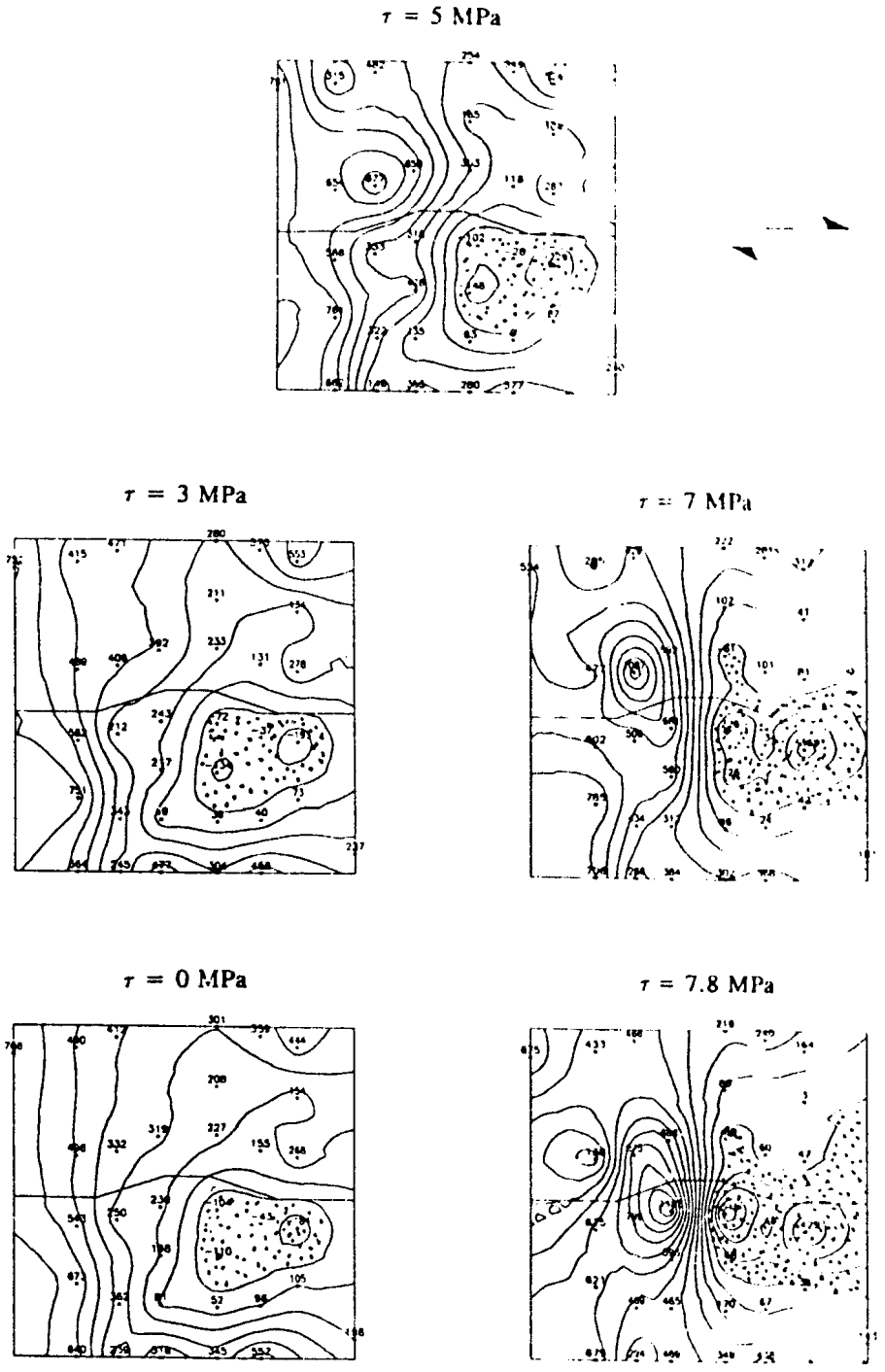

Figure 3-10 (a). Contours of vertically oriented strain recorded during the shear portion of the second shear loading cycle. The loading path is clockwise, the contour interval is 100 $\mu\varepsilon$ and the shear sense is as indicated. Stipples indicate tensile strains and the size of the strain field is 155 mm horizontal by 150 mm vertical.

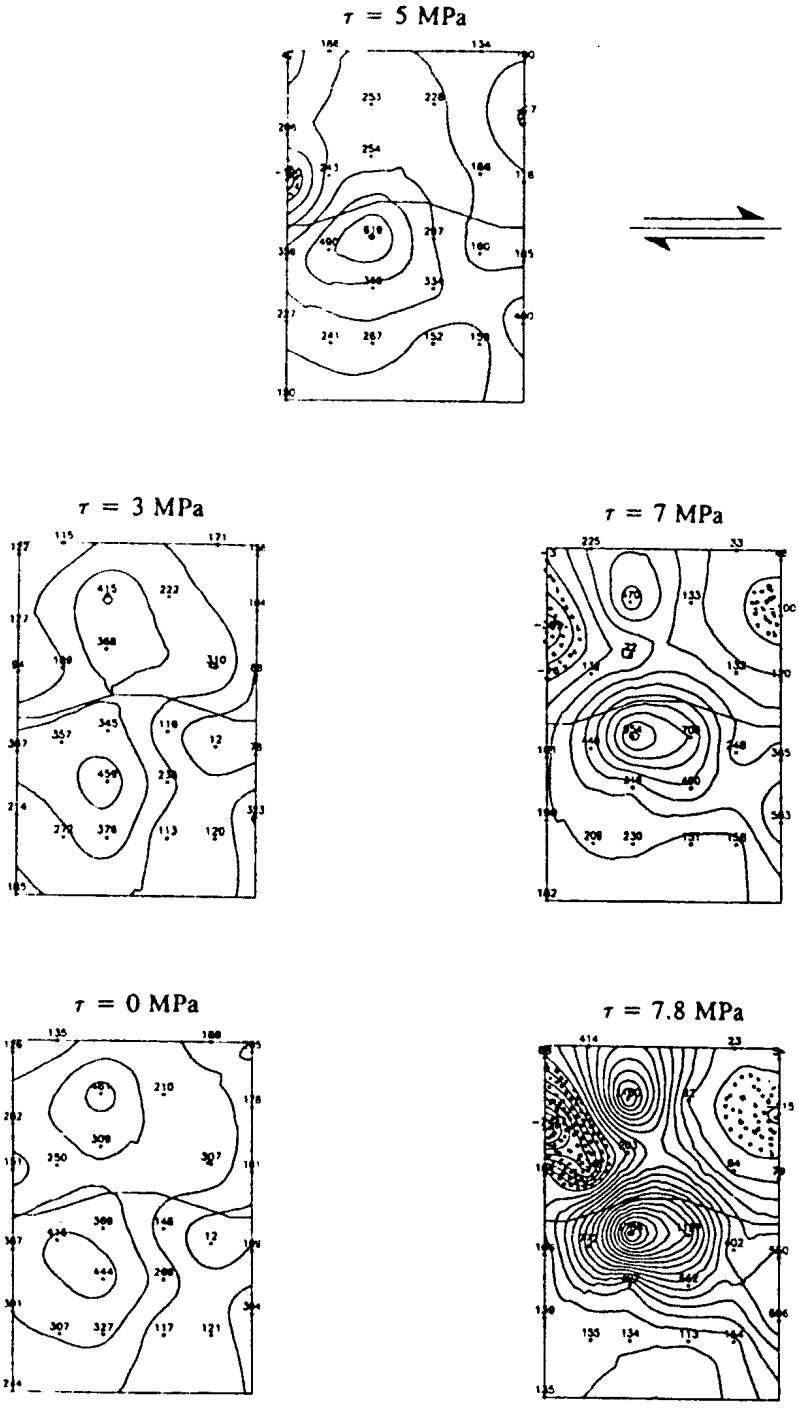

Figure 3-10 (b). Contours of horizontally oriented strain recorded during the shear portion of the second shear loading cycle. The loading path is clockwise, the contour interval is 100 $\mu\epsilon$ and the shear sense is as indicated. Stipples indicate tensile strains and the size of the strain field is 99 mm horizontal by 146 mm vertical.

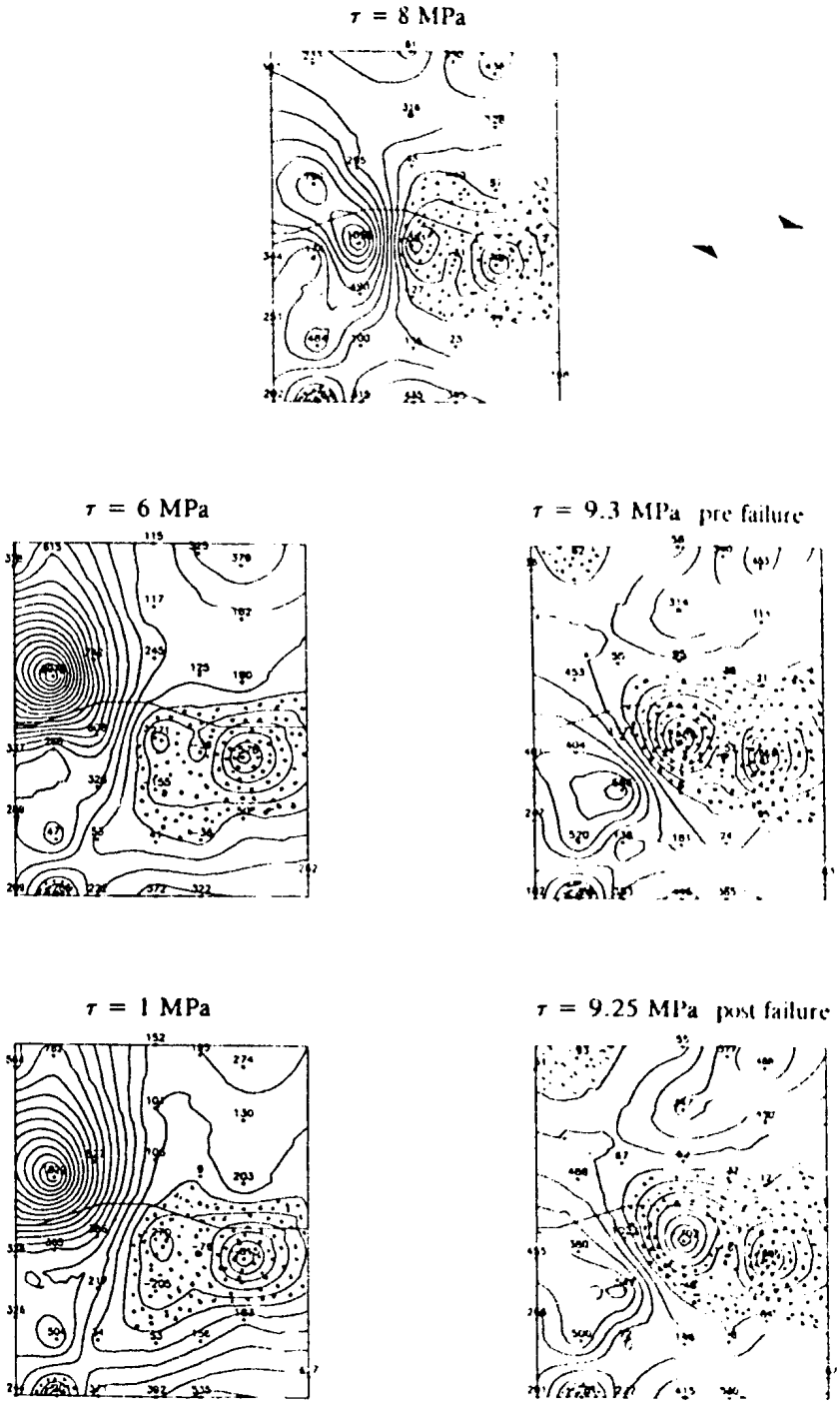

Figure 3-11 (a). Contours of vertically oriented strain recorded during the shear portion of the third and final shear loading cycle. The loading path is clockwise, the contour interval is 100 $\mu\varepsilon$ and the shear sense is as indicated. Stipples indicate tensile strains and the size of the strain field is 126 mm horizontal by 100 mm vertical.

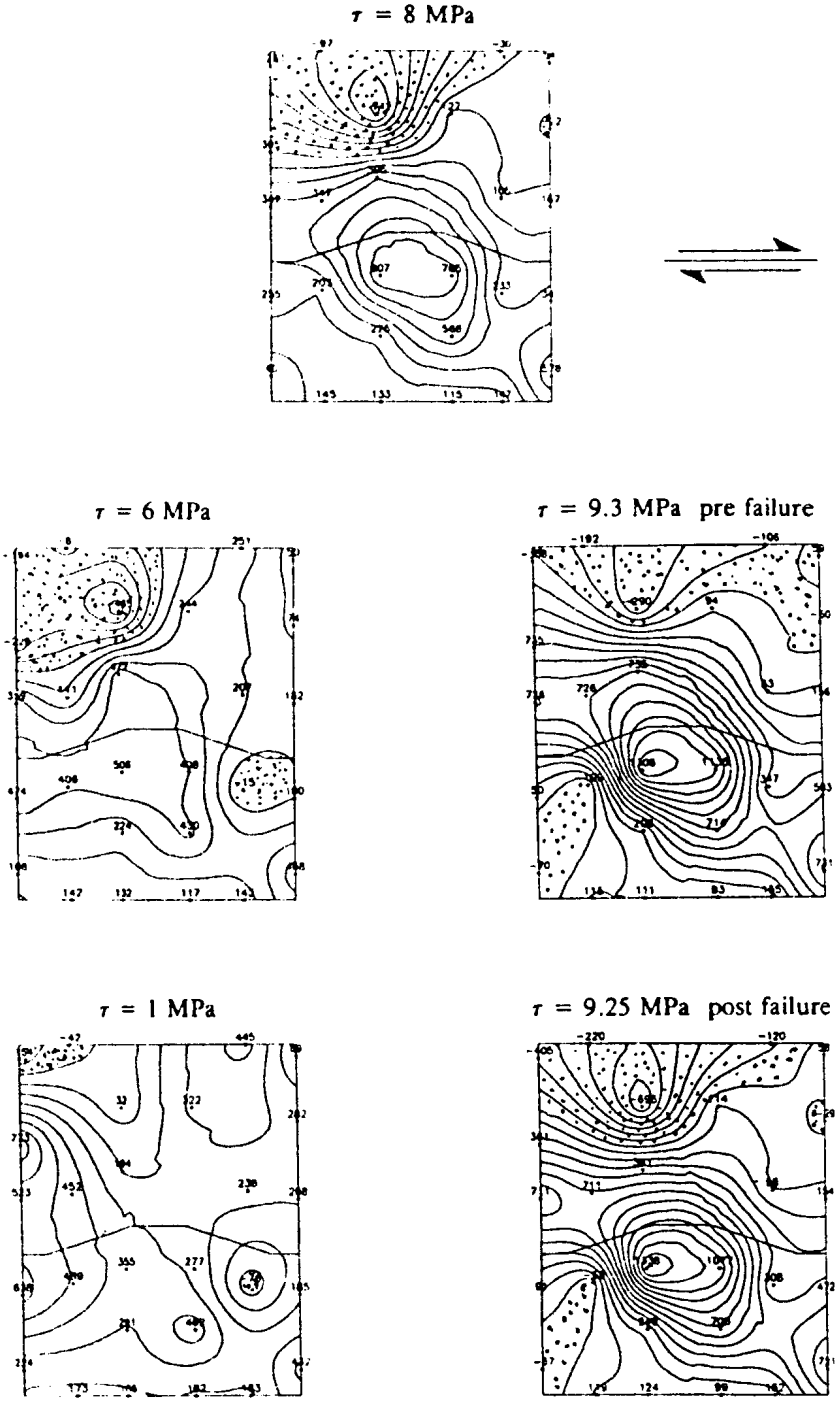

Figure 3-11 (b). Contours of horizontally oriented strain recorded during the shear portion of the third and final shear loading cycle. The loading path is clockwise, the contour interval is 100 $\mu\epsilon$ and the shear sense is as indicated. Stipples indicate tensile strains and the size of the strain field is 99 mm horizontal by 122 mm vertical.

with the maximum vertical strain moving from above to below the restraining bend. This change most likely coincided with the onset of definite shear displacement at τ = 7.0 MPa (Figure 3-8) and once again indicates a local rotation of the ϵ_1 direction towards the horizontal as shear displacement began to occur. Horizontal strain plots do not show such a reversal in trend and instead show the initiation and growth of a large compressive zone at and below the restraining bend and a large tensile zone above the asperity at the top of the strain field. At an incipient failure load of τ = 9.3 MPa, the maximum compressive strains occurred immediately below the restraining bend and correspond to vertical and horizontal stresses of approximately 69 and 67 MPa. After macroscopic shear failure, there was a 30% reduction in vertical compressive strain below the restraining bend and a 140% increase in tensile strain above the asperity step. These changes suggest the formation of secondary fractures during failure and, in fact, they do correspond to secondary fracture locations as discussed in the next section. Figure 3-12 presents a schematic diagram of the interpreted sample behaviour during the second and third shear cycles. This schematic shows that increasing shear displacement results in increased compressive stresses along the face of the restraining bend and increased tensile stresses at the base of the restraining bend and at the top of the releasing bend.

3.4 Post Mortem Sectioning

After macroscopic asperity failure at the peak of the third shear loading cycle, the shear stress applied to the fracture was gradually decreased until shear displacement stopped at a residual shear strength of 8.56 MPa. The fracture was dried and

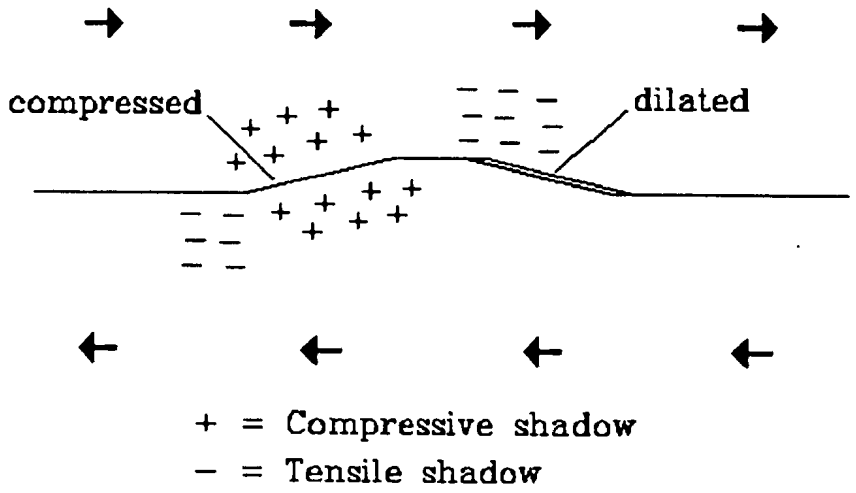

Figure 3-12. A schematic diagram proposing the basic fracture behaviour which resulted in the characteristic strain patterns observed during the second and third shear cycles.

impregnated with a dyed low viscosity resin following the procedures outlined in Gale et al. (1990). Unfortunately, while the resin bonded the sample together, a poor packer seal resulted in an incomplete impregnation which became evident after the slab of sample containing the fracture was removed from the sample box using a diamond saw. Fresh resin (dyed a different colour than the first resin to differentiate them) was allowed to flow into unimpregnated fractures exposed on the upper surface of the slab. After curing the slab was sectioned using a diamond saw along four profile planes equally spaced along its width. Visual inspection indicated that most of the secondary fractures visible in the sections were impregnated during the first impregnation and that only the ends of these fractures furthest from the simulated fracture were impregnated during the second attempt.

Figure 3-13 presents sketches of these four profile sections through the sample. Although there is variation in the fracture patterns observed in each profile, there is an overwhelming consistency of secondary fracture positions, orientation and mode across the width of the sample. There is an apparent conjugate set of shear fractures formed at the face of the restraining bend with one or both members of the conjugate set appearing in each profile. A single concave upwards shear fracture beginning at the top of the restraining bend and propagating across the asperity is also prominent in each profile. Crushed or brecciated zones were found at the base and along the face of the restraining bend as well as bounding many of the shear fractures. In several profiles, a long shear fracture is observed which begins in the upper left hand corner of the sketch but does not extend all the way to the face of the restraining bend. This fracture may be another member of the conjugate set formed at the face of the restraining bend or may be from a second adjacent conjugate set. Finally, vertically oriented tensile fractures at the base and top of the restraining bend are found in all profiles and inclined tensile fractures in the tensile shadow above the releasing bend are found in two profiles.

These results are in general agreement with the internal strain patterns which where observed from the strain gauge data. Conjugate shears, crushing and brecciation are observed in regions where high compressive strains were measured and tensile fractures were formed where large tensile strains were measured. Comparison with Figure 2-13 indicates that the observed secondary fracture patterns are very similar to those which were predicted from the results of the numerical modelling.

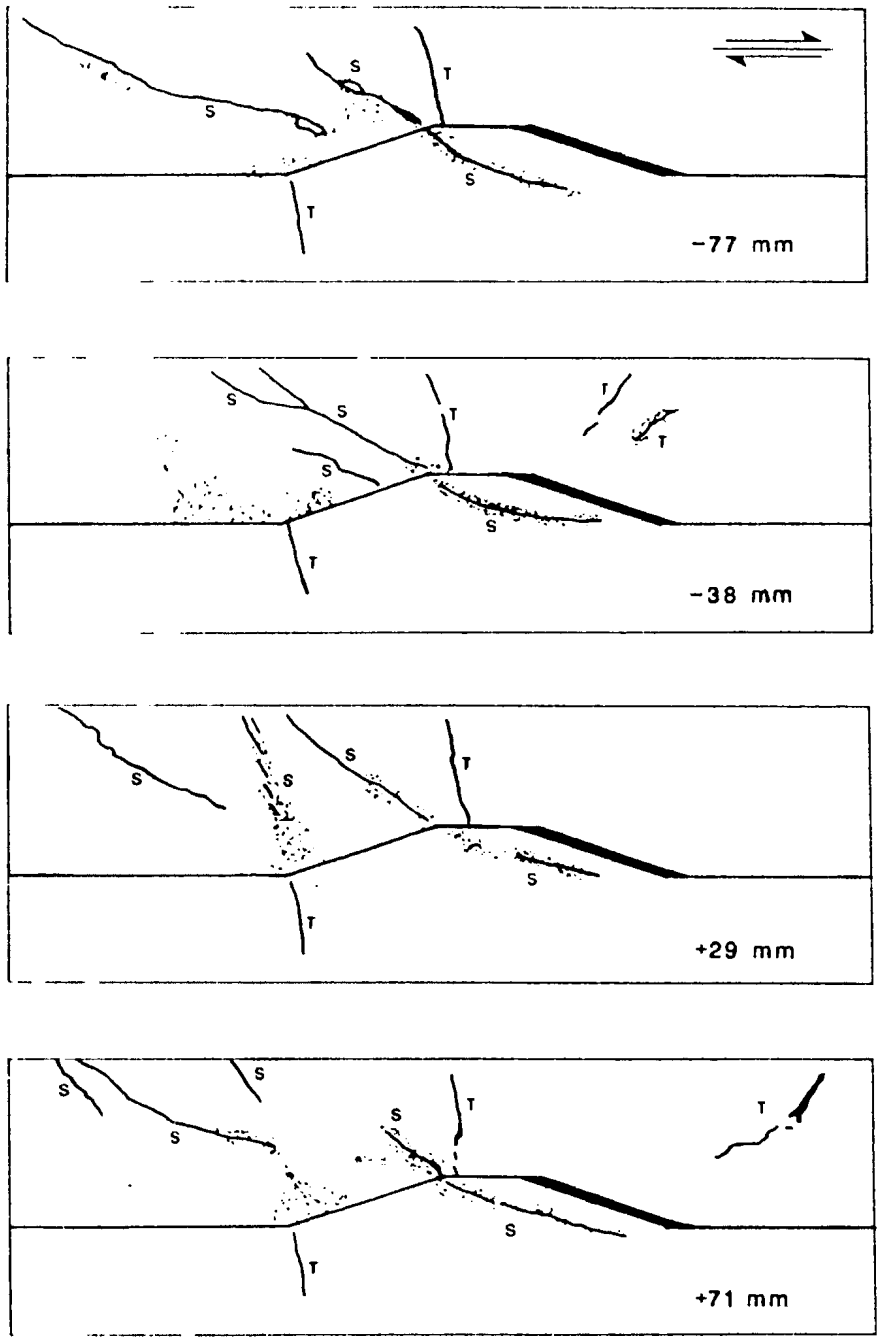

Figure 3-13. Sketches of profile sections through the resin impregnated sample after macroscopic shear failure. Discrete fractures are indicated by solid lines and crushed or brecciated zones are indicated by stippling. The mode of each secondary fracture is given as S for shear and T for tensile and the measurement indicated in the lower right hand corner of each sketch is the distance of the profile from the sample center line. The shear sense is as indicated in the upper profile.

Chapter 4 - Discussion, Conclusions and Recommendations

The numerical and physical modelling results in this investigation are discussed and analyzed. Results of the physical experiment are compared to predictions made from numerical modelling and discrepancies are identified and discussed. Finally, conclusions are made regrading the influence of large scale fracture roughness on the topics examined in this investigation and recommendations for future work are made.

4.1 Discussion of Results

Throughout this investigation, care was taken to ensure that all numerical and physical results would be applicable to natural geological conditions. This was the major reason behind the selection of high strength concrete as a rock analogue for the physical model. However, all results pertain to the scale which was tested in the laboratory and numerically simulated. Standard scaling techniques are available which can be used, with limitations, to scale the results presented in this investigation to scales which would be encountered in the field. This will not be done in this thesis, but the reader is referred to Hubbert (1937, 1951) for the theory and procedures involved.

Modelling results for normal loading indicate that the uniformity of the fracture mating about the asperity significantly influences the stress state in adjacent wall rock. If mating about the asperity is uniform then the internal stress field is symmetrical about the asperity and stress concentrations are minimal, as shown by numerical modelling.

Numerical results suggest, in fact, that as a fracture stiffens from repeated normal closure cycles, stress concentrations are reduced. Physical modelling, however, showed that stress fields can be highly asymmetric and both compressive and tensile stress zones can develop on opposite sides of the asperity. Since most natural fractures would be expected to have wide variations in fracture mating, either due to inherent variations during formation or subsequent differential weathering, natural asperities would likely cause an adjacent pattern of alternating compressive and tensile stress zones. This is in agreement with the photoelastic study of Hyett and Hudson (1990) discussed in Section 1-3. Since the tensile strength of most rocks is relatively low, moderate amounts of applied fracture normal load can result in large enough tensile stress concentrations to cause secondary tensile fracturing. This was suggested from internal strain measurements and AE data recorded during the first normal loading cycle.

Under shear loading, compressive stress concentrations are observed at the faces of asperity restraining bends and tensile stress concentrations are observed at the base of restraining bends and at the top of releasing bends. These patterns of stress concentration are consistent between numerical and physical modelling, so much so, that patterns and modes of secondary fractures predicted from numerical results are very similar to those that were observed. Compressive normal stresses measured at restraining bends can be 10 times the stresses applied to the mean fracture plane, as observed during the final two shear loading cycles. Macroscopic asperity failure is not coincident with frictional shear failure of the fracture surface but occurs after shear

displacement concentrates significant compressive stresses onto the face of the restraining bend to fracture adjacent wall rock and bypass the asperity. The observed formation of shear fractures at the face of the restraining bend is consistent with the experimental results of Aydan et. al. (1990) and Handanyan et. al. (1990) while the formation of tensile fractures at the base of restraining bends is consistent with the observations of Fishman (1990) as discussed in Section 1-3.

Observed transitions of mobilized shear strength are in general agreement with the conceptual model behind the Barton-Bandis failure criterion, as described above. However, results from both the second and third shear loading cycles indicate that the measured residual friction angle (computed from the applied fracture stresses at the onset of shear slip) was 4° less (25° as opposed to 29°) than that predicted by the Barton-Bandis index tests (Section 2-4). Perhaps there were slight variations in the concrete batches used to cast the index test sample block and the physical model or perhaps the presence of water on the fracture plane (from the permeability tests done in conjunction with this investigation) reduced the frictional properties of the concrete. Further experimentation along these lines of reasoning is required.

Finally, acoustic emission monitoring throughout this investigation has shown that macroscopic failure is almost always preceded by elevated levels of AE activity. As concluded earlier, these elevated AE levels are likely due to formation of brittle microcracks which eventually coalesce to form macroscopic fractures (Jaeger and Cook, 1976). Physical modelling results indicate that the formation of both compressive shear

and tensile fractures are preceded by recognizable AE signatures. This is consistent with the results of other workers in this field (Hardy, 1975), and suggests that AE monitoring can detect incipient failure of large stressed fractures, as are often encountered in mining and tunneling operations, and improve safety.

4.2 - Comparison of Physical Measurements to Numerical Predictions

Numerical modelling was partially successful in predicting the internal stress fields measured during the physical experiment. Numerical predictions for the shear loading cycles were more accurate than for the normal loading cycles. Several potential sources of error can be proposed. The first of these, is the plane strain formulation used by the numerical code to model stresses in the intact concrete. Lateral deformation of the concrete sample (that is, deformation perpendicular to the fracture profile) is constrained by the epoxy concrete and the steel sample box except for the region of the model adjacent to the fracture. Non-plane strain behaviour may occur in these regions and influence measured deformation. However, the major discrepancies noted between the predicted and the measured internal stress fields were associated with overall stress patterns not errors in magnitude and scaling which would have been produced by non plane strain behaviour. For example, the numerically modelled normal loading cycles predicted symmetrical stress fields surrounding the asperity, which was clearly not observed from the measured internal strain fields. Non-plane strain behaviour would have only changed the scale and magnitudes of observed strains, not produced the highly

asymmetrical strain patterns observed. Thus, although non-plane strain behaviour may have occurred in the sample, other factors are probably more significant.

A second source of error is the fact that the numerical model uses an elastic formulation for intact rock, whereas experimental results indicate that there was plastic strain within the concrete during each loading cycle. Thus, errors in assigning stresses to measured strains would certainly occur, with calculated stresses overestimating the true internal stresses. Experimental results, however, show that the extent of permanent set decreases with each new loading cycle, so errors associated with this problem would become less significant during successive loading cycles. As well, errors in stress estimation would be more significant during the unloading portion of a loading cycle, so comparisons between numerical and experimental results would be more valid if limited to the upward portion of the loading cycle.

A third source of error, continuing the line of reasoning above, deals with the influence of secondary fracturing within the concrete sample. Experimental measurements taken before and after macroscopic failure indicate that significant internal strain changes accompany the formation of secondary fractures. The numerical model assumes an elastic behaviour of the intact rock and could not model the formation and effects of secondary fracturing. AE data and internal strain measurements suggest that secondary tensile fracturing may have occurred prior to macroscopic sample failure. This certainly would have influenced all subsequent measurements and may be an important source of error in some numerical predictions.

A final source of error, as discussed in the previous section, is the uniformity of fracture mating about the asperity. Numerical modelling assumed that fracture mating was uniform at the beginning of each loading cycle, which was clearly not the case observed during most of the experimental testing. Unexpected behaviour induced by this condition influenced the internal strains measured during the physical experiment. Numerous examples of this can be identified in the experimental data set. For example, numerical modelling indicated that stress patterns during normal loading should be symmetrical about the asperity. As proposed in Figure 3-7, non uniform mating of the fracture on the right hand asperity bend induced tensile strains below that side of the asperity and resulted in an asymmetrical stress pattern. Stress concentrations resulting from this strain asymmetry induced compressive stresses which were four times larger than those predicted by the modelling and may have even induced secondary tensile fracturing in adjacent regions. Secondly, during the first shear cycle a large portion of the applied shear energy was used to overcome friction and slip the fracture 200 μm to bring the faces of the restraining bend into contact. In this situation, the numerical modelling would have difficulty predicting the measured strain field since the modelling assumed that the fracture was in contact at the restraining bend at the start of shear loading and an inherently different stress/deformation path (i.e. without the stress changes associated with shear slip) would have been predicted. Finally, the strain field measured during the third shear cycle was influenced by permanent fracture displacement which was produced during the second shear cycle. Clearly, non uniform fracture

mating appears to be a significant source of error in the numerical predictions made in this study.

When the initial fracture mating and secondary fracture conditions are assumed correctly, however, the predictions of the numerical model were improved. This was evident from the predicted stress patterns for the second shear loading cycle, which were similar to those that were measured. This was probably because the slip induced at the peak of the first shear cycle brought the restraining bend faces into tight contact (which was the underlying assumption during all predictive modelling) and any non uniform fracture mating at the releasing bend would have minimal effect since that bend would be dilated. At peak shear stress, the geometry of the vertical and horizontal stress fields numerically predicted (Figure A-4) are similar to the measured strain fields (Figure 3-10) which have been placed side by side for comparison in Figure 4-1. Examination of Figure 4-1 in greater detail, however, indicates that the geometric agreement is better for the compressive stress/strain zones than for the tensile zones. For example, the size of the tensile zone in the vertical strain field (Figure 4-1b) is much larger than numerically predicted and, as a second example, the horizontal strain field (Figure 4-2a) shows a tensile zone at the upper left of the restraining bend which was not numerically predicted at all. These discrepancies reflect a fundamental shortcoming of the numerical modelling code, namely the inability to realistically model the tensile behaviour of the concrete, as was explained earlier (Section 3.2) as a rationale for not assigning tensile stress values to tensile strains. Examination of the maximum compressive strains in Figure 4-1

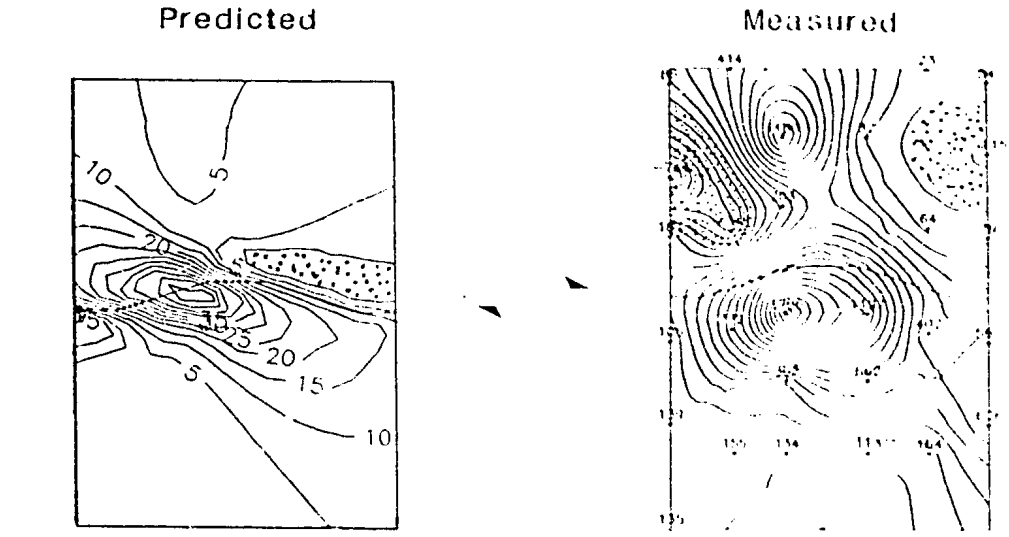

(a)

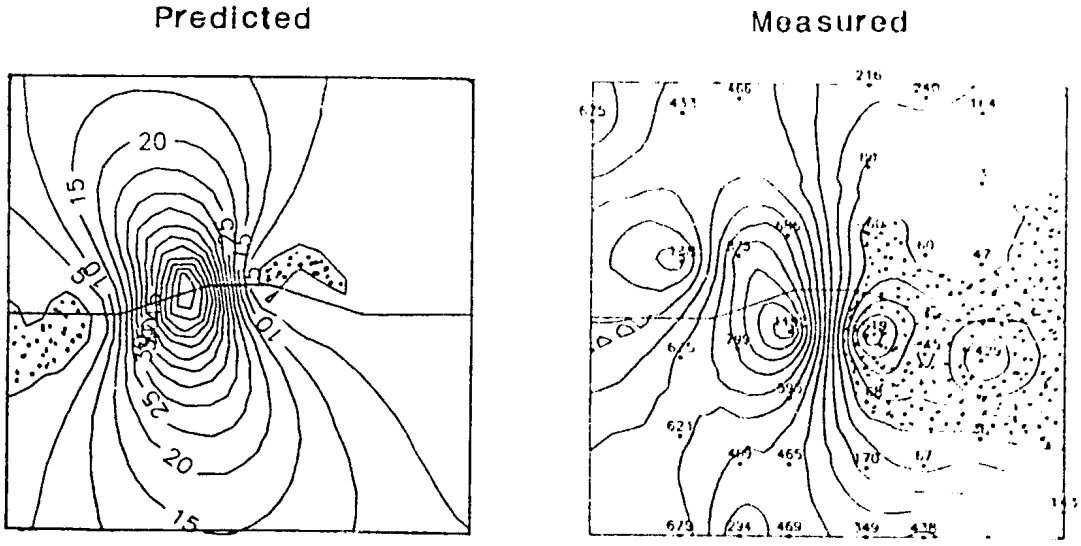

(b)

Figure 4-1. Comparison of the predicted stresses at τ = 4.60 MPa and the measured strains at τ = 7.8 MPa for the second shear loading cycle for (a) horizontal orientation and (b) vertical orientation. Note: these tests are at a constant normal stress of σ_N = 8 MPa. Stippling indicated tensile zones.

indicates approximate corresponding stresses of 60 MPa vertical and 89 MPa horizontal which compare to numerically predicted values of 74 MPa vertical and 59 MPa horizontal. The maximum vertical stress is more accurate (differing by 20% less then the predicted value) than the maximum horizontal stress (differing by 50% greater then the predicted value). In this case, the discrepancies are most likely the result of the approximations used to estimate stresses from strains and the influence of the inferred secondary fractures in the physical model at this stage of loading (Section 3.3).

Overall, comparisons between predicted numerical and measured experimental results highlight shortfalls in some of the assumptions concerning the physical condition of the fracture and the limitations within the modelling approach itself. The non linear modelling procedures used (Section 2-5) and the independent laboratory measurement of the concrete and fracture properties (Section 2-4) likely ensured the most accurate predictions available from the modelling code. The major sources of error with predictive modelling were (1) an inaccurate assumption regarding the uniformity of fracture mating about the large scale roughness asperity and (2) the inability of the modelling code to realistically simulate secondary fracturing and plastic deformation. *A priori* knowledge of the uniformity of fracture mating could overcome the first major source of error, but a significant modification of the modelling code is required to address the second major source of error.

Before this section is concluded, however, one question needs to be resolved, namely, why didn't the sample fail at the peak of the second shear loading cycle? The

obvious answer is that the sources of error, described earlier, combined to result in inaccurate stress predictions. However, the measured strain field for the second shear loading cycle was very similar to that predicted by the numerical modelling. Some other hypothesis seems necessary to explain why failure did not occur.

The prediction of failure was made by examining the magnitude of the largest major principal stress produced in the numerical model. During the numerical simulation of the second shear cycle, a maximum value of 96 MPa for major principal stress was encountered, and since it was greater than the uniaxial compressive strength of the concrete of 70 MPa, it was assumed that failure would occur. However, it would have been more appropriate to predict failure of the intact concrete using a Mohr-Coulomb failure criterion, since there is a biaxial state of stress in the concrete sample during loading. This was done in Figure 4-2, which assumes an internal angle of friction of 30°. In this diagram, it is clear that at 96 MPa compressive stress the minor principal normal stress (which was determined by going back to the original modelling output data) is not small enough to alow the Mohr failure circle to become tangent to the failure curve. Had the prediction for sample failure been done using this procedure, a more accurate prediction would have been made.

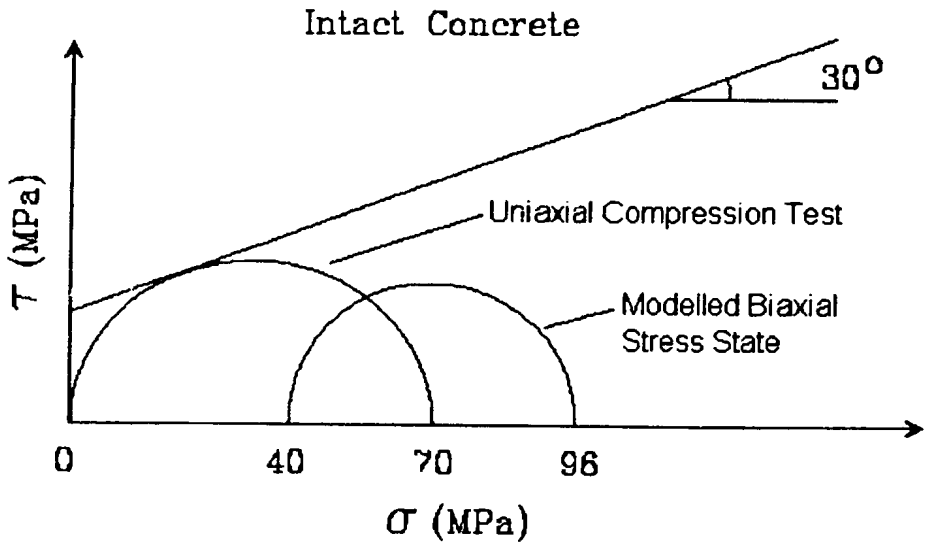

Figure 4-2. Mohr-Coulomb failure diagram explaining why the model did not macroscopically fail as anticipated, even though both predicted and measured maximum compressive stresses exceeded the uniaxial compressive strength of the concrete.

4.3 - Conclusions

As was predicted by numerical modelling in Chapter 2 and measured in a controlled physical experiment in Chapter 3, large scale fracture roughness has significant influence on normal and shear fracture stiffnesses, on the stress state in adjacent wall rock and on the modes and patterns of induced secondary fractures. These factors ultimately increase the total volume of available fracture porosity in the vicinity of the large scale roughness feature by the normal or lateral dilation of the fracture, or by the creation of induced secondary fractures.

Since the data set collected and analyzed during this study was large and comprehensive, numerous conclusions can be drawn. These include:

(1) Under normal loading, large scale fracture roughness enables lateral stresses to be applied to adjacent wall rock even though no shear loads are applied parallel to the mean fracture plane, as is evident from analysis of the internal horizontal strain fields observed from all three normal loading cycles. If no lateral stresses were applied, the horizontal strain fields would be uniform, but the pronounced heterogeneity and asymmetry observed indicates significant resolution of lateral stresses in the adjacent wall rock. If large enough, stress concentrations associated with these lateral stresses can induce secondary tensile fracturing.

(2) Under shear loading there are significant stress concentrations associated with restraining and releasing bends which can easily induce both shear and tensile fracturing and brecciation in adjacent wall rock. Restraining bends serve as pinning points on a

fracture surface, inhibiting uniform fracture slip and acting as zones of stress accumulation.

(3) Induced secondary fractures in adjacent wall rock do not occur when friction is overcome and the fracture begins to slip but does occur when pinning of the fracture at a restraining bend induces stress concentrations in the adjacent wall rock. Thus failure in the adjacent wall rock is not coincident with the frictional shear failure of the fracture.

(4) Induced tensile fracturing occurs when any of the three principal stresses exceeds the tensile strength of the rock, which is typically 5% to 10% of its uniaxial compressive strength. Induced shear fractures, on the other hand, occur only after the major and minor principal stresses meet the Mohr-Coulomb failure criterion. As such, induced secondary tensile fractures can occur at much lower levels of applied fracture stresses and should be more common then secondary shear fractures.

(5) Episodes of shear displacement and fracture shear strength recorded during shear loading are in general agreement with the conceptual model behind the Barton-Bandis shear strength criterion.

(6) Formation of macroscopic shear and tensile fractures is generally preceded by levels of sustained acoustic emission activity.

(7) Enhanced fracture porosity in the vicinity of large scale roughness features can take three different forms. These include normally dilated fractured porosity associated with climbing of restraining bends, laterally dilated fracture porosity at releasing bends, and the porosity of induced secondary fractures in adjacent wall rock.

(8) From a mining or construction perspective, regions of large scale fracture roughness identified along a fracture trace can cause potential excavation or tunnelling problems because of locally heterogeneous stress fields, high stress concentrations and excessive secondary fracturing.

(9) From an exploration point of view, large scale roughness features identified along a fracture trace are likely candidates for enhanced fracture porosity and potential sites of accumulation of fracture transported fluids.

4.4 - Recommendations for Future Work

Future research in this area can examine numerous related topics or can focus on shortfalls and limitations highlighted by this study. For example:

(1) Investigation of the state of stress and deformation associated with other varieties of large scale roughness. Models can be tested which examine the effects of asperity size, shape, numbers and three dimensional arrangement. Models incorporating some form of anisotropy such as simulated bedding or cleavage planes can also be tested. The mechanical interaction between multiple asperities can be used to investigate such topics as incremental shear strain.

(2) The numerical modelling code can be modified to accommodate additional types of deformation, such as plastic strain, brittle fracturing, plane stress or even a three dimensional formulation. Procedures can be developed to predict the uniformity of fracture mating before an experiment. Ultimately, a full three dimensional numerical and

physical characterization of the influence of large scale fracture roughness on local stress fields and secondary fracturing patterns can be realized.

Bibliography

Aydan, O., S. Ebisu, S. Komura and A. Watanabe (1990), Studies on interfaces and discontinuities and an incremental elasto-plastic constitutive law in: Rock Joints, ISRM Symposium, Barton and Stephansson (eds), Balkema, Norway, pp 595-602, 1990.

Atkinson, L. C. (1987), A Laboratory and Numerical Investigation of Fracture Flow into a Horizontal Wellbore, PhD Dissertation, Memorial University of Newfoundland.

Barton, N., S. Bandis and K. Bakhtar (1985), Strength, Deformation and Conductivity Coupling of Rock Joints, International Journal of Rock Mechanics and Mining Sciences & Geomechanical Abstracts, Vol. 22, No. 3, pp 121-140, 1985.

Beer, F.P. and E.R. Johnson Jr. (1981), Mechanics of Materials, McGraw-Hill Ryerson Limited, Toronto, 1981.

Berwanger, C. (1968), An Evaluation of Electrical Resistance Strain Gauges for Use On Concrete Surfaces, National Research Council of Canada, Division of Building Research, Technical Paper No. 285, Ottawa, 1968.

Brace, W.F and J.D. Byerlee (1966), Stick slip as a mechanism for earthquakes, Science, Vol 153, pp 990-992, 1966.

Byerlee, J. D. (1978), Friction of rocks, Pure and Applied Geophysics, Vol. 116, pp 615-626, 1978.

Canadian Portland Cement Association (1991), Design of High Strength Concrete Handbook, CPCA, Toronto, 1991.

Deng, Q, D. Wu, P. Zhang and S. Chen (1986), Structure and Deformational Character of Strike-Slip Fault Zones, Pure and Applied Geophysics, Vol. 124, Nos. 1/2, pp 203-233, 1986.

Erickson, S. G. and D. V. Wiltschko (1991), Spatially Heterogeneous Strength in Thrust Fault Zones, Journal of Geophysical Research, Vol. 96, No. B5, pp 8427-8439, May, 1991.

Fishman, Yu. A. (1990), Failure mechanism and shear strength of joint wall asperities in: Rock Joints, ISRM Symposium, Barton and Stephansson (eds), Balkema, Norway, pp 627-631, 1990.

Gale, J. E. (1975), A numerical, field and laboratory study of flow in rocks with deformable fractures, PhD dissertation, University of California, Berkeley.

Gale, J. E., P. Lemessurier, R. MacLeod and A. Pye (1990), The coupled stress-flow-thermal behaviour of natural rock joints, unpublished report, Department of Earth Sciences, Memorial University of Newfoundland, January, 1990.

Gale, J. E., R. MacLeod, M. Gutierrez, L. Dacker and A. Makurat (1993), Integration and analysis of coupled stress-flow laboratory tests data on natural fractures - MUN and NGI tests, unpublished consultants report, Fracflow Consultants Inc., St. John's, Canada and Norwegian Geotechnical Institute, Olso, Norway, June, 1993.

Gammond, J. F. (1987), Bridge structures as sense of displacement criteria in brittle fault zones, Journal of Structural Geology, Vol. 9, No. 5/6, pp 609-620, 1987.

Goodman, R.E. (1976), Methods of geological engineering in discontinuous rocks, West St. Paul, Minnesota, 1976.

Goodman, R. E. (1989), Introduction to rock mechanics, 2nd Ed., John Wiley & Sons, New York, 1989.

Goodman, R.E., R.E.Taylor and T. Brekke, (1968), A model for the mechanics of jointed rock, Journal of Soil Mechanics and Foundation Division, ASCE, Vol. 94, No. SM3, 1968.

Groshong, R.H. (1988), Low Temperature deformation mechanisms and their interpretation, Geological Society of American Bulletin, Vol. 100, pp 1329-1360, 1988.

Handanyan, J. M., E. R. Danek, R.A. D'Andrea and J. D. Sage (1990), The role of tension in failure of jointed rock in: Rock Joints, ISRM Symposium, Barton and Stephansson (eds), Balkema, Norway, 1990.

Hardy, H.G. (1975), Emergence of Acoustic Emissions/Microseismic Activity as a Tool in Geomechanics, Research review and introduction to Proceedings, First Conference on Acoustic Emission/Microseismic Activity in Geologic Structures and Materials, Pennsylvania State University, Pennsylvania, pp 13-32, 1975.

Hubbert, M. K. (1937), Theory of scale models as applied to the study of geological structures, Bulletin of the Geological Society of America, Vol. 48, pp 1459-1520, 1937.

Hubbert, M. K. (1951), Mechanical basis for certain familiar geological structures, Bulletin of the Geological Society of America, Vol. 62, pp 355-372, 1951.

Hyett, A. J. and J. A. Hudson (1990), A photoelastic investigation of the stress state close to rock joints, Rock Joints, ISRM Symposium, Barton and Stephansson (eds), Balkema, Norway, pp 195-202, 1990.

Jaeger, J.C and N.G.W. Cook (1976), Fundamentals of rock mechanics, Chapmand and Hall, London, 1976.

Keithley Assist (1992), ViewDAC users guide, Keithley Technology Corp., Rochester, 1992.

Kerrich, R. and I. Allison (1978), Flow mechanics in rocks: Microscopic and mesoscopic structures, and their relation to physical conditions of deformation in the crust, Geoscience Canada, Vol. 5, No. 3, pp 109-118, 1978.

Lee, Y.H., J.R. Carr, D.J. Barr and C.J. Haas (1990), The fractal dimension as a measure of the roughness of rock discontinuity profiles, International Journal of Rock Mechanics and Mining Sciences & Geomechanics, Vol. 27, No. 6, pp 453-468, 1990.

Petit, J. P. (1987), Criteria for the sense of movement on fault surfaces in brittle rocks, Journal of Structural Geology, Vol. 9, No. 5/6, pp 590-608, 1987.

Power, W. L., T. E. Tullis, S. Brown, G. N. Boitnott and C. H. Scholtz (1987), Roughness of natural fault surfaces, Geophysical Research Letters, 14: 29-32, 1987.

Price, N. G. (1966), Fault and joint development in brittle and semi-brittle rocks, Permagon Press, Oxford, 1966.

Segall, P. and D. D. Pollard (1980), Mechanics of Discontinuous Faults, Journal of Geophysical Research, Vol. 85, No. B8, pp 4337-4350, 1980.

Segall, P. and D.D. Pollard (1983), Nucleation and Growth of Strike Slip Faults in Granite, Journal of Geophysical Research, Vol. 88, No. B1, pp 555-578, 1983.

Scholtz, C. H. (1990), The Mechanics of Earthquakes and Faulting, Cambridge University Press, New York, 1990.

Sibson, R. H. (1986), Brecciation Processes in Fault Zones: Inferences from Earthquake Rupturing, Pure and Applied Geophysics, Vol. 124, Nos. 1/2, pp 159-175, 1986.

Telford, W. M., L. P. Geldart and R. E. Sheriff (1990), Applied Geophysics, Second Edition, Cambridge University Press, New York, pp 217-222, 1990.

White, S.H. and R.J. Knipe (1978), Microstructure and cleavage development in selected slates, Contributions to Mineralogy and Petrology, Vol. 66, pp 165-174, 1978.

Appendix A - Vertical and Horizontal Stress Results From Numerical Modelling of Large Scale Fracture Roughness

The following diagrams are contour plots of the vertical and horizontal stresses determined from the numerical simulation of two normal loading cycles followed by two shear loading cycles presented in Chapter 2. These are meant to compliment the mean and maximum shear stress plots presented in that chapter, and for comparison with the biaxial experimental results. Note that the loading path for each of these diagrams is clockwise beginning in the lower left hand corner of the page.

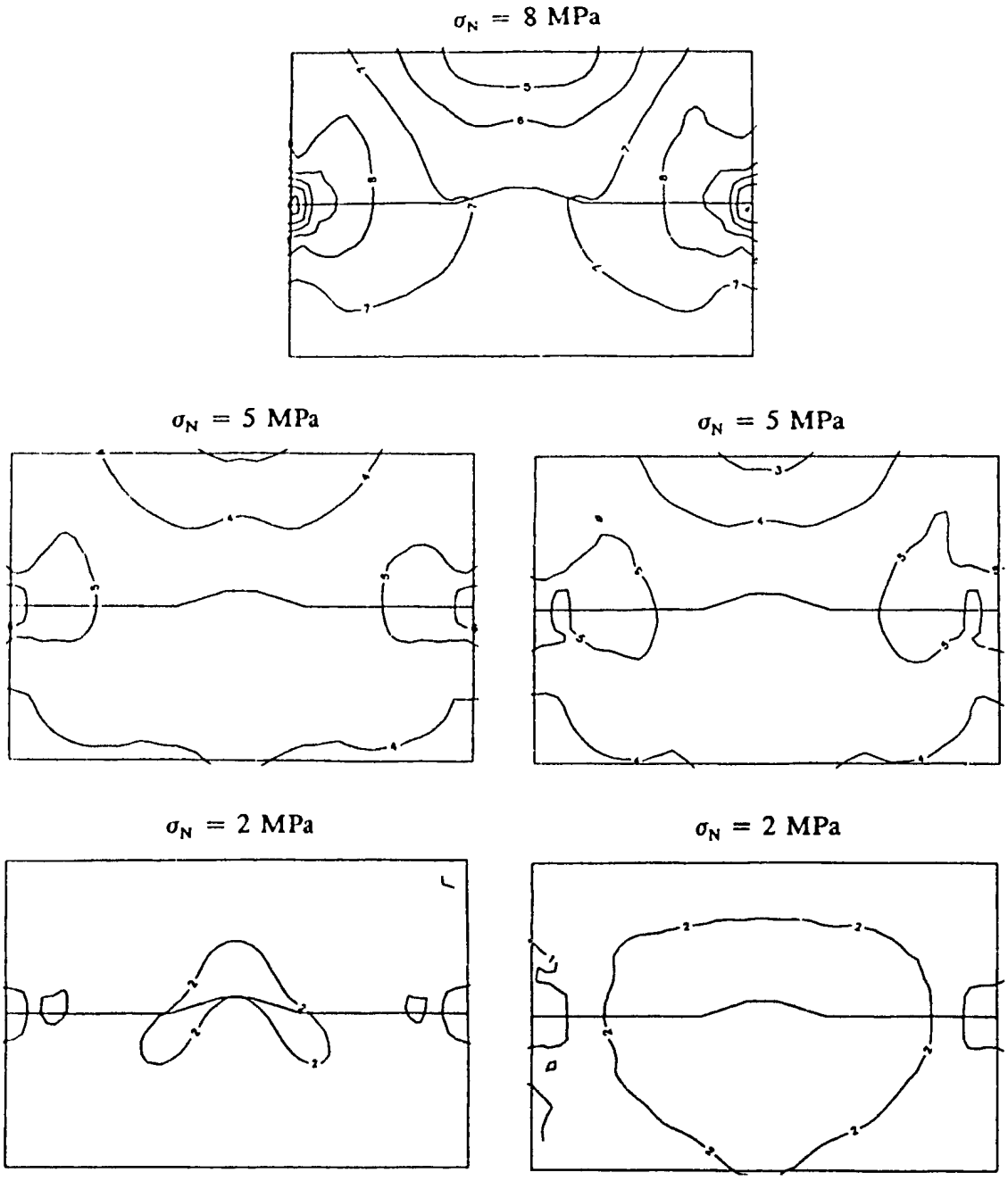

Figure A-1(a). Vertical stress contours for first modelled normal loading cycle. Compressive stresses are positive and the contour interval is 1 MPa.

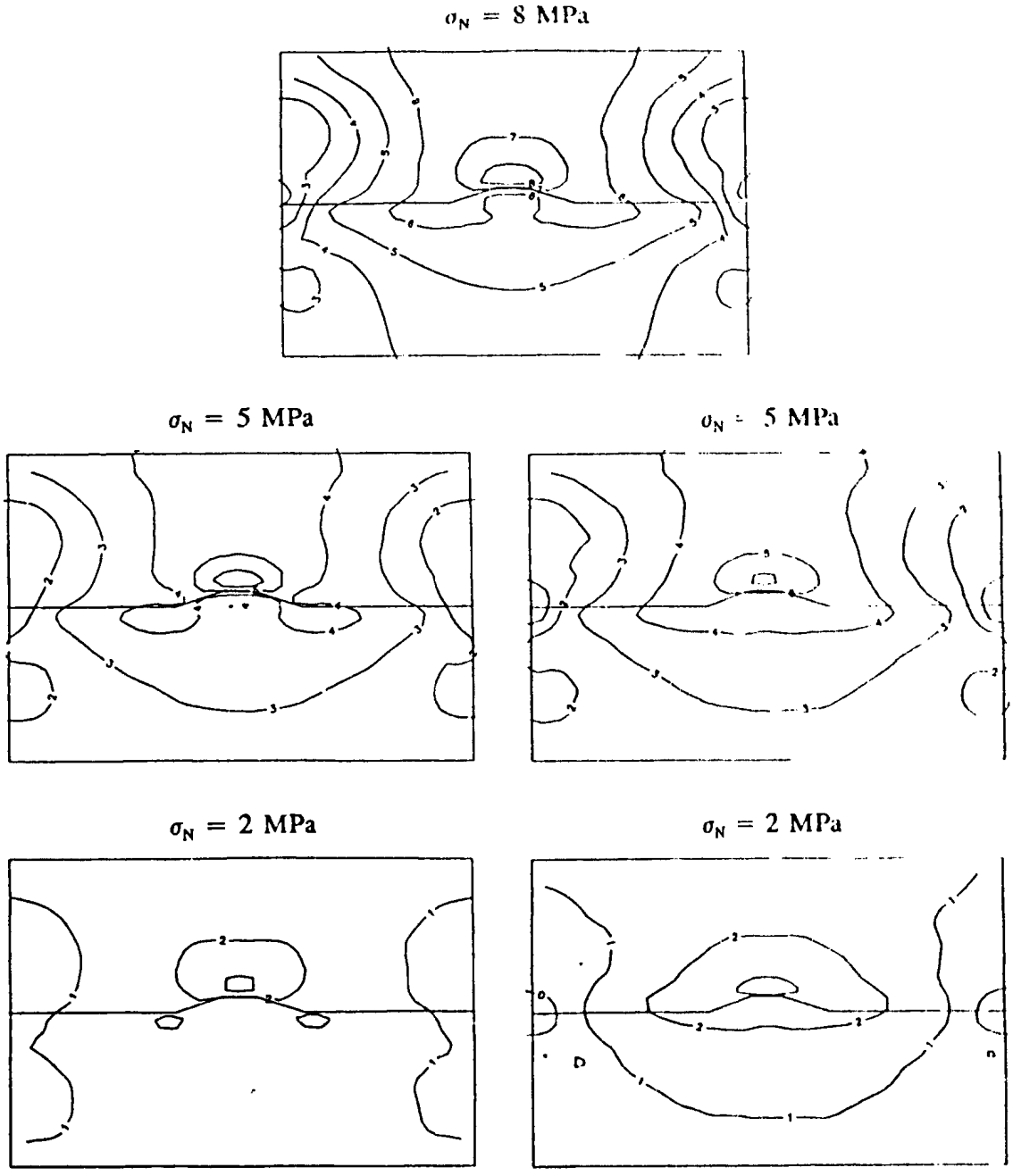

Figure A-1(b). Horizontal stress contours for first modelled normal loading cycle. Compressive stresses are positive and the contour interval is 1 MPa.

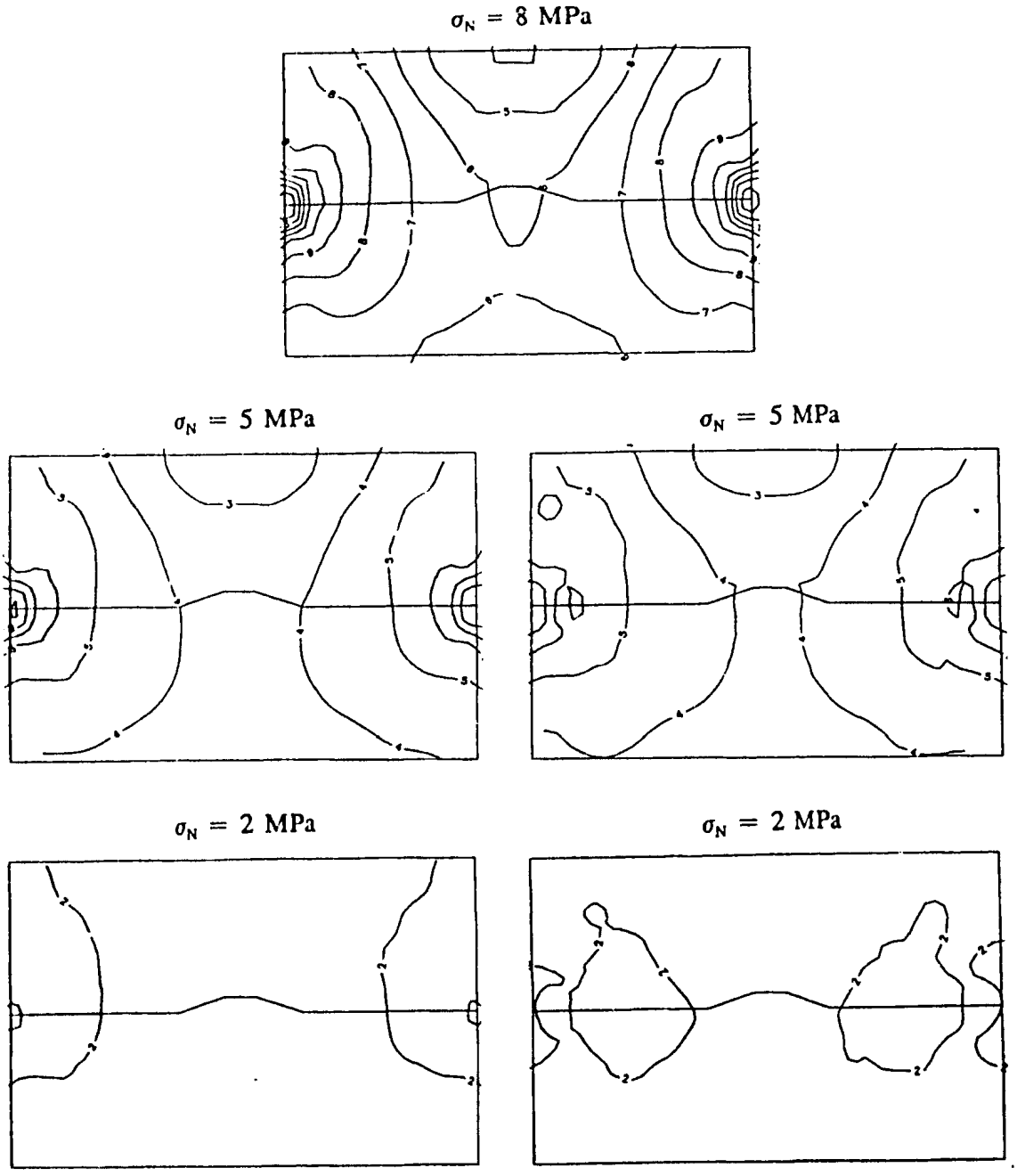

Figure A-2(a). Vertical stress contours for second modelled normal loading cycle. Compressive stresses are positive and the contour interval is 1 MPa.

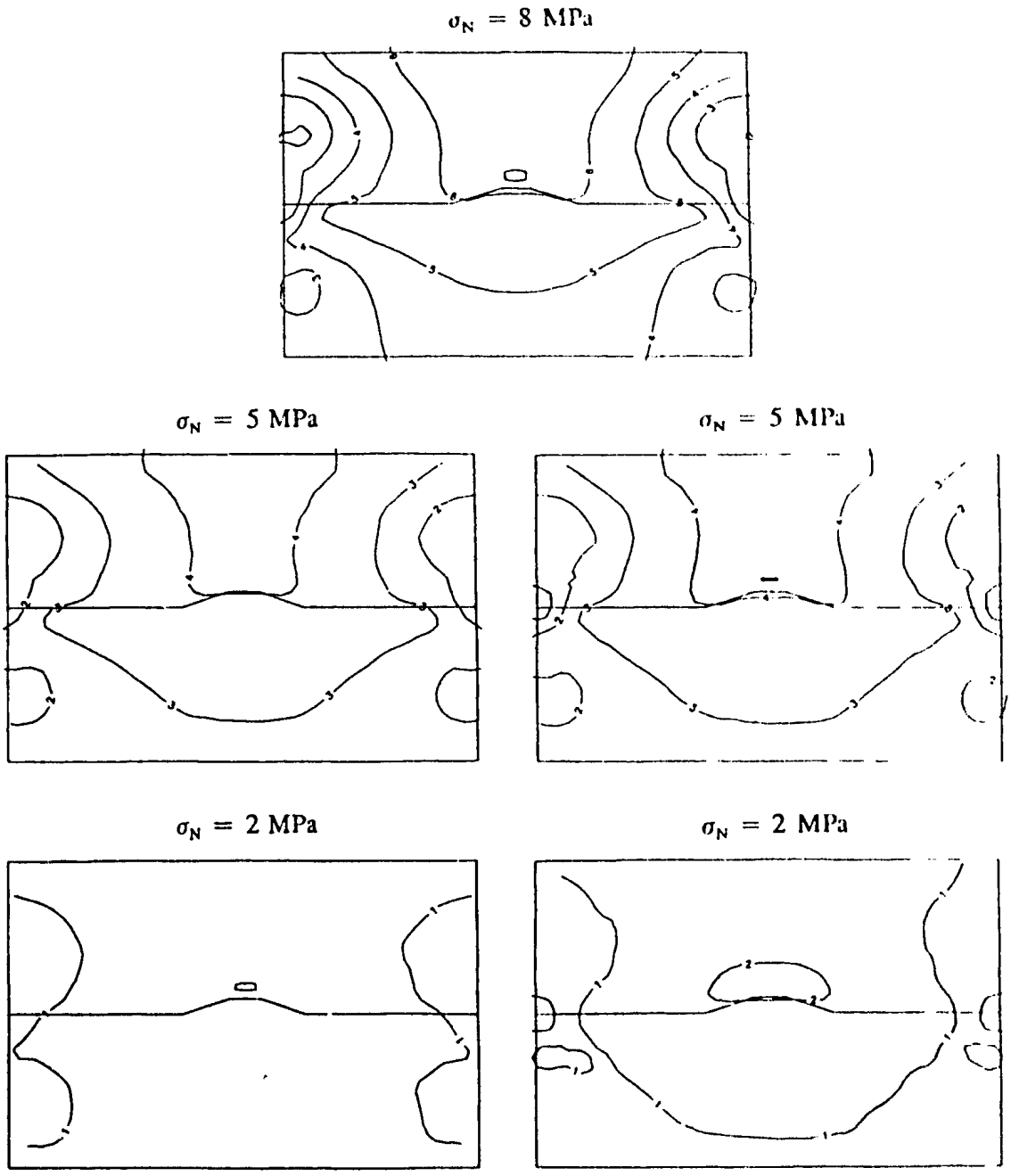

Figure A-2(b). Horizontal stress contours for second modelled normal loading cycle. Compressive stresses are positive and the contour interval is 1 MPa.

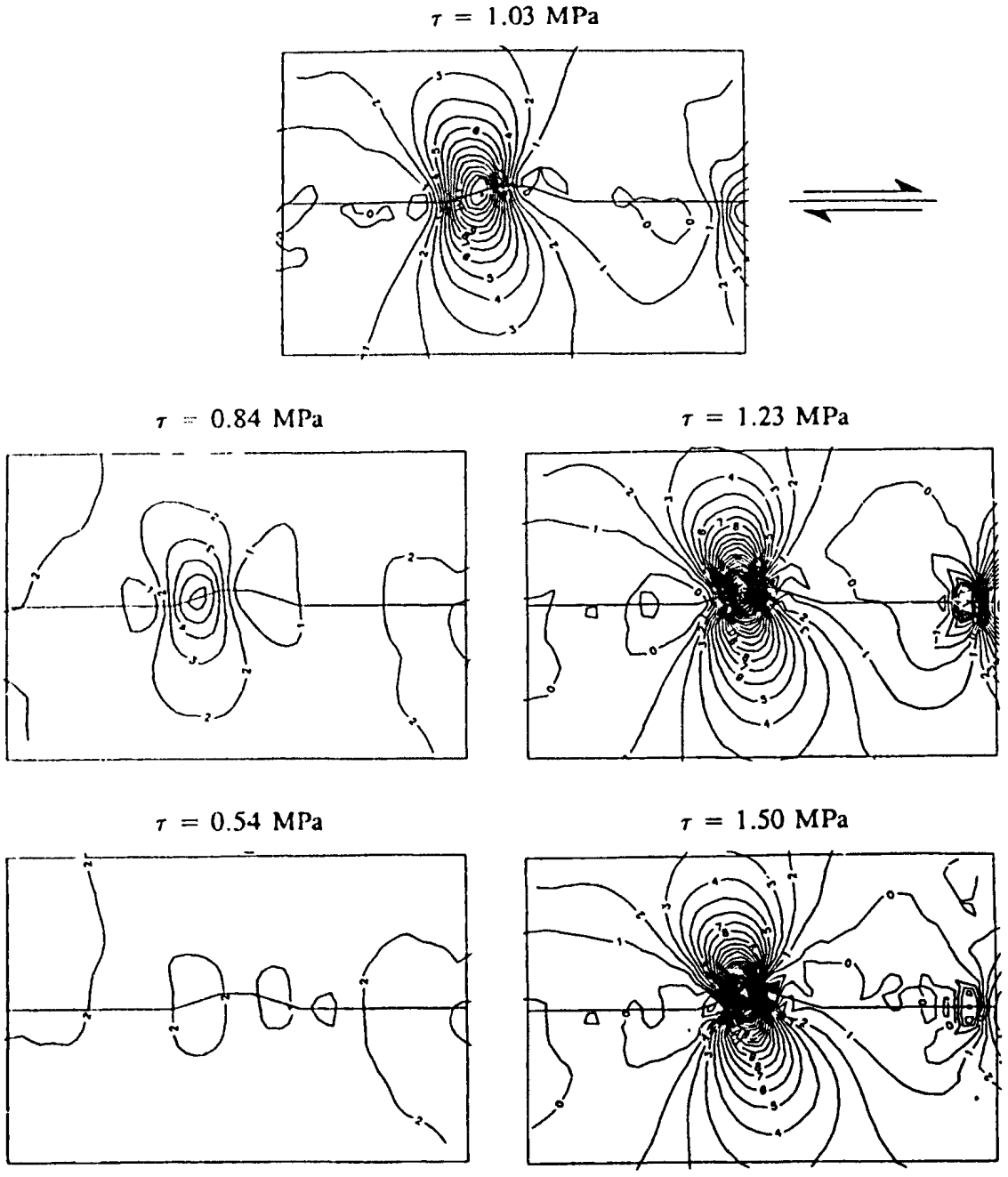

Figure A-3(a). Vertical stress contours for modelled shear loading cycle at normal stress of 2 MPa. Compressive stresses are positive and the contour interval is 1 MPa.

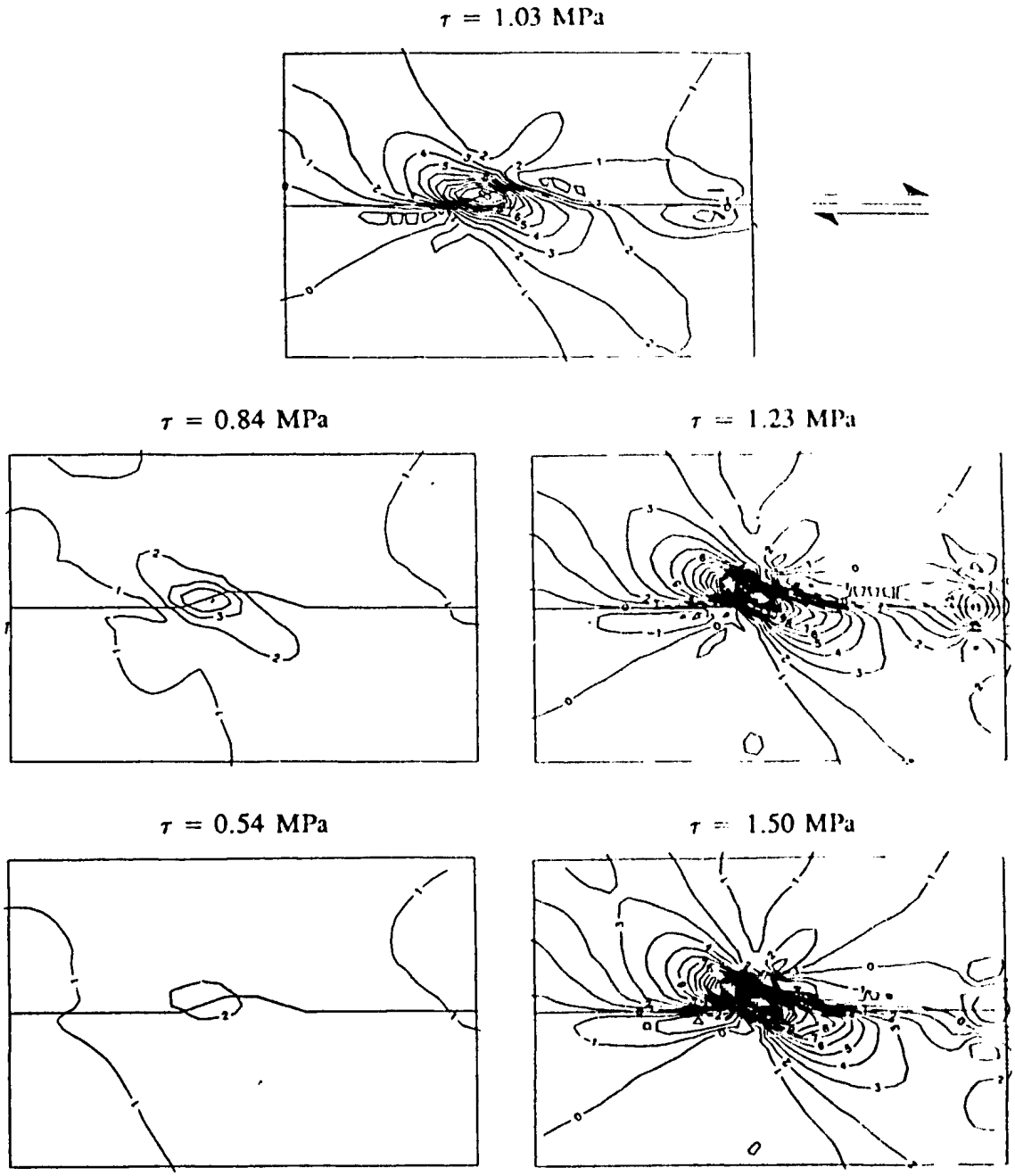

Figure A-3(b). Horizontal stress contours for modelled shear loading cycle at normal stress of 2 MPa. Compressive stresses are positive and the contour interval is 1 MPa.

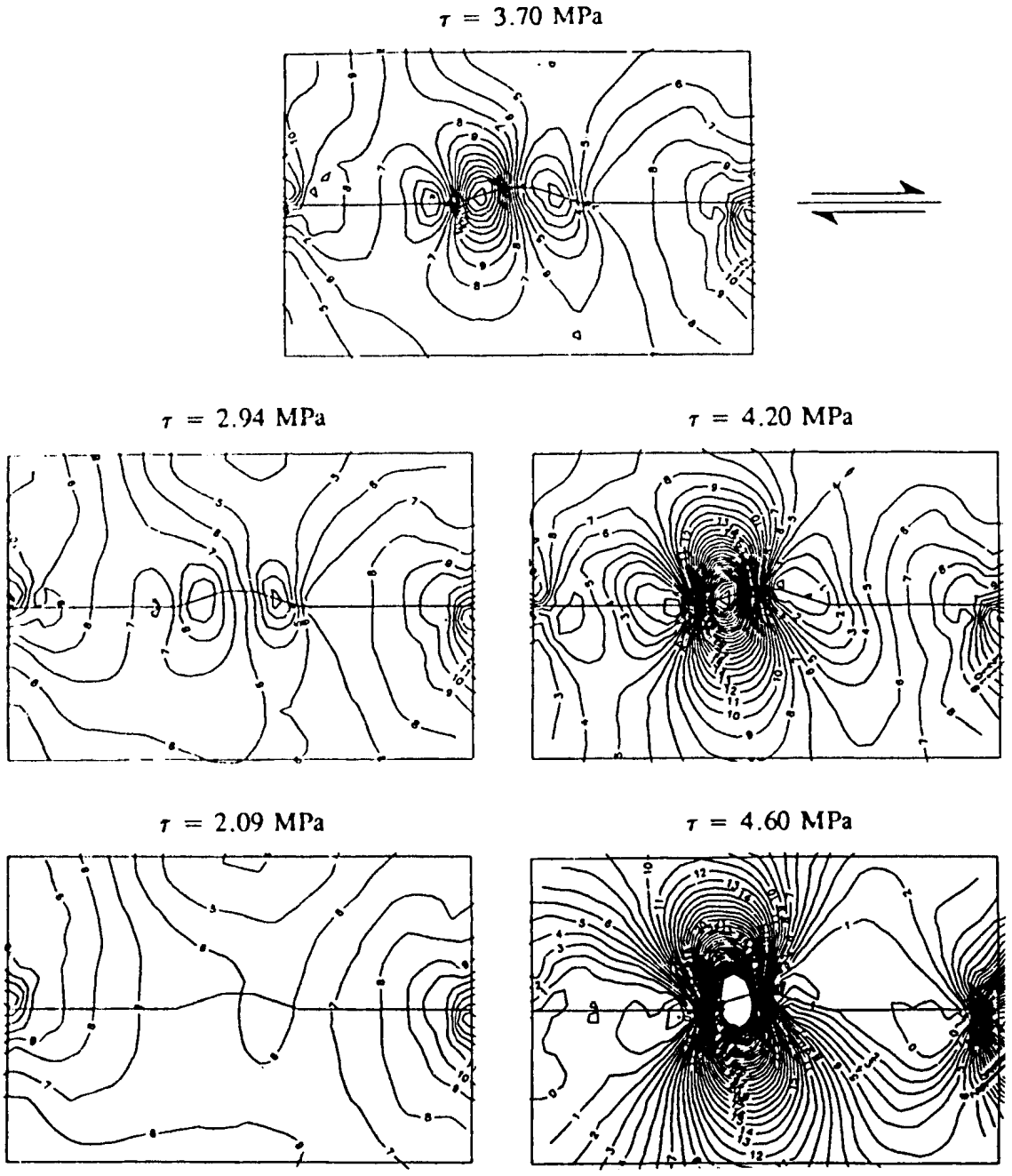

Figure A-4(a). Vertical stress contours for modelled shear loading cycle at normal stress of 8 MPa. Compressive stresses are positive and the contour interval is 1 MPa.

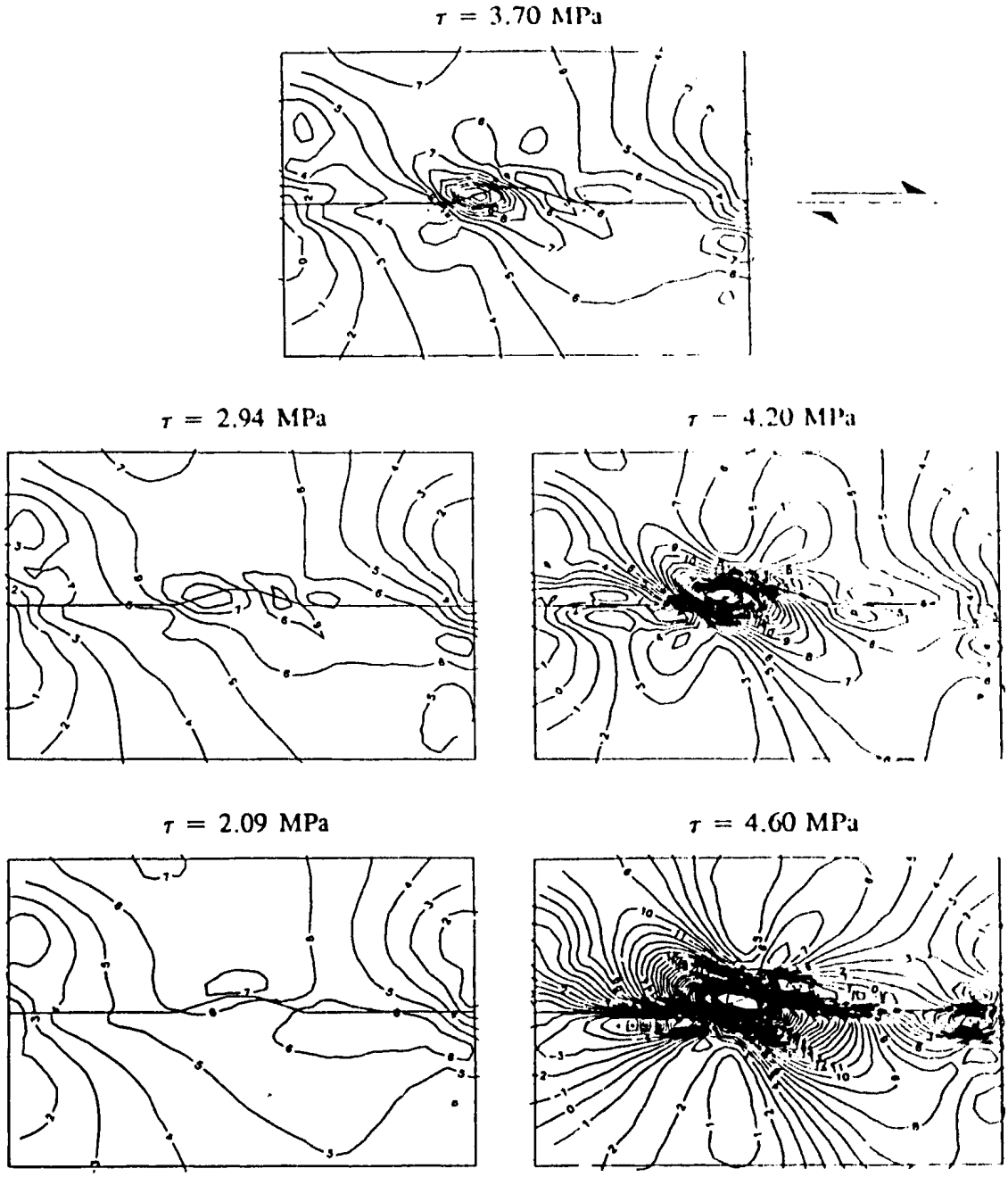

Figure A-4(b). Horizontal stress contours for modelled shear loading cycle at normal stress of 8 MPa. Compressive stresses are positive and the contour interval is 1 MPa.

Appendix B - Design, Testing and Calibration of MUGS Strain Gauge Measuring System

Although the experimental component of this investigation relied heavily on the collection of strain gauge data, the availability of strain gauge reading equipment was limited. Due to the excessive cost of commercially available systems, it was decided to develop an alternative system in house. This undertaking proved successful and resulted in a strain gauge measuring system providing good accuracy and resolution over the strain range and time intervals typical of static rock mechanics experiments.

B-1. MUGS System Design and Operation

Most commercial multiple strain gauge reading systems rely upon the unbalanced ¼ Wheatstone Bridge circuit shown in Figure B-1. The voltage change measured across both arms of the bridge is linearly proportional to the strain measured by the strain gauge. This voltage is filtered, amplified and sometimes scaled to improve the signal to noise ratio before it is relayed to a data storage device, such as a computer. As well, expensive precision resistors (typically with three required per strain gauge channel) are required to complete the bridge circuit. These factors, coupled with a limited market, make the use of strain gauges expensive, often costing hundreds of dollars per active strain gauge channel.

The strain gauge system developed in house is called the Multiple Unbridged Strain Gauge System (MUGS) and uses simplified electronics and real time microcomputer based software analysis to bypass the expensive aspects of commercial

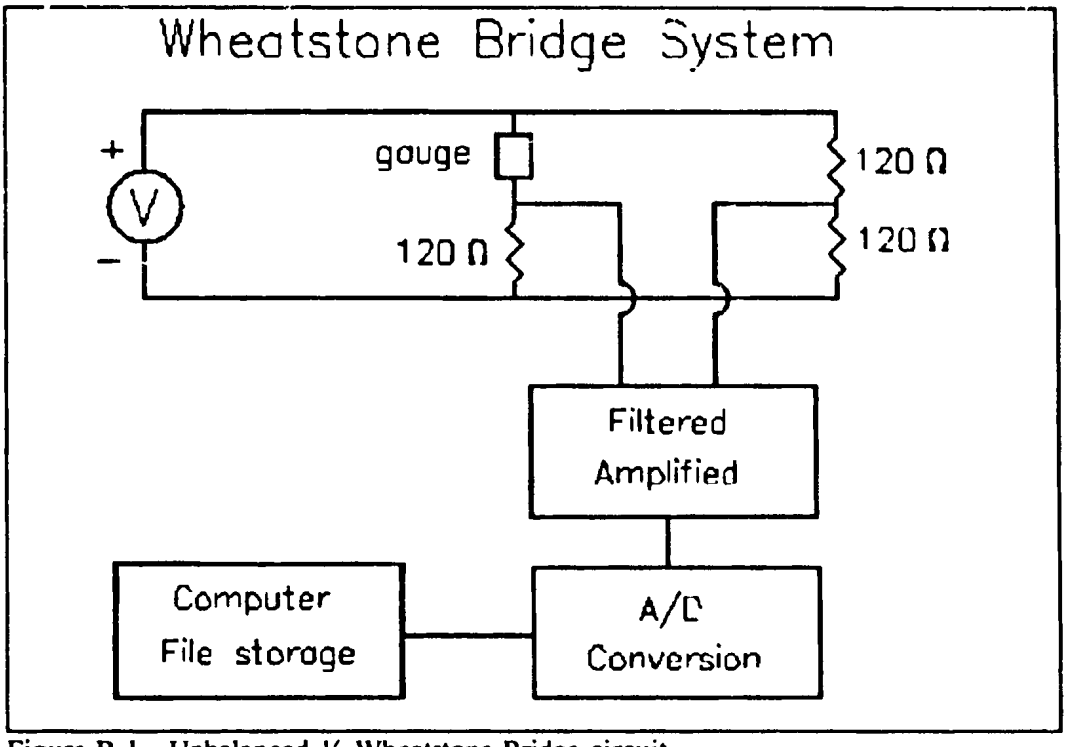

Figure B-1. Unbalanced ¼ Wheatstone Bridge circuit.

systems. The system schematic is given in Figure B-2. In the basic MUGS set up, 32 ¼ bridge arms are connected in parallel to a single regulated DC power supply. The resistors used are not precision resistors but much less expensive 1% resistors, costing only a few cents each. A 32 channel 16 bit A/D converter connected to a microcomputer reads the voltage directly across each strain gauge (referenced to a common side of the parallel arrangement) as shown in Figure B-2. In this arrangement, the strain gauges are read "unbridged" (hence the name) since there is no non strain gauge bridge arm to reference.

The particular A/D system used for this experiment is the Keithley 500A DAC which provides 64 channels of A/D input enabling the use of two of the basic units

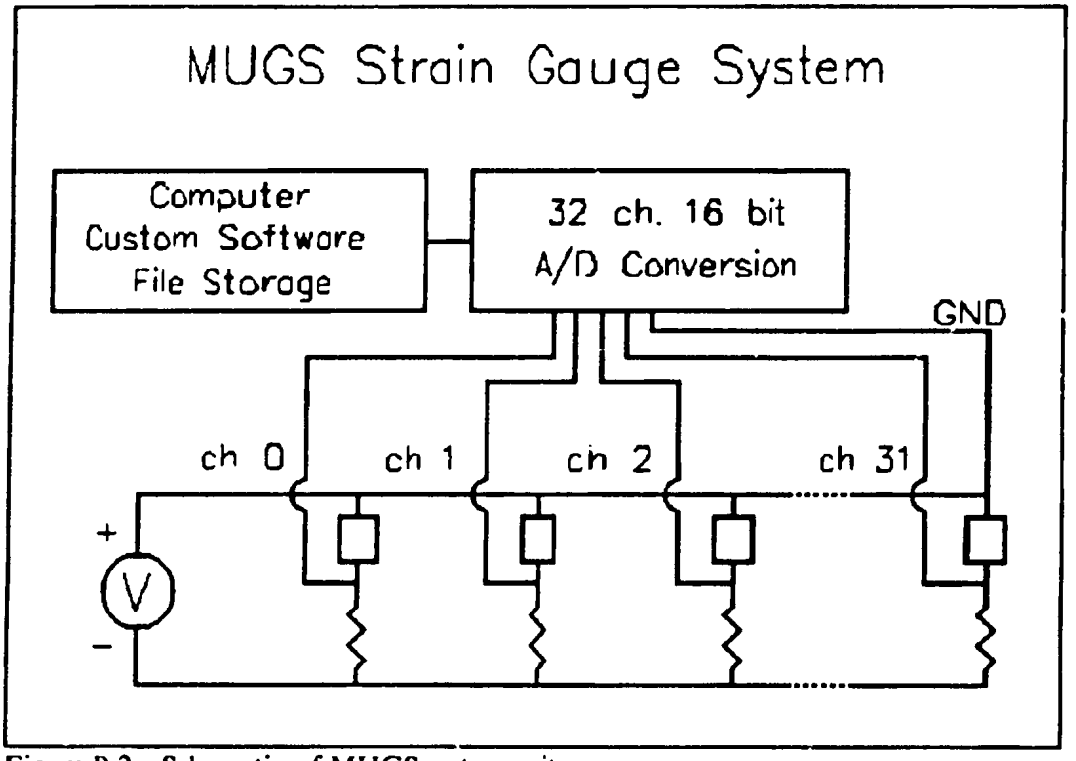

Figure B-2. Schematic of MUGS system unit.

shown in Figure B-2. For each group of 32 channels, one gauge is sacrificed as a reference gauge (channel 0), thus providing a total of 62 active gauges. These reference gauges are bonded to the same material as the other gauges, but remain unstrained throughout an experiment to measure the voltage changes resulting from transient temperature and supply voltage fluctuations.

Prior to running an experiment, the strain gauges and power supply are allowed to warm up for several hours. The normal supply voltage to the system should be 5 to 10 V DC. When the system is warmed up, the strain gauges are calibrated using the procedure outlined in section B-3. After this and before any load is applied, the system software reads each strain gauge channel several thousand times and averages to get a

stable unstrained voltage. During testing, each channel is read 200 times and averaged to reduce noise. The strain recorded by each gauge is then calculated by subtracting the gauge unstrained voltage and the change in the reference gauge voltage from the averaged gauge voltage. When the software is used for data acquisition only, a complete set of strains form all 62 active gauges is generated every 15 seconds and when the software is providing loading control a complete set of strains is generated approximately every 3 minutes.

B-2. Testing of MUGS System

To test the accuracy and precision of the MUGS system, the aluminum cantilever beam apparatus shown in Figure B-3 was constructed. Four strain gauges were positioned near the fixed end of the beam; two on the top (tensile gauges) and two on the bottom (compressive gauges). Four weights were added to the beam and the strain gauge response was measured using the MUGS system and using a BLH Electronics Inc. Model 1200 Digital Strain Indicator. As well, these results were also compared to the theoretical result determined assuming pure bending in the beam (Beer and Johnston, 1985).

Figure B-4 graphs the results of the MUGS results compared with the BLH results, indicated by the solid lines. Within experimental error, these results are almost identical and confirm the accuracy of the MUGS system. Precision of this nature is more than acceptable and is less noisy than some commercial systems. Figure B-5 compares the MUGS results with the theoretical results and shows that the assumption

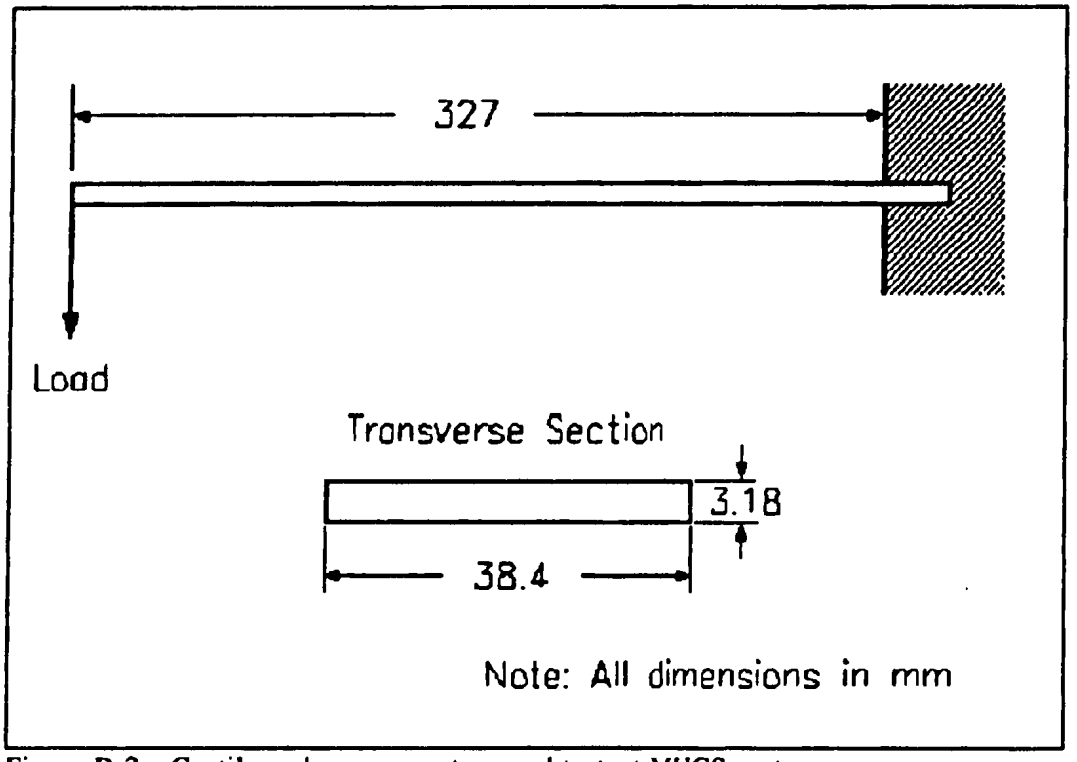

Figure B-3. Cantilever beam apparatus used to test MUGS system.

of pure bending is not valid for the beam, since the mismatch increases the more the beam is bent. Overall, these results confirm the viability and simplicity of the MUGS system approach and its suitability in experiments where dynamic measurements are not necessary.

B-3. Strain Gauge Calibration Procedure.

After the strain gauge system has warmed up and before any load is applied each active gauge channel must be calibrated. This is accomplished by shunting a precision resistor across each gauge and recording the resulting voltage change. Typically, this can be recorded in the same data file as the experimental data, providing that it is done

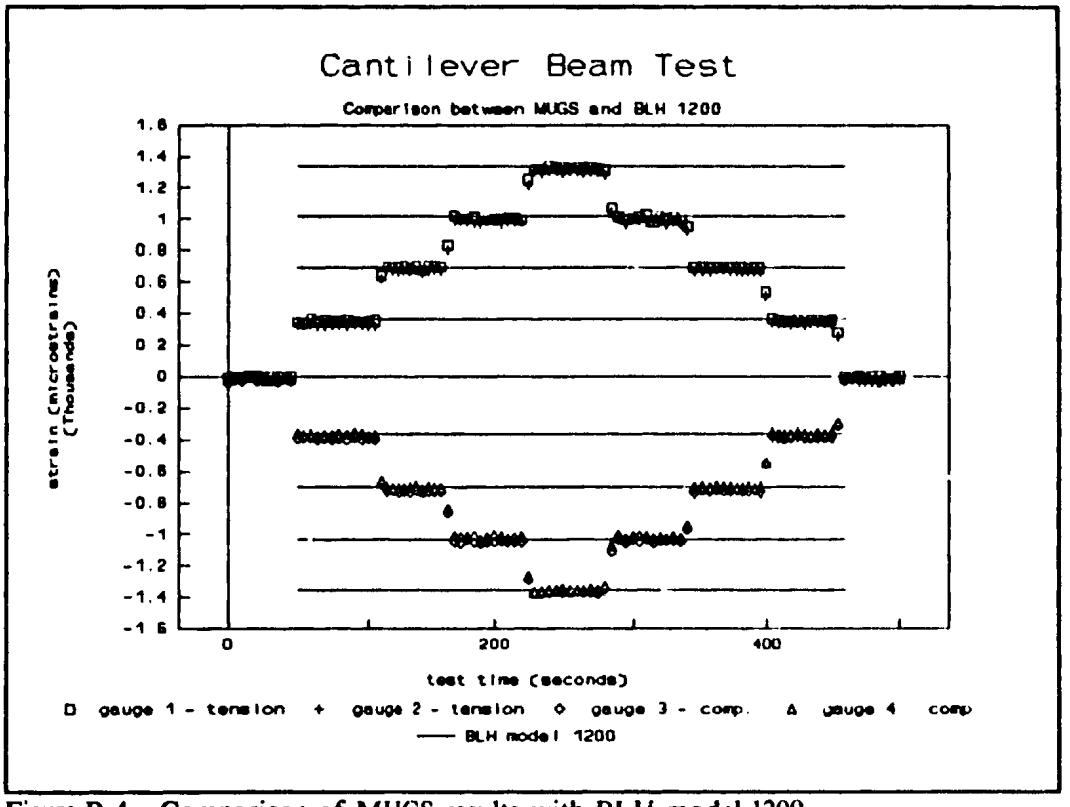

Figure B-4. Comparison of MUGS results with BLH model 1200.

before any load is applied. The equivalent strain is calculated using:

$$E = \frac{-R_g * 10^6}{GF(R_g + R_{sh})} \qquad \text{Eqn B-1}$$

where: E = equivalent strain ($\mu\epsilon$)
R_g = resistance of gauge (Ω)
R_{sh} = resistance of shunt resistor (Ω)
GF = gauge factor (dimensionless)

and the calibration factor is calculated using:

$$CF = E/V \qquad \text{Eqn B-2}$$

where: CF = Calibration Factor ($\mu\epsilon$/V)
E = equivalent strain ($\mu\epsilon$)
V = voltage change when shunt is added (V)

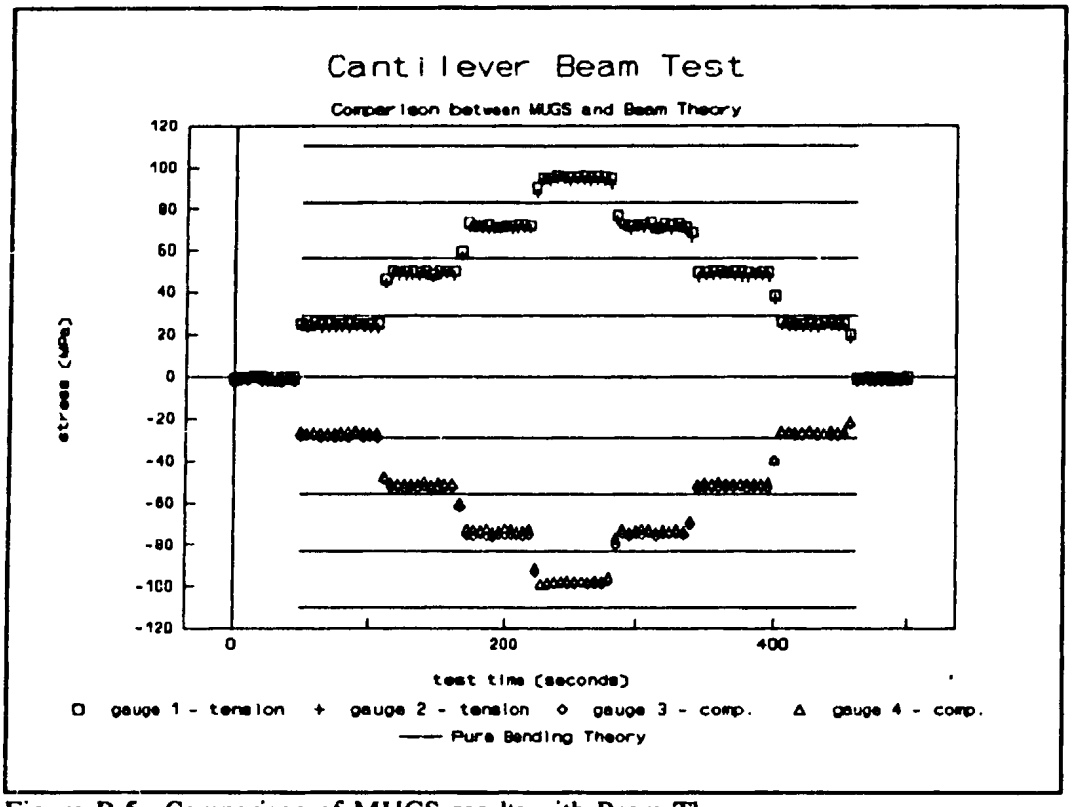

Figure B-5. Comparison of MUGS results with Beam Theory.

The calibration factors for all gauges should be similar, but not exact, since precision resistors are not used. The strain measured by each strain gauge is then calculated by multiplying the strain gauge voltage recorded in the data file by its calibration factor to give results in microstrains ($\mu\epsilon$).

Appendix C - Numerical Loading Control Software Algorithm

The control software provides displacement controlled loading for the biaxial loading frame. It provides precise control of the resolved normal and shear loads applied to the mean fracture plane while preventing any rapid movement of the actuators associated with fracture slip or secondary fracturing. This enables a shear test to proceed into the post shear failure region of the loading cycle, a capability not available with most other load controlled loading frames.

Prior to testing, the servo controller for each frame actuator is configured for displacement control, meaning that the displacement applied at each actuator is kept constant and does not drift. DC voltages are applied to each of the actuator controllers by the software via an Analog to Digital converter. These voltages are translated by the servo controllers into fixed positions of the actuators. The software operator specifies a displacement rate for each actuator and a desired normal and shear stress. Loadcells mounted in line with each actuator measure the loads applied which are relayed to the software via a Digital to Analog converter. Five times a second the software calculates the measured normal and shear stresses on the mean fracture plane and compares them to the user specified normal and shear stresses. Depending on the condition of this comparison, two of the following four actions is taken:

IF measured normal load < desired normal load THEN
    increase both actuators by specified normal load displacement rate

IF measured normal load > desired normal load THEN
decrease both actuators by specified normal load displacement rate

IF measured shear load < desired shear load THEN
increase actuator # 1 and decrease actuator # 2 by specified shear displacement rate

IF measured shear load > desired shear load THEN
decrease actuator # 1 and increase actuator # 2 by specified shear displacement rate

Following these actions, the actuator positions are slowly adjusted until the user specified stress conditions are met. If sudden stress changes occur on the fracture, the loading software returns to the desired stress condition in a controlled manner. At any time during an experiment, the software operator can modify the desired fracture normal stress, and desired fracture shear stress or the displacement rate for any actuator. The operator can also instantly freeze loading by automatically swapping the desired fracture stresses with the corresponding measured current values. Both positive and negative shear stresses can be applied, where a positive shear stress is in the direction of actuator #2 and vice versa. This algorithm has enabled controlled shear testing beyond the peak of the shear displacement curve while maintaining the applied fracture normal stress within 1% accuracy.

Operating concurrently with this algorithm are data acquisition and storage loops which record information from the variety of transducers, strain gauges and accelerometers mounted on the loading frame and test sample, display them in real time on the computer screen and store them to computer file.

Appendix D - Strain Gauge Correction Procedures

D-1. Filtering of MUGS Strain Gauge Records.

Due to gauge overheating, the excitation voltage of the MUGS strain gauges was reduced from it's normal value of 10 V DC to approximately 1.5 V DC. This resulted in unacceptable noise levels in the all resulting data sets. The use of a low pass convolution filter (Telford et al., 1990) with a maximum wavelength of 20000 seconds effectively removed this noise, as shown in Figure D-1. Each filtered data set was then averaged over intervals of constant applied load. This was considered valid because other, less noisier strain gauge records portrayed a constant voltage over such intervals.

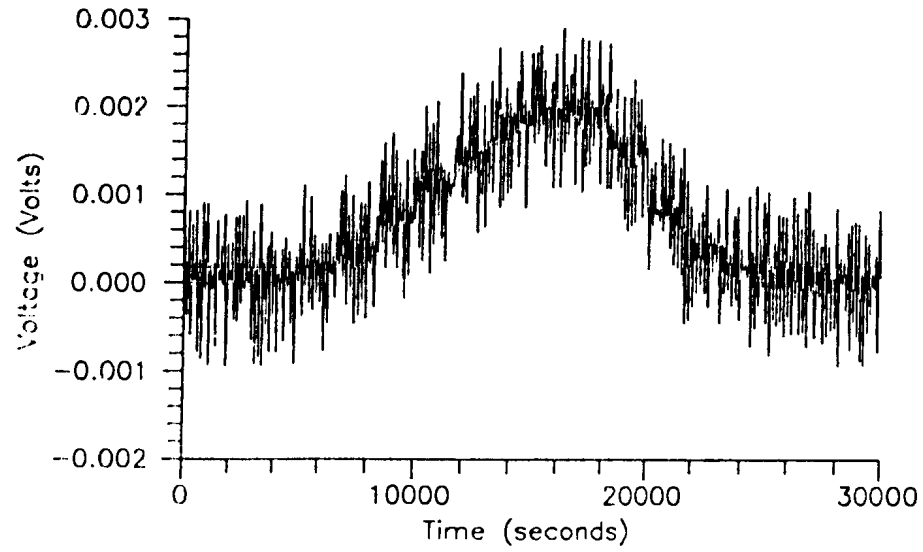

(a)

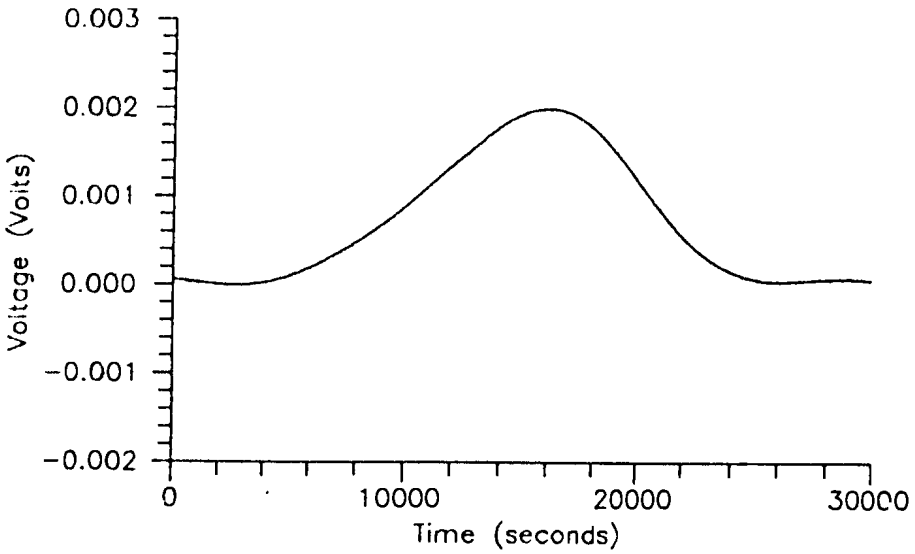

(b)

Figure D-1. (a) Noisy strain gauge data set recorded using MUGS system and (b) strain gauge record corrected by application of low pass convolution filter.

D-2. Removal of Self Warming Response From HP Strain Gauge Records.

During the second normal loading cycle, many gauges recorded using the HP 3497A data acquisition systems were masked by an exponential self warming response as shown in Figure D-2. To correct this condition, the bad data record was loaded into a computer spreadsheet and scaled so that the first data value was zero. This was accomplished by subtracting the value of the first data record from itself and all other data values in the strain gauge record. This self warming response was determined by a trial and error fit of a curve of the form $f(t) = At^b$ to the zeroed data record as is also shown in Figure D-2. This fitted curve was iteratively adjusted in the computer spreadsheet by changing values of A and b, plotting the resulting curve on the same axis as the zeroed data record and repeating this process until the fitted curve was parallel and coincident to the beginning and ending portions of the data record. This was considered a valid approach, since other strain gauge records that were not influenced by self warming responses indicated that these regions were generally at zero constant voltage. The bad strain gauge records were then corrected by subtracting the estimated self warming curve from the original data record as is shown in Figure D-3. Generally, the self warming response of each strain gauge was different, so this correction procedure was repeated for each bad strain gauge record.

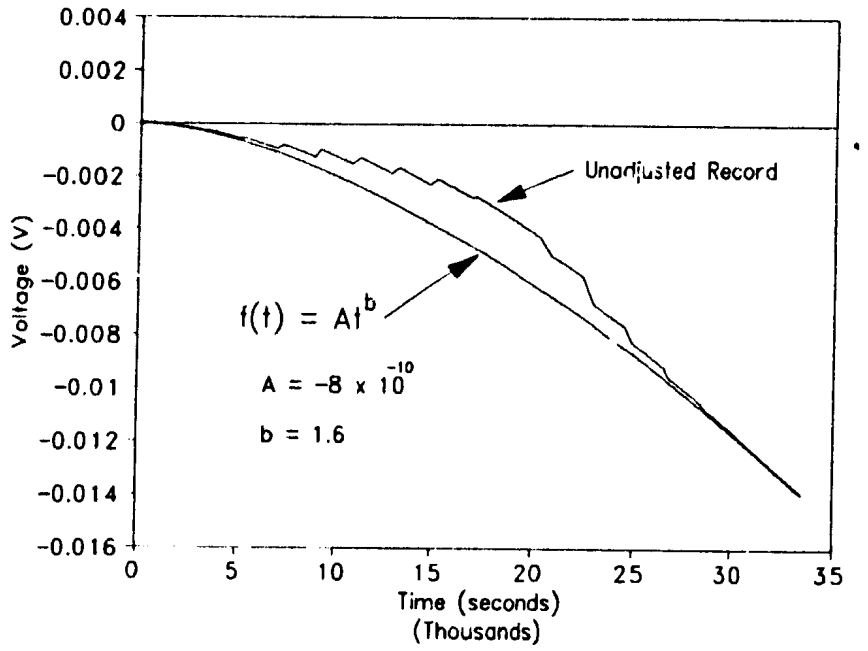

Figure D-2. Zeroed strain gauge record masked by an exponential warming trend and an empirically fitted estimate of the warming trend.

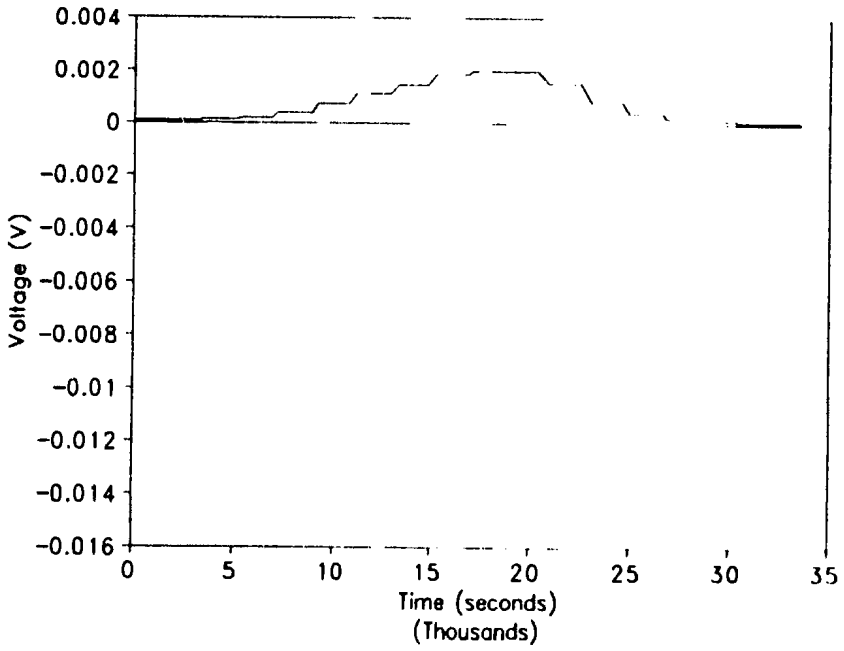

Figure D-3. Corrected strain gauge record after numerical subtraction of estimated self warming response from the zeroed data record.

Appendix E - Strain Gauge Positions in Physical Model

The procedures used in construction of the concrete physical model are outlined in Section 3.1. Table E-1 provides the coordinates of the strain gauges cast into the physical model with respect to a profile plane through the model, as shown in Figure E-1. This information is meant to augment the information presented schematically in Figure 3-1. As well, the strain gauge labels presented in Table E-1 are used in Appendix F which provides tables comparing the strains and approximated stresses measured during the physical experiment to stresses which were predicted from numerical modelling.

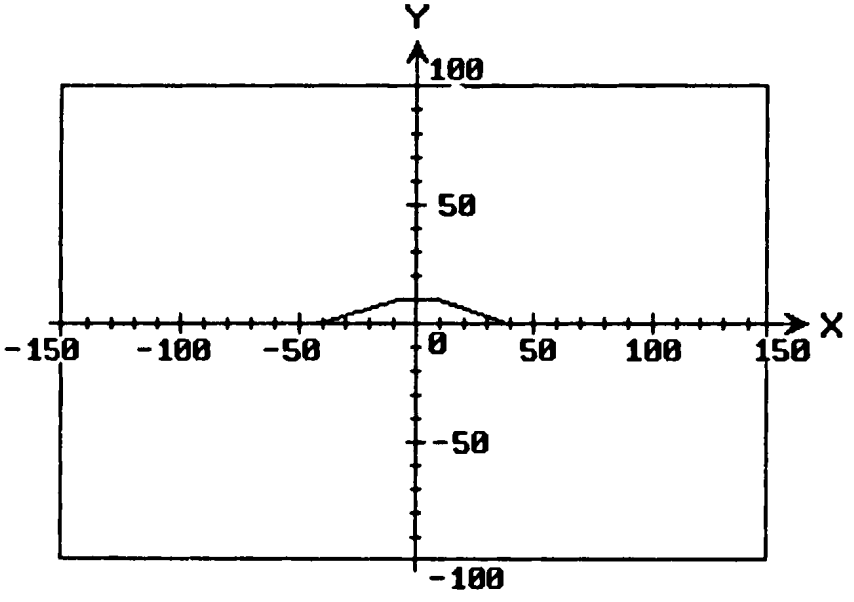

Figure E-1. Coordinate convention for strain gauge positions given in Table E-1. Axes are labelled in millimeters.

Table E-1. Strain gauge labels and positions within the physical model
Strain gauge coordinates are with respect to Figures E-1 and 3-1
The analysis label refers to the name assigned to the strain gauge during data analysis, such as in Appendix F.

gauge #	x -coor (mm)	y-coor (mm)	orient (R,V,H)	analysis label
1	-109	-61	R1	
2	-109	-61	R2	
3	-109	-61	R3	
4	-78	-75	R1	
5	-78	-75	R2	
6	-78	-75	R3	
7	-49	-72	V	tv1
8	-49	-73	H	th1
9	-30	-72	V	tv2
10	-12	-72	V	tv3
11	-109	-31	R1	
12	-109	-31	R2	
13	-109	-31	R3	
14	-78	-26	R1	
15	-78	-26	R2	
16	-78	-26	R3	
17	-49	-39	V	tv4
18	-49	-40	H	th2
19	-30	-48	V	tv5
20	-30	-49	H	th3
21	-12	-48	V	tv6
22	-12	-49	H	th4
23	-31	-26	R1	
24	-31	-26	R2	
25	-31	-26	R3	
26	-12	-26	V	tv7
27	-12	-26	H	th5
28	-49	-13	V	tv8
29	-49	-14	H	th6
30	-31	-10	V	tv9
31	-31	-10	H	th7
32	-12	-4	V	tv10

gauge #	x -coor (mm)	y-coor (mm)	orient (R,V,H)	analysis label
33	-12	-5	H	th8
34	13	-72	V	tv11
35	32	-72	V	tv12
36	50	-63	R1	
37	50	-63	R2	
38	50	-63	R3	
39	77	-63	V	tv13
40	107	-60	R1	
41	107	-60	R2	
42	107	-60	R3	
43	13	-49	V	tv14
44	13	-49	H	th9
45	32	-48	V	tv15
46	32	-49	H	th10
47	13	-27	V	tv16
48	13	-26	H	th11
49	32	-27	R1	
50	32	-27	R2	
51	32	-27	R3	
52	50	-39	V	tv17
53	50	-40	H	th12
54	77	-33	V	tv18
55	13	-5	V	tv19
56	13	-5	H	th13
57	32	-11	V	tv20
58	32	-11	H	th14
59	50	-13	V	tv21
60	50	-14	H	th15
61	77	-12	R1	
62	77	-12	R2	
63	77	-12	R3	
64	107	-20	R1	

Table E-1 continued .....

gauge #	x-coor (mm)	y-coor (mm)	orient (R,V,H)	analysis label
65	107	-20	R2	
66	107	-20	R3	
67	13	29	V	tv22
68	13	29	H	
69	32	22	V	tv23
70	32	22	H	th16
71	50	19	V	tv24
72	50	19	H	th17
73	77	16	R1	
74	77	16	R2	
75	77	16	R3	
76	13	51	V	tv25
77	13	51	H	th18
78	32	50	R1	
79	32	50	R2	
80	32	50	R3	
81	50	46	V	tv26
82	50	46	H	th19
83	77	45	R1	
84	77	45	R2	
85	77	45	R3	
86	107	31	R1	
87	107	31	R2	
88	107	31	R3	
89	13	78	V	tv27
90	32	74	V	tv28
91	32	73	H	th20
92	50	69	V	tv29
93	50	69	H	th21
94	77	69	V	
95	107	67	R1	
96	107	67	R2	
97	107	67	R3	
98	-109	30	R1	
99	-109	30	R2	
100	-109	30	R3	
101	-78	17	R1	
102	-78	17	R2	
103	-78	17	R3	
104	-49	19	V	tv30
105	-49	19	H	th22
106	-31	21	V	tv31
107	-31	21	H	th23
108	-13	28	V	tv32
109	-13	29	H	th24
110	-78	46	R1	
111	-78	46	R2	
112	-78	46	R3	
113	-49	38	V	
114	-49	38	H	th25
115	-31	49	R1	
116	-31	49	R2	
117	-31	49	R3	
118	-13	51	V	
119	-13	51	H	th26
120	-109	65	R1	
121	-109	65	R2	
122	-109	65	R3	
123	-78	65	V	tv33
124	-49	68	V	tv34
125	-49	68	H	th27
126	-31	73	V	tv35
127	-31	73	H	th28
128	-13	77	V	

Appendix F - Tabulated Strain Gauge and Numerical Modelling Data

Tables F-1 through F-6 provide the strain gauge data used to produce the contour plots of strain presented in Chapter 3. One table is given for each loading cycle and, where available, data for load steps not presented in the chapter are also provided. Approximate stresses are calculated from the stress-strain conversion factor derived in Chapter 3 and these are given in the tables. Note, however, that for reasons given in Section 3-2, approximate values of tensile stress are unreliable. The numerical modelling data sets, used to produce the contour plots of stress presented in Chapter 2, were analyzed and the predicted stresses at the same locations as the strain gauges are also given. This was done using a computer program which overlaid the strain gauge coordinates onto the numerically predicted stress fields, found the three nearest element centroids to each strain gauge position, and interpolated the corresponding stress value using a weighted mean technique. Where numerical or physical modelling data is not available for the load steps presented, the column corresponding to the measured strain or the predicted stresses is omitted. Finally, when a strain gauge was malfunctioning or damaged and did not provide reliable strain information, a "b/g" symbol is given for the strain value and no corresponding stress value is calculated.

Table F-1. Measured strains and approximated stresses from first normal loading cycle, along with numerically predicted stresses at the same position in the physical model.

		Applied normal stress (MPa) and portion of loading cycle (up = loading cycle, dn = unloading)										
		2 up			5 up			8 up			13.4 peak	
gauge label	gauge orient. (H or V)	meas. strain (μE)	approx. stress (MPa)	pred. stress (MPa)	meas. strain (μE)	approx. stress (MPa)	pred. stress (MPa)	meas. strain (μE)	approx stress (MPa)	pred. stress (MPa)	meas strain (μE)	approx stress (MPa)
th1	H	74	3.7	1.4	168	8.4	3.2	202	10.1	5.1	306	15.3
th2	H	93	4.7	1.4	210	10.5	3.4	266	13.3	5.3	422	21.1
th3	H	61	3.0	1.7	212	10.6	3.9	273	13.7	5.8	410	20.5
th4	H	108	5.4	1.8	248	12.4	4.2	298	14.9	6.5	422	21.1
th5	H	120	6.0	1.7	264	13.2	4.0	331	16.5	6.2	506	25.3
th6	H	93	4.7	1.4	236	11.8	3.4	320	16.0	5.4	555	27.7
th7	H	103	5.2	1.6	289	14.4	3.7	380	19.0	5.8	608	30.4
th8	H	126	6.3	1.2	354	17.7	3.2	426	21.3	5.7	606	30.3
th9	H	b/g		1.8	b/g		4.2	b/g		6.5	b/g	
th10	H	b/g		1.8	b/g		4.2	b/g		6.4	b/g	
th11	H	b/g		2.2	b/g		4.9	b/g		7.3	b/g	
th12	H	b/g		1.8	b/g		4.2	b/g		6.6	b/g	
th13	H	b/g		2.9	b/g		6.0	b/g		8.3	b/g	
th14	H	b/g		2.1	b/g		4.6	b/g		7.0	b/g	
th15	H	b/g		1.9	b/g		4.3	b/g		6.7	b/g	
th16	H	b/g		2.1	b/g		4.6	b/g		6.9	b/g	
th17	H	b/g		1.9	b/g		4.4	b/g		6.8	b/g	
th18	H	b/g		1.8	b/g		4.1	b/g		6.3	b/g	
th19	H	b/g		1.9	b/g		4.3	b/g		6.6	b/g	
th20	H	b/g		1.5	b/g		3.5	b/g		5.4	b/g	
th21	H	b/g		1.6	b/g		3.6	b/g		5.6	b/g	
th22	H	49	2.5	1.4	171	8.5	3.4	244	12.2	5.3	360	18.0
th23	H	53	2.7	1.6	204	10.2	3.7	290	14.5	5.8	354	17.7
th24	H	52	2.6	1.6	247	12.3	3.8	361	18.0	6.2	596	29.8
th25	H	24	1.2	1.5	136	6.8	3.5	191	9.6	5.4	-35	-1.7
th26	H	15	0.8	1.9	119	5.9	4.3	146	7.3	6.4	-88	-4.4
th27	H	8	0.4	1.4	22	1.1	3.3	8	0.4	5.2	-66	-3.3
th28	H	0	0.0	1.6	103	5.2	3.6	138	6.9	5.5	137	6.9
tv1	V	159	8.0	1.9	260	13.0	4.7	221	11.0	7.3	118	5.9
tv2	V	149	7.4	2.0	232	11.6	4.7	206	10.3	7.4	156	7.8
tv3	V	181	9.1	1.9	265	13.3	4.7	238	11.9	7.4	141	7.1

Table F-1. continued .....

		Applied normal stress (MPa) and portion of loading cycle (up = loading cycle, dn = unloading)										
		2 up			5 up			8 up			13.4 peak	
gauge label	gauge orient. (H or V)	meas. strain (μE)	approx. stress (MPa)	pred. stress (MPa)	meas. strain (μE)	approx. stress (MPa)	pred. stress (MPa)	meas. strain (μE)	approx. stress (MPa)	pred. stress (MPa)	meas. strain (μE)	approx. stress (MPa)
tv4	V	205	10.3	1.9	428	21.4	4.5	507	25.4	6.9	563	28.1
tv5	V	150	7.5	2.1	325	16.2	4.8	361	18.0	7.2	356	17.8
tv6	V	41	2.0	1.9	60	3.0	4.6	38	1.9	7.1	33	1.6
tv7	V	121	6.0	2.0	198	9.9	4.6	197	9.9	6.8	187	9.3
tv8	V	64	3.2	1.8	131	6.5	4.3	129	6.4	6.6	153	7.6
tv9	V	83	4.2	1.8	206	10.3	4.3	223	11.2	6.6	259	12.9
tv10	V	123	6.2	1.8	193	9.6	4.2	196	9.8	6.6	221	11.1
tv11	V	b/g		1.9	b/g		4.6	b/g		7.4	b/g	
tv12	V	b/g		1.7	b/g		4.3	b/g		6.9	b/g	
tv13	V	b/g		1.6	b/g		4.1	b/g		6.5	b/g	
tv14	V	b/g		1.8	b/g		4.3	b/g		6.7	b/g	
tv15	V	b/g		1.7	b/g		4.2	b/g		6.5	b/g	
tv16	V	b/g		1.9	b/g		4.4	b/g		6.7	b/g	
tv17	V	b/g		1.7	b/g		3.9	b/g		5.9	b/g	
tv18	V	b/g		1.5	b/g		3.4	b/g		5.2	b/g	
tv19	V	b/g		2.2	b/g		4.8	b/g		7.0	b/g	
tv20	V	b/g		2.0	b/g		4.4	b/g		6.4	b/g	
tv21	V	b/g		1.7	b/g		3.9	b/g		5.8	b/g	
tv22	V	b/g		2.0	b/g		4.5	b/g		6.7	b/g	
tv23	V	b/g		1.9	b/g		4.2	b/g		6.3	b/g	
tv24	V	b/g		1.7	b/g		3.9	b/g		5.7	b/g	
tv25	V	b/g		1.8	b/g		4.3	b/g		6.8	b/g	
tv26	V	b/g		1.7	b/g		4.0	b/g		6.1	b/g	
tv27	V	b/g		1.9	b/g		4.7	b/g		7.4	b/g	
tv28	V	b/g		1.8	b/g		4.5	b/g		7.2	b/g	
tv29	V	b/g		1.7	b/g		4.3	b/g		6.8	b/g	
tv30	V	210	10.5	1.8	481	24.1	4.4	571	28.6	6.7	769	38.5
tv31	V	62	3.1	1.9	213	10.7	4.4	227	11.3	6.8	234	11.7
tv32	V	157	7.9	2.1	362	18.1	4.7	423	21.2	7.0	668	33.4
tv33	V	79	4.0	1.7	243	12.1	4.3	311	15.6	6.6	277	13.9
tv34	V	67	3.3	2.0	278	13.9	4.7	398	19.9	7.2	341	17.0
tv35	V	74	3.7	2.0	207	10.3	4.8	244	12.2	7.4	159	8.0

Table F-1. continued .....

		Applied normal stress (MPa) and portion of loading cycle (up = loading cycle, dn = unloading)									
		8 dn		5 dn			2 dn			0 dn	
gauge label	gauge orient. (H or V)	meas. strain (μE)	approx. stress (MPa)	meas. strain (μE)	approx. stress (MPa)	pred stress (MPa)	meas. strain (μE)	approx. stress (MPa)	pred stress (MPa)	meas strain (μE)	approx stress (MPa)
th1	H	224	11.2	169	8.5	3.3	147	7.3	1.2	100	5.0
th2	H	286	14.3	198	9.9	3.5	149	7.5	1.4	67	3.4
th3	H	311	15.5	242	12.1	3.9	187	9.4	1.7	112	5.6
th4	H	301	15.1	219	11.0	4.5	165	8.3	2.3	88	4.4
th5	H	373	18.6	282	14.1	4.3	230	11.5	2.2	152	7.6
th6	H	403	20.1	268	13.4	3.5	163	8.2	1.4	-9	-0.5
th7	H	518	25.9	441	22.0	3.9	377	18.8	1.8	285	14.2
th8	H	510	25.5	461	23.1	4.2	427	21.4	2.2	368	18.4
th9	H	b/g		b/g		4.5	b/g		2.2	b/g	
th10	H	b/g		b/g		4.3	b/g		1.9	b/g	
th11	H	b/g		b/g		5.1	b/g		2.6	b/g	
th12	H	b/g		b/g		4.3	b/g		1.8	b/g	
th13	H	b/g		b/g		5.8	b/g		3.0	b/g	
th14	H	b/g		b/g		4.7	b/g		2.2	b/g	
th15	H	b/g		b/g		4.5	b/g		1.9	b/g	
th16	H	b/g		b/g		4.7	b/g		2.2	b/g	
th17	H	b/g		b/g		4.5	b/g		1.9	b/g	
th18	H	b/g		b/g		4.4	b/g		2.2	b/g	
th19	H	b/g		b/g		4.4	b/g		1.8	b/g	
th20	H	b/g		b/g		3.6	b/g		1.5	b/g	
th21	H	b/g		b/g		3.6	b/g		1.4	b/g	
th22	H	240	12.0	148	7.4	3.4	96	4.8	1.3	28	1.4
th23	H	223	11.2	124	6.2	3.9	48	2.4	1.7	-67	-3.4
th24	H	416	20.8	265	13.3	4.5	170	8.5	2.4	32	1.6
th25	H	-152	-7.6	-225	-11.2	3.6	-265	-13.2	1.5	-306	-15.3
th26	H	-168	-8.4	-261	-13.1	4.5	-341	-17.1	2.3	-478	-23.9
th27	H	-147	-7.3	-201	-10.0	3.3	-228	-11.4	1.3	-245	-12.2
th28	H	122	6.1	98	4.9	3.6	83	4.2	1.5	67	3.3
tv1	V	68	3.4	31	1.5	4.8	3	0.2	2.3	-39	-2.0
tv2	V	127	6.4	116	5.8	4.9	115	5.8	2.3	83	4.1
tv3	V	116	5.8	119	5.9	5.0	104	5.2	2.4	47	2.3

Table F-1. continued .....

		Applied normal stress (MPa) and portion of loading cycle (up = loading cycle, dn = unloading)									
		8 dn		5 dn			2 dn			0 dn	
gauge label	gauge orient. (H or V)	meas. strain (μE)	approx. stress (MPa)	meas. strain (μE)	approx. stress (MPa)	pred. stress (MPa)	meas. strain (μE)	approx. stress (MPa)	pred. stress (MPa)	meas. strain (μE)	approx. stress (MPa)
tv4	V	469	23.4	381	19.1	4.5	276	13.8	2.4	39	1.9
tv5	V	306	15.3	268	13.4	4.9	198	9.9	2.5	7	0.3
tv6	V	16	0.8	39	1.9	4.9	35	1.7	2.5	-9	-0.5
tv7	V	153	7.6	120	6.0	4.7	79	3.9	2.4	-29	-1.5
tv8	V	119	6.0	135	6.7	4.5	140	7.0	2.4	102	5.1
tv9	V	222	11.1	206	10.3	4.6	184	9.2	2.5	104	5.2
tv10	V	208	10.4	223	11.2	4.7	217	10.8	2.7	162	8.1
tv11	V	b/g		b/g		4.9	b/g		2.3	b/g	
tv12	V	b/g		b/g		4.7	b/g		2.2	b/g	
tv13	V	b/g		b/g		4.2	b/g		1.8	b/g	
tv14	V	b/g		b/g		4.6	b/g		2.3	b/g	
tv15	V	b/g		b/g		4.5	b/g		2.2	b/g	
tv16	V	b/g		b/g		4.6	b/g		2.4	b/g	
tv17	V	b/g		b/g		4.0	b/g		2.1	b/g	
tv18	V	b/g		b/g		3.4	b/g		1.7	b/g	
tv19	V	b/g		b/g		4.9	b/g		2.7	b/g	
tv20	V	b/g		b/g		4.4	b/g		2.4	b/g	
tv21	V	b/g		b/g		4.0	b/g		2.1	b/g	
tv22	V	b/g		b/g		4.6	b/g		2.4	b/g	
tv23	V	b/g		b/g		4.3	b/g		2.2	b/g	
tv24	V	b/g		b/g		3.9	b/g		2.0	b/g	
tv25	V	b/g		b/g		4.7	b/g		2.4	b/g	
tv26	V	b/g		b/g		4.1	b/g		2.1	b/g	
tv27	V	b/g		b/g		4.9	b/g		2.3	b/g	
tv28	V	b/g		b/g		4.7	b/g		2.1	b/g	
tv29	V	b/g		b/g		4.4	b/g		1.9	b/g	
tv30	V	812	40.6	788	39.4	4.5	744	37.2	2.3	646	32.3
tv31	V	234	11.7	217	10.9	4.6	186	9.3	2.4	101	5.0
tv32	V	667	33.4	651	32.5	4.8	611	30.6	2.4	511	25.5
tv33	V	-28	-1.4	-375	-18.7	4.3	-557	-27.9	2.0	-799	-40.0
tv34	V	237	11.8	75	3.8	4.8	-62	-3.1	2.3	-268	-13.4
tv35	V	232	11.6	179	8.9	5.0	75	3.7	2.3	-114	-5.7

Table F-2. Measured strains and approximated stresses from second normal loading cycle, along with numerically predicted stresses at the same position in the physical model.

		Applied normal stress (MPa) and portion of loading cycle (up = loading cycle, dn = unloading)										
		2 up			5 up			8 up			13.4 peak	
gauge label	gauge orient. (H or V)	meas. strain (μE)	approx. stress (MPa)	pred. stress (MPa)	meas. strain (μE)	approx. stress (MPa)	pred. stress (MPa)	meas. strain (μE)	approx. stress (MPa)	pred. stress (MPa)	meas. strain (μE)	approx. stress (MPa)
th1	H	45	2.2	1.4	80	4.0	3.2	132	6.6	5.0	216	10.8
th2	H	67	3.3	1.4	133	6.7	3.3	221	11.0	5.2	339	16.9
th3	H	96	4.8	1.5	147	7.3	3.5	220	11.0	5.5	348	17.4
th4	H	66	3.3	1.7	125	6.3	3.7	203	10.2	5.9	323	16.2
th5	H	98	4.9	1.7	175	8.7	3.7	270	13.5	5.8	418	20.9
th6	H	133	6.7	1.4	217	10.9	3.3	333	16.6	5.3	521	26.0
th7	H	120	6.0	1.6	193	9.7	3.6	265	13.2	5.6	374	18.7
th8	H	100	5.0	1.6	160	8.0	3.7	215	10.8	5.7	296	14.8
th9	H	19	1.0	1.6	72	3.6	3.8	110	5.5	6.0	156	7.8
th10	H	67	3.3	1.6	114	5.7	3.8	144	7.2	6.0	160	8.0
th11	H	91	4.6	1.8	201	10.0	4.1	288	14.4	6.4	420	21.0
th12	H	47	2.4	1.7	88	4.4	4.0	126	6.3	6.3	219	11.0
th13	H	214	10.7	1.9	343	17.2	4.4	401	20.1	6.9	489	24.4
th14	H	-326	-16.3	1.8	-385	-19.2	4.1	-354	-17.7	6.6	-300	-15.0
th15	H	-179	-8.9	1.7	-181	-9.0	4.1	-141	-7.0	6.5	-65	-3.2
th16	H	117	5.8	1.8	247	12.4	4.1	366	18.3	6.5	527	26.3
th17	H	52	2.6	1.7	141	7.1	4.1	228	11.4	6.5	506	25.3
th18	H	57	2.8	1.6	218	10.9	3.7	339	17.0	5.9	497	24.8
th19	H	86	4.3	1.7	59	2.9	4.0	53	2.6	6.3	51	2.6
th20	H	39	2.0	1.4	137	6.9	3.3	255	12.8	5.2	621	31.1
th21	H	-22	-1.1	1.5	23	1.2	3.4	70	3.5	5.4	113	5.6
th22	H	64	3.2	1.4	120	6.0	3.3	191	9.5	5.2	308	15.4
th23	H	98	4.9	1.5	171	8.6	3.5	241	12.1	5.6	376	18.8
th24	H	123	6.1	1.7	229	11.4	3.8	347	17.3	5.9	568	28.4
th25	H	57	2.8	1.5	101	5.0	3.4	125	6.2	5.3	133	6.6
th26	H	125	6.2	1.6	249	12.5	3.7	388	19.4	5.8	563	28.1
th27	H	43	2.1	1.4	80	4.0	3.2	123	6.2	5.1	162	8.1
th28	H	25	1.2	1.5	40	2.0	3.4	62	3.1	5.3	91	4.5
tv1	V	81	4.1	1.8	67	3.4	4.3	61	3.1	6.8	62	3.1
tv2	V	-2	-0.1	1.8	-16	-0.8	4.4	-35	-1.8	7.0	-45	-2.2
tv3	V	25	1.3	1.9	-28	-1.4	4.4	-77	-3.9	7.0	-145	-7.2

Table F-2. continued .....

		Applied normal stress (MPa) and portion of loading cycle (up = loading cycle, dn = unloading)										
		2 up			5 up			8 up			13.4 peak	
gauge label	gauge orient. (H or V)	meas. strain (μE)	approx. stress (MPa)	pred. stress (MPa)	meas. strain (μE)	approx. stress (MPa)	pred. stress (MPa)	meas strain (μE)	approx. stress (MPa)	pred. stress (MPa)	meas. strain (μE)	approx. stress (MPa)
tv4	V	255	12.7	1.7	370	18.5	4.0	471	23.6	6.3	613	30.6
tv5	V	183	9.2	1.8	290	14.5	4.1	375	18.8	6.6	429	21.4
tv6	V	77	3.8	1.8	102	5.1	4.1	124	6.2	6.5	170	8.5
tv7	V	169	8.4	1.7	202	10.1	3.9	217	10.9	6.1	222	11.1
tv8	V	77	3.8	1.6	60	3.0	3.8	63	3.2	6.1	125	6.3
tv9	V	230	11.5	1.6	239	12.0	3.8	211	10.6	6.0	164	8.2
tv10	V	92	4.6	1.6	96	4.8	3.7	97	4.8	5.9	106	5.3
tv11	V	236	11.8	1.8	180	9.0	4.4	170	8.5	7.1	212	10.6
tv12	V	169	8.4	1.7	186	9.3	4.2	63	3.1	6.7	29	1.4
tv13	V	197	9.8	1.6	419	20.9	4.0	412	20.6	6.4	445	22.3
tv14	V	150	7.5	1.7	161	8.0	4.0	186	9.3	6.3	150	7.5
tv15	V	185	9.3	1.6	231	11.5	3.8	184	9.2	6.1	102	5.1
tv16	V	200	10.0	1.6	125	6.2	3.8	76	3.8	6.0	25	1.3
tv17	V	96	4.8	1.4	228	11.4	3.4	314	15.7	5.4	506	25.3
tv18	V	274	13.7	1.2	415	20.7	3.0	481	24.0	4.7	533	26.6
tv19	V	-203	-10.1	1.6	-182	-9.1	3.7	-135	-6.8	5.9	169	8.4
tv20	V	255	12.7	1.5	328	16.4	3.5	398	19.9	5.5	465	23.3
tv21	V	-138	-6.9	1.4	-304	-15.2	3.2	-427	-21.4	5.0	-529	-26.5
tv22	V	154	7.7	1.6	260	13.0	3.8	360	18.0	6.0	434	21.7
tv23	V	83	4.1	1.5	113	5.7	3.5	127	6.4	5.6	213	10.7
tv24	V	15	0.7	1.4	99	5.0	3.2	174	8.7	5.0	400	20.0
tv25	V	107	5.4	1.7	193	9.6	4.0	333	16.7	6.4	538	26.9
tv26	V	216	10.8	1.5	326	16.3	3.5	366	18.3	5.6	368	18.4
tv27	V	99	5.0	1.9	206	10.3	4.4	338	16.9	7.1	492	24.6
tv28	V	214	10.7	1.8	353	17.6	4.4	442	22.1	7.5	418	20.9
tv29	V	344	17.2	2	412	20.6	4	352	17.6	8	432	21.6
tv30	V	251	12.6	2	321	16.0	4	361	18.1	6	428	21.4
tv31	V	222	11.1	2	273	13.6	4	295	14.8	6	340	17.0
tv32	V	182	9.1	2	236	11.8	4	271	13.5	6	341	17.0
tv33	V	145	7.2	2	165	8.3	4	143	7.2	6	94	4.7
tv34	V	226	11.3	2	430	21.5	4	618	30.9	8	45	2.3
tv35	V	207	10.4	2	457	22.9	4	719	35.9	8	559	27.9

Table F-2. continued .....

		Applied normal stress (MPa) and portion of loading cycle (up = loading cycle, dn = unloading)									
		8 dn		5 dn			2 dn			0 dn	
gauge label	gauge orient. (H or V)	meas strain (μE)	approx stress (MPa)	meas strain (μE)	approx. stress (MPa)	pred stress (MPa)	meas strain (μE)	approx stress (MPa)	pred stress (MPa)	meas strain (μE)	approx stress (MPa)
th1	H	127	6.4	74	3.7	3.2	34	1.7	1.2	7	0.4
th2	H	217	10.9	138	6.9	3.4	77	3.9	1.3	-0	-0.0
th3	H	236	11.8	136	6.8	3.6	71	3.6	1.5	5	0.2
th4	H	209	10.4	120	6.0	3.9	62	3.1	1.8	-0	-0.0
th5	H	300	15.0	212	10.6	3.8	139	7.0	1.7	44	2.2
th6	H	399	19.9	278	13.9	3.4	116	5.8	1.3	-108	-5.4
th7	H	267	13.4	199	10.0	3.7	233	11.6	1.5	233	11.6
th8	H	198	9.9	140	7.0	3.8	203	10.2	1.7	258	12.9
th9	H	77	3.8	29	1.4	4.0	-38	-1.9	1.8	-67	-3.3
th10	H	94	4.7	59	3.0	3.9	12	0.6	1.6	-2	-0.1
th11	H	306	15.3	221	11.1	4.4	107	5.4	2.1	6	0.3
th12	H	133	6.7	72	3.6	4.1	29	1.4	1.7	-19	-1.0
th13	H	381	19.1	304	15.2	4.8	165	8.2	2.3	115	5.8
th14	H	-324	-16.2	-297	-14.9	4.4	-174	-8.7	1.9	-65	-3.2
th15	H	-142	-7.1	-170	-8.5	4.3	-129	-6.4	1.7	-246	-12.3
th16	H	385	19.2	246	12.3	4.3	97	4.8	1.9	-12	-0.6
th17	H	322	16.1	218	10.9	4.3	94	4.7	1.7	-6	-0.3
th18	H	b/g		b/g		3.9	b/g		1.8	b/g	
th19	H	-36	-1.8	-73	-3.6	4.1	-115	-5.7	1.7	-209	-10.4
th20	H	410	20.5	215	10.7	3.4	77	3.9	1.4	-26	-1.3
th21	H	39	1.9	-14	-0.7	3.4	-94	-4.7	1.3	-156	-7.8
th22	H	196	9.8	117	5.9	3.4	78	3.9	1.3	54	2.7
th23	H	264	13.2	174	8.7	3.6	122	6.1	1.5	60	3.0
th24	H	392	19.6	267	13.4	4.0	180	9.0	1.8	99	4.9
th25	H	40	2.0	2	0.1	3.5	-12	-0.6	1.3	-17	-0.9
th26	H	376	18.8	199	9.9	3.9	57	2.8	1.8	-30	-1.5
th27	H	49	2.5	10	0.5	3.3	-13	-0.6	1.2	-16	-0.8
th28	H	24	1.2	-10	-0.5	3.5	10	0.5	1.4	52	2.6
tv1	V	-4	-0.2	-48	-2.4	4.5	-109	-5.4	2.0	-198	-9.9
tv2	V	-84	-4.2	-79	-4.0	4.6	-61	-3.0	2.0	-55	-2.7
tv3	V	-171	-8.6	-142	-7.1	4.6	-119	-5.9	2.1	-143	-7.2

Table F-2. continued .....

		Applied normal stress (MPa) and portion of loading cycle (up = loading cycle, dn = unloading)									
		8 dn		5 dn			2 dn			0 dn	
gauge label	gauge orient. (H or V)	meas. strain (μE)	approx. stress (MPa)	meas. strain (μE)	approx. stress (MPa)	pred. stress (MPa)	meas. strain (μE)	approx. stress (MPa)	pred. stress (MPa)	meas. strain (μE)	approx. stress (MPa)
tv4	V	510	25.5	436	21.8	4.1	307	15.3	1.9	6	0.3
tv5	V	323	16.1	271	13.5	4.3	209	10.5	2.0	36	1.8
tv6	V	140	7.0	142	7.1	4.3	154	7.7	2.0	135	6.7
tv7	V	196	9.8	194	9.7	4.0	164	8.2	1.9	20	1.0
tv8	V	123	6.1	147	7.4	4.0	149	7.5	1.8	-0	-0.0
tv9	V	127	6.4	124	6.2	4.0	101	5.1	1.9	-92	-4.6
tv10	V	77	3.8	66	3.3	3.9	55	2.8	1.9	8	0.4
tv11	V	291	14.6	321	16.1	4.6	220	11.0	2.1	16	0.8
tv12	V	125	6.3	202	10.1	4.4	174	8.7	2.0	0	0.0
tv13	V	183	9.2	60	3.0	4.1	-43	-2.1	1.8	-34	-1.7
tv14	V	101	5.1	57	2.9	4.2	64	3.2	1.9	-2	-0.1
tv15	V	91	4.5	90	4.5	4.0	39	1.9	1.8	-125	-6.2
tv16	V	19	1.0	72	3.6	4.0	150	7.5	1.8	73	3.6
tv17	V	517	25.8	458	22.9	3.5	331	16.5	1.6	67	3.3
tv18	V	315	15.7	181	9.0	3.0	48	2.4	1.3	-33	-1.7
tv19	V	363	18.1	400	20.0	4.0	412	20.6	1.9	180	9.0
tv20	V	390	19.5	329	16.5	3.7	259	13.0	1.7	58	2.9
tv21	V	-332	-16.6	-177	-8.8	3.4	-56	-2.8	1.6	-2	-0.1
tv22	V	173	8.6	69	3.4	3.9	-47	-2.4	1.8	-63	-3.2
tv23	V	195	9.8	179	9.0	3.7	142	7.1	1.7	34	1.7
tv24	V	438	21.9	432	21.6	3.3	357	17.9	1.5	92	4.6
tv25	V	325	16.2	243	12.2	4.2	168	8.4	1.9	44	2.2
tv26	V	334	16.7	312	15.6	3.6	201	10.0	1.6	-11	-0.6
tv27	V	b/g		b/g		4.6	b/g		2.1	b/g	
tv28	V	129	6.5	137	6.9	4.5	90	4.5	2.0	130	6.5
tv29	V	435	21.7	468	23.4	4	445	22.3	2	30	1.5
tv30	V	377	18.9	371	18.5	4	385	19.2	2	335	16.8
tv31	V	301	15.1	304	15.2	4	304	15.2	2	260	13.0
tv32	V	287	14.4	258	12.9	4	266	13.3	2	221	11.0
tv33	V	-72	-3.6	-218	-10.9	4	-333	-16.6	2	-416	-20.8
tv34	V	-391	-19.6	-495	-24.8	4	-580	-29.0	2	-690	-34.5
tv35	V	696	34.8	578	28.9	5	487	24.4	2	379	19.0

Table F-3. Measured strains and approximated stresses from third normal loading cycle, along with numerically predicted stresses at the same position in the physical model.

		Applied normal stress (MPa) and portion of loading cycle (up = loading cycle, dn = unloading)										
		2 up			5 up			8 up			13.4 peak	
gauge label	gauge orient. (H or V)	meas. strain (μE)	approx. stress (MPa)	pred. stress (MPa)	meas. strain (μE)	approx. stress (MPa)	pred stress (MPa)	meas strain (μE)	approx. stress (MPa)	pred stress (MPa)	meas strain (μE)	approx stress (MPa)
th1	H	92	4.6	1.4	144	7.2	3.2	211	10.6	5.0	309	15.4
th2	H	112	5.6	1.4	188	9.4	3.3	251	12.6	5.2	357	17.8
th3	H	115	5.8	1.5	200	10.0	3.5	267	13.4	5.5	362	18.1
th4	H	93	4.6	1.7	163	8.2	3.7	235	11.7	5.9	340	17.0
th5	H	119	5.9	1.7	208	10.4	3.7	289	14.5	5.8	410	20.5
th6	H	132	6.6	1.4	236	11.8	3.3	341	17.0	5.3	436	21.8
th7	H	25	1.3	1.6	93	4.6	3.6	203	10.2	5.6	307	15.3
th8	H	18	0.9	1.6	74	3.7	3.7	145	7.2	5.7	206	10.3
th9	H	-0	-0.0	1.6	77	3.8	3.8	92	4.6	6.0	154	7.7
th10	H	38	1.9	1.6	77	3.8	3.8	116	5.8	6.0	155	7.7
th11	H	76	3.8	1.8	153	7.7	4.1	240	12.0	6.4	381	19.1
th12	H	114	5.7	1.7	191	9.6	4.0	268	13.4	6.3	346	17.3
th13	H	117	5.9	1.9	192	9.6	4.4	207	10.4	6.9	272	13.6
th14	H	-166	-8.3	1.8	-161	-8.1	4.1	-101	-5.0	6.6	-74	-3.7
th15	H	-39	-2.0	1.7	-25	-1.2	4.1	31	1.5	6.5	118	5.9
th16	H	114	5.7	1.8	230	11.5	4.1	308	15.4	6.5	462	23.1
th17	H	37	1.9	1.7	94	4.7	4.1	154	7.7	6.5	306	15.3
th18	H	-104	-5.2	1.6	-50	-2.5	3.7	-98	-4.9	5.9	-32	-1.6
th19	H	81	4.1	1.7	77	3.8	4.0	43	2.1	6.3	30	1.5
th20	H	-1	-0.1	1.4	77	3.8	3.3	155	7.7	5.2	310	15.5
th21	H	38	1.9	1.5	114	5.7	3.4	178	8.9	5.4	232	11.6
th22	H	-15	-0.7	1.4	38	1.9	3.3	105	5.2	5.2	135	6.7
th23	H	20	1.0	1.5	89	4.4	3.5	161	8.0	5.6	207	10.4
th24	H	18	0.9	1.7	116	5.8	3.8	241	12.1	5.9	329	16.5
th25	H	-25	-1.2	1.5	24	1.2	3.4	65	3.2	5.3	84	4.2
th26	H	96	4.8	1.6	236	11.8	3.7	358	17.9	5.8	475	23.7
th27	H	11	0.5	1.4	44	2.2	3.2	79	3.9	5.1	118	5.9
th28	H	-38	-1.9	1.5	-28	-1.4	3.4	23	1.1	5.3	82	4.1
tv1	V	153	7.6	1.8	223	11.2	4.3	325	16.3	6.8	472	23.6
tv2	V	-3	-0.1	1.8	-34	-1.7	4.4	15	0.8	7.0	170	8.5
tv3	V	133	6.6	1.9	79	4.0	4.4	101	5.1	7.0	225	11.3

Table F-3. continued .....

		Applied normal stress (MPa) and portion of loading cycle (up = loading cycle, dn = unloading)										
		2 up			5 up			8 up			13.4 peak	
gauge label	gauge orient. (H or V)	meas. strain (μE)	approx. stress (MPa)	pred. stress (MPa)	meas. strain (μE)	approx. stress (MPa)	pred. stress (MPa)	meas. strain (μE)	approx. stress (MPa)	pred. stress (MPa)	meas. strain (μE)	approx. stress (MPa)
tv4	V	279	14.0	1.7	423	21.1	4.0	538	26.9	6.3	699	35.0
tv5	V	186	9.3	1.8	320	16.0	4.1	384	19.2	6.6	458	22.9
tv6	V	99	5.0	1.8	123	6.2	4.1	118	5.9	6.5	166	8.3
tv7	V	191	9.6	1.7	225	11.3	3.9	215	10.8	6.1	254	12.7
tv8	V	238	11.9	1.6	319	15.9	3.8	332	16.6	6.1	417	20.9
tv9	V	224	11.2	1.6	223	11.2	3.8	171	8.6	6.0	214	10.7
tv10	V	152	7.6	1.6	168	8.4	3.7	214	10.7	5.9	307	15.4
tv11	V	307	15.3	1.8	118	5.9	4.4	105	5.2	7.1	79	4.0
tv12	V	269	13.4	1.7	196	9.8	4.2	108	5.4	6.7	10	0.5
tv13	V	37	1.8	1.6	294	14.7	4.0	311	15.6	6.4	312	15.6
tv14	V	114	5.7	1.7	154	7.7	4.0	149	7.4	6.3	127	6.3
tv15	V	153	7.7	1.6	183	9.2	3.8	128	6.4	6.1	79	3.9
tv16	V	114	5.7	1.6	39	1.9	3.8	-8	-0.4	6.0	-73	-3.7
tv17	V	113	5.6	1.4	228	11.4	3.4	250	12.5	5.4	274	13.7
tv18	V	b/g		1.2	b/g		3.0	b/g		4.7	b/g	
tv19	V	37	1.8	1.6	-14	-0.7	3.7	-36	-1.8	5.9	-71	-3.5
tv20	V	-2	-0.1	1.5	-24	-1.2	3.5	-76	-3.8	5.5	-148	-7.4
tv21	V	-31	-1.6	1.4	-169	-8.4	3.2	-174	-8.7	5.0	-148	-7.4
tv22	V	180	9.0	1.6	265	13.2	3.8	302	15.1	6.0	425	21.2
tv23	V	153	7.7	1.5	193	9.6	3.5	197	9.9	5.6	234	11.7
tv24	V	152	7.6	1.4	236	11.8	3.2	272	13.6	5.0	313	15.7
tv25	V	213	10.7	1.7	276	13.8	4.0	343	17.1	6.4	485	24.2
tv26	V	76	3.8	1.5	193	9.6	3.5	194	9.7	5.6	188	9.4
tv27	V	114	5.7	1.9	193	9.6	4.4	271	13.6	7.1	424	21.2
tv28	V	152	7.6	1.8	308	15.4	4.4	326	16.3	7.0	391	19.5
tv29	V	261	13.1	2	396	19.8	4	335	16.7	7	310	15.5
tv30	V	140	7.0	2	182	9.1	4	279	14.0	6	389	19.4
tv31	V	53	2.7	2	110	5.5	4	187	9.4	6	286	14.3
tv32	V	57	2.9	2	98	4.9	4	213	10.7	6	303	15.2
tv33	V	150	7.5	2	334	16.7	4	424	21.2	6	334	16.7
tv34	V	139	6.9	2	253	12.7	4	285	14.2	7	246	12.3
tv35	V	116	5.8	2	322	16.1	4	585	29.2	7	616	30.6

Table F-3. continued .....

		Applied normal stress (MPa) and portion of loading cycle (up = loading cycle, dn = unloading)									
		8 dn		5 dn			2 dn			0 dn	
gauge label	gauge orient. (H or V)	meas. strain (μE)	approx. stress (MPa)	meas. strain (μE)	approx. stress (MPa)	pred. stress (MPa)	meas. strain (μE)	approx stress (MPa)	pred. stress (MPa)	meas strain (μE)	approx stress (MPa)
th1	H	273	13.6	183	9.4	3.2	113	5.6	1.2	5	0.2
th2	H	308	15.4	197	9.8	3.4	100	5.0	1.3	-5	-0.2
th3	H	328	16.4	237	11.9	3.6	151	7.5	1.5	26	1.3
th4	H	295	14.8	198	9.9	3.9	107	5.4	1.8	-18	-0.9
th5	H	351	17.5	227	11.4	3.8	125	6.2	1.7	23	1.1
th6	H	369	18.4	242	12.1	3.4	126	6.3	1.3	0	0.0
th7	H	283	14.1	201	10.1	3.7	118	5.9	1.5	-16	-0.8
th8	H	199	10.0	156	7.8	3.8	99	5.0	1.7	32	1.6
th9	H	79	3.9	41	2.0	4.0	-36	-1.8	1.8	-75	-3.7
th10	H	79	4.0	41	2.1	3.9	2	0.1	1.6	-54	-2.7
th11	H	270	13.5	194	9.7	4.4	79	3.9	2.1	2	0.1
th12	H	270	13.5	193	9.7	4.1	116	5.8	1.7	2	0.1
th13	H	157	7.9	110	5.5	4.8	-27	-1.4	2.3	-86	-4.3
th14	H	-35	-1.7	17	0.9	4.4	148	7.4	1.9	237	11.9
th15	H	67	3.4	80	4.0	4.3	118	5.9	1.7	121	6.0
th16	H	317	15.9	234	11.7	4.3	118	5.9	1.9	3	0.2
th17	H	167	8.4	110	5.5	4.3	41	2.1	1.7	-32	-1.6
th18	H	-256	-12.8	-385	-19.2	3.9	-556	-27.8	1.8	-662	-33.1
th19	H	-68	-3.4	-111	-5.6	4.1	-150	-7.5	1.7	-260	-13.0
th20	H	158	7.9	44	2.2	3.4	-49	-2.4	1.4	-73	-3.6
th21	H	194	9.7	118	5.9	3.4	47	2.3	1.3	2	0.1
th22	H	95	4.7	25	1.2	3.4	-25	-1.3	1.3	-67	-3.3
th23	H	171	8.6	86	4.3	3.6	9	0.5	1.5	-30	-1.5
th24	H	271	13.6	142	7.1	4.0	36	1.8	1.8	-100	-5.0
th25	H	58	2.9	14	0.7	3.5	-37	-1.9	1.3	-113	-5.6
th26	H	406	20.3	255	12.8	3.9	123	6.1	1.8	-29	-1.4
th27	H	106	5.3	70	3.5	3.3	27	1.4	1.2	-1	-0.0
th28	H	77	3.8	42	2.1	3.5	6	0.3	1.4	9	0.5
tv1	V	454	22.7	355	17.8	4.5	223	11.2	2.0	-24	-1.2
tv2	V	194	9.7	180	9.0	4.6	145	7.2	2.0	24	1.2
tv3	V	262	13.1	241	12.1	4.6	164	8.2	2.1	-3	-0.2

Table F-3. continued .....

		Applied normal stress (MPa) and portion of loading cycle (up = loading cycle, dn = unloading)									
		8 dn		5 dn			2 dn			0 dn	
gauge label	gauge orient. (H or V)	meas. strain (μE)	approx. stress (MPa)	meas. strain (μE)	approx. stress (MPa)	pred. stress (MPa)	meas. strain (μE)	approx. stress (MPa)	pred. stress (MPa)	meas. strain (μE)	approx. stress (MPa)
tv4	V	696	34.8	610	30.5	4.1	469	23.5	1.9	151	7.6
tv5	V	431	21.6	355	17.8	4.3	265	13.3	2.0	61	3.1
tv6	V	164	8.2	132	6.6	4.3	84	4.2	2.0	30	1.5
tv7	V	243	12.2	198	9.9	4.0	129	6.5	1.9	-63	-3.1
tv8	V	403	20.2	326	16.3	4.0	207	10.4	1.8	-80	-4.0
tv9	V	222	11.1	182	9.1	4.0	94	4.7	1.9	-190	-9.5
tv10	V	317	15.9	289	14.5	3.9	237	11.9	1.9	111	5.6
tv11	V	119	6.0	158	7.9	4.6	-36	-1.8	2.1	-208	-10.4
tv12	V	119	5.9	196	9.8	4.4	-74	-3.7	2.0	-347	-17.4
tv13	V	160	8.0	83	4.2	4.1	4	0.2	1.8	-73	-3.6
tv14	V	120	6.0	120	6.0	4.2	80	4.0	1.9	3	0.2
tv15	V	92	4.6	118	5.9	4.0	40	2.0	1.8	-81	-4.1
tv16	V	-34	-1.7	45	2.3	4.0	151	7.5	1.8	118	5.9
tv17	V	200	10.0	163	8.1	3.5	46	2.3	1.6	-111	-5.5
tv18	V	b/g		b/g		3.0	b/g		1.3	b/g	
tv19	V	-69	-3.4	-38	-1.9	4.0	6	0.3	1.9	44	2.2
tv20	V	-184	-9.2	-222	-11.1	3.7	-262	-13.1	1.7	-262	-13.1
tv21	V	-83	-4.1	37	1.8	3.4	120	6.0	1.6	149	7.5
tv22	V	313	15.7	275	13.8	3.9	197	9.8	1.8	78	3.9
tv23	V	197	9.8	158	7.9	3.7	110	5.5	1.7	0	0.0
tv24	V	277	13.8	239	11.9	3.3	195	9.8	1.5	41	2.1
tv25	V	313	15.7	275	13.8	4.2	235	11.8	1.9	116	5.8
tv26	V	190	9.5	196	9.8	3.6	63	3.2	1.6	-150	-7.5
tv27	V	313	15.6	236	11.8	4.6	158	7.9	2.1	42	2.1
tv28	V	355	17.7	279	13.9	4.5	122	6.1	2.0	3	0.2
tv29	V	311	15.6	364	18.2	4	195	9.8	2	-76	-3.8
tv30	V	405	20.2	360	18.0	4	278	13.9	2	66	3.3
tv31	V	302	15.1	272	13.6	4	214	10.7	2	62	3.1
tv32	V	306	15.3	267	13.3	4	215	10.3	2	63	3.2
tv33	V	192	9.6	9	0.5	4	-141	-7.1	2	-336	-16.8
tv34	V	174	8.7	30	1.5	4	-128	-6.4	2	-363	-18.2
tv35	V	504	25.2	336	16.8	5	184	9.4	2	18	0.9

Table F-4. Measured strains and approximated stresses from first shear loading cycle, along with numerically predicted stresses at the same position in the physical model.

		Applied shear stress (MPa) and portion of loading cycle (up = loading cycle, dn = unloading)												
		0 up		0.25 up		0.5 up			0.75 up		0.84 up	1.0 up		
gauge label	gauge orient (H or V)	meas strain (μE)	approx stress (MPa)	meas strain (μE)	approx. stress (MPa)	meas strain (μE)	approx stress (MPa)	pred stress (MPa)	meas strain (μE)	approx stress (MPa)	pred stress (MPa)	meas strain (μE)	approx stress (MPa)	pred stress (MPa)
th1	H	7	0.3	41	2.1	69	3.4	1.6	78	3.9	1.7	80	4.0	2.1
th2	H	58	2.9	84	4.2	108	5.4	1.7	123	6.2	1.9	128	6.4	2.7
th3	H	29	1.4	29	1.4	41	2.0	1.7	55	2.7	1.7	70	3.5	2.8
th4	H	42	2.1	48	2.4	69	3.4	1.9	96	4.8	1.7	119	6.0	1.6
th5	H	12	0.6	28	1.4	59	2.9	1.5	86	4.3	1.6	105	5.3	4.6
th6	H	8	0.4	20	1.0	35	1.7	1.6	43	2.2	1.8	42	2.1	2.2
th7	H	68	3.4	79	3.9	86	4.3	1.8	86	4.3	2.3	76	3.8	4.1
th8	H	48	2.4	66	3.3	78	3.9	1.9	90	4.5	2.7	103	5.2	6.5
th9	H	7	0.3	0	0.0	2	0.1	1.4	0	0.0	1.5	1	0.0	0.7
th10	H	30	1.5	19	0.9	37	1.8	1.5	39	1.9	1.5	37	1.9	1.5
th11	H	77	3.9	77	3.8	77	3.8	1.7	77	3.9	1.6	77	3.9	0.7
th12	H	115	5.8	115	5.8	115	5.7	1.7	125	6.3	1.7	153	7.7	1.9
th13	H	80	4.0	39	1.9	39	1.9	1.8	39	2.0	1.5	39	2.0	1.5
th14	H	-196	-9.8	-154	-7.7	-115	-5.8	1.8	-82	-4.1	1.9	-76	-3.8	2.2
th15	H	-38	-1.9	0	0.0	37	1.8	1.8	39	2.0	1.8	78	3.9	2.0
th16	H	78	3.9	77	3.9	77	3.8	1.7	77	3.9	1.4	39	2.0	1.7
th17	H	30	1.5	1	0.0	0	0.0	1.7	-17	-0.9	1.5	-37	-1.9	1.3
th18	H	-152	-7.6	-195	-9.8	-232	-11.6	1.8	-268	-13.4	2.4	-342	-17.1	5.7
th19	H	39	2.0	9	0.4	0	0.0	1.7	-38	-1.9	1.5	-48	-2.4	1.7
th20	H	2	0.1	1	0.0	1	0.0	1.5	-30	-1.5	1.7	-37	-1.9	3.1
th21	H	1	0.0	0	0.0	0	0.0	1.6	1	0.0	1.8	-35	-1.7	2.5
th22	H	43	2.2	52	2.6	54	2.7	1.3	49	2.5	1.0	49	2.4	0.3
th23	H	58	2.9	88	4.4	98	4.9	1.4	87	4.3	1.4	52	2.6	1.3
th24	H	28	1.4	37	1.9	44	2.2	2.3	45	2.2	4.7	26	1.3	10.8
th25	H	58	2.9	63	3.1	59	2.9	1.3	53	2.7	1.1	50	2.5	0.6
th26	H	86	4.3	106	5.3	99	4.9	1.5	79	4.0	1.1	61	3.1	1.6
th27	H	22	1.1	37	1.8	44	2.2	1.2	49	2.4	1.3	54	2.7	0.8
th28	H	-4	-0.2	3	0.2	6	0.3	1.2	-2	-0.1	1.2	-19	-0.9	0.2
tv1	V	119	5.9	147	7.3	164	8.2	1.8	175	8.7	1.6	189	9.5	0.6
tv2	V	36	1.8	59	3.0	82	4.1	2.0	98	4.9	1.7	102	5.1	0.2
tv3	V	124	6.2	149	7.4	178	8.9	2.0	200	10.0	1.8	202	10.1	-0.0

Table F-4. continued .....

		Applied shear stress (MPa) and portion of loading cycle (up = loading cycle, dn = unloading)												
		0 up		0.25 up		0.5 up			0.75 up		0.84 up	1.0 up		
gauge label	gauge orient. (H or V)	meas. strain (μE)	approx. stress (MPa)	meas. strain (μE)	approx. stress (MPa)	meas. strain (μE)	approx. stress (MPa)	pred. stress (MPa)	meas. strain (μE)	approx. stress (MPa)	pred. stress (MPa)	meas. strain (μE)	approx. stress (MPa)	pred. stress (MPa)
tv4	V	187	9.4	221	11.0	243	12.1	1.5	257	12.8	1.2	261	13.1	1.7
tv5	V	104	5.2	125	6.2	147	7.3	1.7	155	7.7	1.3	141	7.1	0.7
tv6	V	18	0.9	18	0.9	29	1.5	2.0	47	2.3	1.5	66	3.3	0.2
tv7	V	73	3.6	72	3.6	82	4.1	0.7	97	4.8	0.2	118	5.9	0.5
tv8	V	133	6.7	125	6.2	118	5.9	1.5	113	5.6	1.7	97	4.9	3.5
tv9	V	82	4.1	35	1.8	27	1.4	1.4	21	1.1	1.4	11	0.6	3.2
tv10	V	39	1.9	48	2.4	70	3.5	1.8	84	4.2	1.4	91	4.5	3.6
tv11	V	369	18.4	347	17.4	347	17.3	1.9	365	18.3	1.7	386	19.3	0.1
tv12	V	393	19.7	385	19.3	385	19.3	1.7	391	19.5	1.5	408	20.4	0.2
tv13	V	67	3.4	76	3.8	77	3.9	1.5	96	4.8	1.3	117	5.8	0.5
tv14	V	117	5.8	116	5.8	116	5.8	1.6	116	5.8	1.3	116	5.8	0.1
tv15	V	122	6.1	116	5.8	116	5.8	1.5	101	5.0	1.2	77	3.9	0.1
tv16	V	78	3.9	77	3.9	112	5.6	1.0	116	5.8	0.6	133	6.7	0.0
tv17	V	87	4.3	78	3.9	78	3.9	1.2	43	2.1	1.1	40	2.0	0.6
tv19	V	2	0.1	1	0.1	1	0.0	1.1	2	0.1	1.1	2	0.1	1.0
tv18	V	b/g		b/g		b/g		1.7	b/g		1.5	b/g		3.2
tv20	V	-57	-2.8	-75	-3.8	-76	-3.8	1.3	-75	-3.8	1.1	-75	-3.7	1.7
tv21	V	-113	-5.6	-71	-3.6	-17	-0.9	1.2	1	0.1	1.2	40	2.0	1.8
tv22	V	162	8.1	155	7.7	154	7.7	2.3	155	7.7	4.6	116	5.8	10.2
tv23	V	155	7.8	155	7.7	154	7.7	1.9	116	5.8	3.1	116	5.8	7.1
tv24	V	191	9.5	194	9.7	193	9.7	1.5	194	9.7	2.2	194	9.7	4.8
tv25	V	194	9.7	193	9.7	193	9.6	1.8	193	9.7	2.0	193	9.7	3.6
tv26	V	117	5.9	106	5.3	77	3.9	1.7	78	3.9	2.5	78	3.9	5.4
tv27	V	79	3.9	78	3.9	77	3.9	1.8	78	3.9	1.0	78	3.9	0.6
tv28	V	193	9.7	180	9.0	155	7.7	1.9	155	7.8	1.7	156	7.8	1.9
tv29	V	231	11.6	230	11.5	221	11.1	1.9	192	9.6	1.9	192	9.6	2.6
tv30	V	167	8.3	197	9.9	218	10.9	1.8	234	11.7	2.8	242	12.1	5.5
tv31	V	112	5.6	149	7.5	173	8.6	2.1	194	9.7	3.9	230	11.5	8.5
tv32	V	98	4.9	142	7.1	168	8.4	2.5	176	8.8	5.7	175	8.7	11.7
tv33	V	151	7.5	191	9.5	212	10.6	1.6	225	11.2	1.7	231	11.5	2.0
tv34	V	180	9.0	212	10.6	225	11.2	1.8	236	11.8	1.6	243	12.1	1.6
tv35	V	97	4.8	109	5.5	121	6.1	1.8	132	6.6	1.2	131	6.6	0.3

Table F-4. continued .....

		Applied shear stress (MPa) and portion of loading cycle (up = loading cycle, dn = unloading)													
		1.23 MPa peak		1.50 up	1.0 dn		0.75 dn		0.5 dn		0.25 dn		0 dn	
gauge label	gauge orient. (H or V)	meas. strain (μE)	approx. stress (MPa)	pred. stress (MPa)	pred. stress (MPa)	meas. strain (μE)	approx. stress (MPa)	meas. strain (μE)	approx. stress (MPa)	meas. strain (μE)	approx. stress (MPa)	meas strain (μE)	approx stress (MPa)	meas strain (μE)	approx stress (MPa)
th1	H	39	2.0	3.0	3.5	13	0.7	10	0.5	7	0.3	2	0.1	-6	-0.3
th2	H	86	4.3	3.3	3.6	54	2.7	60	3.0	68	3.4	72	3.6	69	3.4
th3	H	17	0.9	4.6	5.5	-10	-0.5	-14	-0.7	-15	-0.8	-15	-0.8	-16	-0.8
th4	H	72	3.6	2.8	3.5	64	3.2	64	3.2	63	3.1	59	2.9	50	2.5
th5	H	90	4.5	8.8	10.3	89	4.5	83	4.2	73	3.7	63	3.2	49	2.4
th6	H	30	1.5	1.9	1.9	29	1.4	34	1.7	39	1.9	38	1.9	31	1.6
th7	H	24	1.2	4.5	4.4	10	0.5	16	0.8	20	1.0	18	0.9	10	0.5
th8	H	85	4.3	8.8	8.3	51	2.5	47	2.3	44	2.2	41	2.1	33	1.7
th9	H	1	0.1	-0.2	-0.5	4	0.2	4	0.2	1	0.0	1	0.1	2	0.1
th10	H	40	2.0	1.2	1.0	39	2.0	39	2.0	39	2.0	40	2.0	21	1.1
th11	H	116	5.8	-0.1	-0.8	116	5.8	116	5.8	116	5.8	116	5.8	117	5.8
th12	H	154	7.7	1.8	1.7	154	7.7	154	7.7	154	7.7	154	7.7	155	7.7
th13	H	79	3.9	0.4	-0.6	78	3.9	78	3.9	40	2.0	40	2.0	41	2.1
th14	H	-23	-1.2	2.3	2.2	-38	-1.9	-37	-1.9	-37	-1.8	-75	-3.7	-74	-3.7
th15	H	117	5.9	1.7	1.6	116	5.8	100	5.0	78	3.9	79	3.9	49	2.5
th16	H	2	0.1	2.7	2.7	1	0.1	1	0.1	2	0.1	2	0.1	3	0.2
th17	H	-36	-1.8	1.2	1.1	-37	-1.9	-37	-1.9	-37	-1.8	-36	-1.8	-35	-1.8
th18	H	-553	-27.7	6.3	6.9	-597	-29.9	-609	-30.4	-607	-30.4	-632	-31.6	-641	-32.0
th19	H	-75	-3.8	2.6	2.7	-76	-3.8	-76	-3.8	-75	-3.8	-75	-3.7	-74	-3.7
th20	H	-36	-1.8	3.7	4.0	-37	-1.8	-37	-1.8	-36	-1.8	3	0.1	4	0.2
th21	H	-37	-1.8	3.3	3.5	-37	-1.9	-37	-1.9	-6	-0.3	2	0.1	2	0.1
th22	H	72	3.6	0.4	0.4	75	3.8	69	3.4	63	3.1	57	2.9	47	2.4
th23	H	3	0.1	0.3	0.3	21	1.1	29	1.5	33	1.6	32	1.6	27	1.4
th24	H	-45	-2.3	3.0	1.4	-44	-2.2	-43	-2.2	-44	-2.2	-49	-2.5	-61	-3.0
th25	H	42	2.1	0.9	0.8	46	2.3	47	2.4	48	2.4	48	2.4	45	2.2
th26	H	25	1.2	-0.0	-0.3	22	1.1	22	1.1	21	1.1	20	1.0	15	0.8
th27	H	3	0.1	0.6	0.3	-9	-0.5	-1	-0.0	10	0.5	17	0.8	17	0.9
th28	H	-57	-2.9	-0.4	-1.0	-64	-3.2	-65	-3.3	-66	-3.3	-65	-3.3	-65	-3.3
tv1	V	111	5.6	1.1	1.4	74	3.7	68	3.4	59	3.0	50	2.5	35	1.8
tv2	V	-8	-0.4	0.4	0.5	-58	-2.9	-62	-3.1	-61	-3.0	-57	-2.9	-55	-2.8
tv3	V	46	2.3	0.0	0.0	-13	-0.7	-24	-1.2	-35	-1.7	-45	-2.3	-62	-3.1

Table F-4. continued .....

		Applied shear stress (MPa) and portion of loading cycle (up = loading cycle, dn = unloading)													
		1.23 MPa peak			1.50 up	1.0 dn		0.75 dn		0.5 dn		0.25 dn		0 dn	
gauge label	gauge orient. (H or V)	meas. strain (μE)	approx. stress (MPa)	pred. stress (MPa)	pred. stress (MPa)	meas. strain (μE)	approx. stress (MPa)	meas. strain (μE)	approx. stress (MPa)	meas. strain (μE)	approx. stress (MPa)	meas. strain (μE)	approx. stress (MPa)	meas. strain (μE)	approx. stress (MPa)
tv4	V	167	8.3	3.3	3.8	141	7.0	138	6.9	134	6.7	125	6.3	105	5.2
tv5	V	63	3.1	1.4	1.6	51	2.5	51	2.6	49	2.5	44	2.2	34	1.7
tv6	V	22	1.1	0.2	0.3	-6	-0.3	-7	-0.4	-7	-0.4	-7	-0.4	-9	-0.5
tv7	V	46	2.3	1.4	1.0	9	0.4	3	0.2	-2	-0.1	-8	-0.4	-23	-1.1
tv8	V	-34	-1.7	6.0	6.5	-74	-3.7	-78	-3.9	-81	-4.0	-86	-4.3	-100	-5.0
tv9	V	-101	-5.1	7.2	8.1	-146	-7.3	-148	-7.4	-148	-7.4	-150	-7.5	-158	-7.9
tv10	V	50	2.5	9.9	9.7	8	0.4	2	0.1	-3	-0.2	-7	-0.4	-14	-0.7
tv11	V	310	15.5	-0.1	-0.0	309	15.4	309	15.5	306	15.3	275	13.8	273	13.6
tv12	V	271	13.6	-0.2	-0.1	270	13.5	271	13.5	248	12.4	233	11.6	234	11.7
tv13	V	80	4.0	0.1	0.1	79	3.9	79	3.9	79	4.0	80	4.0	54	2.7
tv14	V	79	4.0	0.0	0.1	78	3.9	78	3.9	67	3.4	45	2.2	42	2.1
tv15	V	2	0.1	-0.0	-0.0	39	2.0	39	2.0	40	2.0	40	2.0	46	2.3
tv16	V	21	1.0	-0.0	-0.3	1	0.1	1	0.1	2	0.1	3	0.1	-26	-1.3
tv17	V	5	0.2	0.9	0.9	3	0.1	3	0.1	4	0.2	5	0.3	7	0.4
tv19	V	-47	-2.4	1.5	1.5	-55	-2.8	-64	-3.2	-73	-3.7	-72	-3.6	-70	-3.5
tv18	V	b/g		7.4	7.0	b/g		b/g		b/g		b/g		b/g	
tv20	V	-154	-7.7	3.5	3.5	-189	-9.5	-189	-9.4	-192	-9.6	-225	-11.3	-223	-11.2
tv21	V	4	0.2	3.1	3.2	2	0.1	2	0.1	3	0.1	4	0.2	-27	-1.4
tv22	V	-36	-1.8	8.9	8.8	-37	-1.9	-37	-1.9	-36	-1.8	-36	-1.8	-34	-1.7
tv23	V	40	2.0	8.8	9.0	39	2.0	20	1.0	2	0.1	2	0.1	3	0.2
tv24	V	124	6.2	6.8	6.8	117	5.9	118	5.9	119	5.9	120	6.0	122	6.1
tv25	V	79	4.0	0.7	0.6	78	3.9	78	3.9	79	4.0	80	4.0	81	4.1
tv26	V	2	0.1	5.8	6.1	1	0.1	1	0.1	2	0.1	3	0.1	4	0.2
tv27	V	41	2.0	-0.0	0.1	40	2.0	40	2.0	40	2.0	41	2.1	42	2.1
tv28	V	84	4.2	1.2	1.3	83	4.1	86	4.3	84	4.2	109	5.4	109	5.4
tv29	V	117	5.9	2.1	2.2	116	5.8	116	5.8	117	5.9	118	5.9	119	5.9
tv30	V	145	7.3	5.2	4.8	111	5.5	110	5.5	107	5.4	99	5.0	79	4.0
tv31	V	227	11.3	7.8	7.1	185	9.3	182	9.1	180	9.0	175	8.7	156	7.8
tv32	V	90	4.5	1.6	-1.3	64	3.2	65	3.2	67	3.3	66	3.3	58	2.9
tv33	V	182	9.1	1.3	1.1	179	8.9	180	9.0	174	8.7	163	8.1	137	6.8
tv34	V	196	9.8	0.6	0.3	207	10.4	207	10.4	202	10.1	191	9.5	166	8.3
tv35	V	75	3.8	-0.1	-0.1	41	2.1	35	1.8	28	1.4	21	1.1	9	0.5

Table F-5. Measured strains and approximated stresses from second shear loading cycle, along with numerically predicted stresses at the same position in the physical model.

		Applied shear stress (MPa) and portion of loading cycle (up = loading cycle, dn = unloading)										
		0 up		2 up			3 up			3.7 up	4 up	
gauge label	gauge orient. (H or V)	meas. strain (μE)	approx. stress (MPa)	meas. strain (μE)	approx stress (MPa)	pred. stress (MPa)	meas. strain (μE)	approx stress (MPa)	pred stress (MPa)	pred stress (MPa)	meas strain (μE)	approx stress (MPa)
th1	H	244	12.2	221	11.1	5.8	185	9.3	6.1	6.2	182	9.1
th2	H	301	15.1	252	12.6	5.8	214	10.7	6.2	6.7	337	16.8
th3	H	307	15.3	311	15.5	6.2	272	13.6	6.1	6.1	278	13.9
th4	H	327	16.3	381	19.0	6.4	376	18.8	6.8	6.6	375	18.8
th5	H	444	22.2	504	25.2	5.9	459	22.9	5.4	5.1	408	20.4
th6	H	367	18.3	388	19.4	5.6	367	18.4	5.9	6.3	462	23.1
th7	H	416	20.8	326	16.3	5.9	357	17.9	6.4	7.4	428	21.4
th8	H	369	18.5	283	14.1	5.6	345	17.3	7.1	8.5	453	22.7
th9	H	117	5.9	120	6.0	6.0	113	5.6	5.8	5.9	137	6.9
th10	H	121	6.0	123	6.2	5.9	120	6.0	5.8	5.8	140	7.0
th11	H	269	13.5	261	13.0	6.6	238	11.9	6.4	6.3	282	14.1
th12	H	304	15.2	322	16.1	6.3	323	16.1	6.2	6.3	359	18.0
th13	H	148	7.4	135	6.8	7.2	116	5.8	6.2	5.6	190	9.5
th14	H	12	0.6	26	1.3	6.7	12	0.6	6.7	7.0	104	5.2
th15	H	109	5.5	112	5.6	6.6	78	3.9	6.6	6.8	125	6.2
th16	H	307	15.4	306	15.3	6.6	310	15.5	6.3	5.7	265	13.2
th17	H	101	5.0	84	4.2	6.7	88	4.4	6.5	6.1	89	4.4
th18	H	210	10.5	217	10.8	6.1	222	11.1	6.7	7.9	226	11.3
th19	H	178	8.9	142	7.1	6.6	104	5.2	6.4	6.1	36	1.8
th20	H	188	9.4	178	8.9	5.5	171	8.6	5.7	6.2	159	8.0
th21	H	205	10.2	177	8.8	5.9	158	7.9	6.1	6.4	128	6.4
th22	H	151	7.6	115	5.7	4.9	94	4.7	4.6	4.1	-107	-5.3
th23	H	250	12.5	185	9.2	5.3	189	9.5	5.2	5.0	159	7.9
th24	H	309	15.5	338	16.9	6.3	368	18.4	8.2	13.4	374	18.7
th25	H	282	14.1	197	9.8	4.9	177	8.9	4.6	4.4	135	6.7
th26	H	461	23.1	328	16.4	5.5	415	20.7	5.2	4.1	389	19.4
th27	H	126	6.3	68	3.4	4.4	122	6.1	4.2	4.3	111	5.5
th28	H	135	6.7	101	5.0	4.6	115	5.7	4.3	4.3	129	6.5
tv1	V	640	32.0	614	30.7	7.0	564	28.2	7.1	6.8	602	30.1
tv2	V	239	12.0	289	14.4	7.1	245	12.3	7.5	7.2	227	11.4
tv3	V	516	25.8	516	25.8	7.2	477	23.9	7.5	7.4	452	22.6

Table F-5. continued .....

		Applied shear stress (MPa) and portion of loading cycle (up = loading cycle, dn = unloading)											
		0 up		2 up			3 up			3.7 up		4 up	
gauge label	gauge orient. (H or V)	meas. strain (μE)	approx. stress (MPa)	meas. strain (μE)	approx. stress (MPa)	pred. stress (MPa)	meas. strain (μE)	approx. stress (MPa)	pred. stress (MPa)	pred. stress (MPa)	meas. strain (μE)	approx. stress (MPa)
tv4	V	673	33.7	759	37.9	6.3	751	37.6	5.6	5.1	817	40.8
tv5	V	362	18.1	435	21.7	6.7	342	17.1	6.5	5.8	320	16.0
tv6	V	81	4.0	95	4.8	6.7	49	2.4	7.6	6.9	124	6.2
tv7	V	198	9.9	242	12.1	5.6	217	10.8	2.8	1.5	317	15.8
tv8	V	543	27.1	600	30.0	6.0	582	29.1	5.7	5.9	612	30.6
tv9	V	250	12.5	253	12.7	5.9	212	10.6	5.4	5.1	296	14.8
tv10	V	230	11.5	233	11.7	6.0	243	12.1	6.7	5.6	282	14.1
tv11	V	345	17.3	321	16.0	7.1	304	15.2	7.5	7.4	285	14.3
tv12	V	557	27.9	506	25.3	6.6	458	22.9	6.7	6.5	405	20.2
tv13	V	198	9.9	223	11.1	6.0	237	11.8	5.8	5.5	247	12.3
tv14	V	52	2.6	42	2.1	6.2	38	1.9	6.4	6.0	53	2.7
tv15	V	98	4.9	66	3.3	6.0	40	2.0	5.8	5.4	30	1.5
tv16	V	-110	-5.5	-119	-6.0	5.6	-134	-6.7	3.9	3.0	-138	-6.9
tv17	V	105	5.3	75	3.7	5.3	73	3.6	4.8	4.5	83	4.2
tv18	V	b/g		b/g		4.6	b/g		4.3	4.2	b/g	
tv19	V	-104	-5.2	-84	-4.2	6.1	-72	-3.6	6.1	5.3	-83	-4.1
tv20	V	-43	-2.1	-34	-1.7	5.5	-37	-1.8	4.7	4.2	-33	-1.6
tv21	V	-184	-9.2	-175	-8.7	5.0	-193	-9.6	4.6	4.5	-196	-9.8
tv22	V	227	11.3	240	12.0	6.6	233	11.7	8.3	13.1	225	11.2
tv23	V	155	7.7	150	7.5	6.0	131	6.5	7.0	9.5	104	5.2
tv24	V	268	13.4	273	13.6	5.3	278	13.9	5.7	6.9	306	15.3
tv25	V	208	10.4	214	10.7	6.7	211	10.5	7.0	7.0	198	9.9
tv26	V	154	7.7	137	6.9	5.9	134	6.7	6.6	8.2	122	6.1
tv27	V	301	15.0	291	14.6	7.3	28[illegible]	14.0	7.1	5.7	268	13.4
tv28	V	359	18.0	368	18.4	7.3	373	18.6	7.4	7.[illegible]	365	18.2
tv29	V	444	22.2	507	25.3	7.1	553	27.[illegible]	7.4	7.5	553	27.6
tv30	V	496	24.8	427	21.4	6.3	489	24.5	7.0	8.6	565	28.2
tv31	V	332	16.6	324	16.2	6.5	409	20.4	8.9	11.5	592	29.6
tv32	V	319	16.0	343	17.1	6.9	392	19.6	9.1	15.8	529	26.9
tv33	V	708	35.4	683	34.1	6.2	722	36.1	6.3	6.5	760	38.0
tv34	V	490	24.5	408	20.4	6.8	415	20.8	6.8	6.7	371	18.5
tv35	V	412	20.6	460	23.0	7.1	471	23.5	6.9	6.1	445	22.3

Table F-5. continued .....

		Applied shear stress (MPa) and portion of loading cycle (up = loading cycle, dn = unlo							
		4.2 up	4.6 up	5 up		7 up		7.8 peak	
gauge label	gauge orient. (H or V)	pred. stress (MPa)	pred. stress (MPa)	meas. strain (μE)	approx stress (MPa)	meas strain (μE)	approx. stress (MPa)	meas. strain (μE)	approx stress (MPa)
th1	H	6.5	9.4	150	7.5	182	9.1	135	6.8
th2	H	7.8	11.4	227	11.4	190	9.5	139	6.9
th3	H	6.5	13.1	241	12.0	209	10.4	155	7.7
th4	H	4.1	7.4	267	13.4	230	11.5	134	6.7
th5	H	8.0	23.0	369	18.5	319	15.9	302	15.1
th6	H	6.8	8.4	359	17.9	181	9.0	106	5.3
th7	H	9.9	17.3	490	24.5	440	22.0	772	38.6
th8	H	14.2	30.8	619	31.0	954	47.7	1786	89.3
th9	H	6.1	0.9	152	7.6	151	7.6	113	5.7
th10	H	6.6	4.8	159	7.9	158	7.9	154	7.7
th11	H	6.0	0.6	334	16.7	490	24.5	662	33.1
th12	H	7.2	6.8	400	20.0	503	25.1	606	30.3
th13	H	6.3	2.9	297	14.8	700	35.0	1197	59.8
th14	H	8.2	7.7	160	8.0	248	12.4	402	20.1
th15	H	7.4	7.0	185	9.2	365	18.2	550	27.5
th16	H	5.4	6.4	186	9.3	132	6.6	64	3.2
th17	H	5.4	4.3	118	5.9	120	6.0	79	3.9
th18	H	12.6	23.7	228	11.4	133	6.6	82	4.1
th19	H	5.7	6.8	-27	-1.3	-100	-5.0	-115	-5.7
th20	H	8.1	13.2	134	6.7	33	1.7	23	1.1
th21	H	7.7	10.6	100	5.0	46	2.3	54	2.7
th22	H	2.5	0.6	-190	-9.5	-16	-0.8	181	9.1
th23	H	4.7	2.8	243	12.1	132	6.6	-348	-17.4
th24	H	27.1	40.0	254	12.7	72	3.6	203	10.1
th25	H	3.2	2.0	206	10.3	-302	-15.1	-744	-37.2
th26	H	4.4	2.7	253	12.7	470	23.5	1160	58.0
th27	H	4.5	2.1	42	2.1	-3	-0.1	88	4.4
th28	H	4.0	-1.7	186	9.3	225	11.2	414	20.7
tv1	V	4.6	3.0	662	33.1	706	35.3	679	34.0
tv2	V	4.4	0.9	146	7.3	266	13.3	294	14.7
tv3	V	5.1	0.1	353	17.6	384	19.2	469	23.4

Table F-5. continued .....

		Applied shear stress (MPa) and portion of loading cycle (up = loading cycle, dn = unlo							
		4.2 up	4.6 up	5 up		7 up		7.8 peak	
gauge label	gauge orient. (H or V)	pred. stress (MPa)	pred. stress (MPa)	meas. strain (μE)	approx. stress (MPa)	meas. strain (μE)	approx. stress (MPa)	meas. strain (μE)	approx. stress (MPa)
tv4	V	4.4	8.6	761	38.0	785	39.3	621	31.1
tv5	V	2.6	3.3	322	16.1	434	21.7	469	23.4
tv6	V	2.2	0.6	135	6.7	312	15.6	465	23.3
tv7	V	0.9	2.9	428	21.4	560	28.0	595	29.7
tv8	V	8.3	16.7	586	29.3	602	30.1	625	31.2
tv9	V	7.2	16.8	333	16.7	506	25.3	799	40.0
tv10	V	7.8	19.8	318	15.9	681	34.0	1193	59.7
tv11	V	5.6	0.1	280	14.0	302	15.1	349	17.4
tv12	V	4.9	0.6	377	18.8	368	18.4	438	21.9
tv13	V	4.5	1.6	240	12.0	181	9.0	143	7.2
tv14	V	3.0	0.3	63	3.2	96	4.8	170	8.5
tv15	V	3.5	0.5	9	0.5	24	1.2	67	3.3
tv16	V	1.1	0.1	-148	-7.4	-126	-6.3	-68	-3.4
tv17	V	3.8	2.7	87	4.3	42	2.1	36	1.8
tv18	V	4.4	4.5	b/g		b/g		b/g	
tv19	V	7.5	15.7	-102	-5.1	-226	-11.3	-519	-26.0
tv20	V	5.1	8.0	-28	-1.4	-34	-1.7	-45	-2.2
tv21	V	5.6	8.0	-229	-11.5	-369	-18.4	-429	-21.5
tv22	V	26.7	40.0	303	15.1	-61	-3.0	-60	-3.0
tv23	V	17.8	30.3	118	5.9	101	5.1	60	3.0
tv24	V	12.0	20.8	287	14.3	81	4.0	47	2.4
tv25	V	10.3	11.2	165	8.3	102	5.1	80	4.0
tv26	V	13.8	22.2	104	5.2	41	2.0	3	0.2
tv27	V	1.8	1.7	254	12.7	222	11.1	216	10.8
tv28	V	5.8	7.2	349	17.5	281	14.1	247	12.0
tv29	V	7.9	10.0	524	26.2	312	15.6	164	8.2
tv30	V	14.8	22.0	654	32.7	477	23.8	138	6.9
tv31	V	21.7	34.9	877	43.8	1087	54.4	875	43.8
tv32	V	32.7	38.2	658	32.9	592	29.6	686	34.3
tv33	V	7.3	6.8	791	39.6	524	26.2	675	33.8
tv34	V	6.3	4.3	315	15.8	285	14.2	433	21.7
tv35	V	2.6	-0.1	482	24.1	429	21.4	466	23.3

Table F-6. Measured strains and approximated stresses from third shear loading cycle. No numerical simulation of this step was conducted, so no predicted stresses are available.

		Applied shear stress (MPa) and portion of loading cycle (up = loading cycle, dn = unloading)													
		1.00 up		3.00 up		3.75 up		6.00 up		7.00 up		8.00 up		8.50 up	
gauge label	gauge orient. (H or V)	meas. strain (μE)	approx. stress (MPa)	meas. strain (μE)	approx. stress (MPa)	meas. strain (μE)	approx. stress (MPa)	meas strain (μE)	approx. stress (MPa)	meas strain (μE)	approx stress (MPa)	meas strain (μE)	approx stress (MPa)	meas. strain (μE)	approx stress (MPa)
th1	H			b/g		b/g		b/g		b/g		b/g		b/g	
th2	H	224	11.2	192	9.6	170	8.5	108	5.4	74	3.7	40	2.0	18	0.9
th3	H	173	8.7	166	8.3	159	8.0	142	7.1	146	7.3	145	7.2	145	7.2
th4	H	185	9.3	169	8.4	157	7.8	132	6.6	136	6.8	133	6.7	130	6.5
th5	H	291	14.5	278	13.9	263	13.2	224	11.2	223	11.1	225	11.3	222	11.1
th6	H	638	31.9	623	31.2	589	29.5	474	23.7	389	19.4	255	12.8	207	10.3
th7	H	489	24.5	496	24.8	479	24.0	406	20.3	346	17.3	203	10.2	137	6.8
th8	H	355	17.8	404	20.2	431	21.5	506	25.3	589	29.5	807	40.3	866	43.3
th9	H	182	9.1	166	8.3	150	7.5	117	5.8	114	5.7	115	5.7	121	6.1
th10	H	183	9.2	174	8.7	163	8.2	143	7.1	141	7.1	147	7.3	148	7.4
th11	H	462	23.1	460	23.0	449	22.5	430	21.5	465	23.3	568	28.4	612	30.6
th12	H	432	21.6	447	22.3	449	22.4	468	23.4	499	25.0	578	28.9	607	30.4
th13	H	277	13.9	311	15.6	320	16.0	408	20.4	529	26.4	765	38.3	845	42.2
th14	H	-76	-3.8	-52	-2.6	-43	-2.2	-15	-0.7	85	4.3	233	11.7	283	14.1
th15	H	185	9.2	169	8.4	135	6.8	100	5.0	201	10.0	341	17.1	398	19.9
th16	H	238	11.9	246	12.3	250	12.5	207	10.3	136	6.8	105	5.2	93	4.6
th17	H	208	10.4	189	9.4	184	9.2	182	9.1	173	8.6	167	8.3	146	7.3
th18	H	322	16.1	306	15.3	294	14.7	244	12.2	162	8.1	127	6.4	110	5.5
th19	H	282	14.1	212	10.6	180	9.0	74	3.7	2	0.1	-22	-1.1	-50	-2.5
th20	H	445	22.3	394	19.7	364	18.2	251	12.6	126	6.3	-30	-1.5	-79	-3.9
th21	H	89	4.4	71	3.6	75	3.8	50	2.5	38	1.9	54	2.7	61	3.0
th22	H	523	26.2	502	25.1	485	24.3	359	17.9	310	15.5	347	17.3	335	16.7
th23	H	452	22.6	399	19.9	341	17.0	111	5.5	-130	-6.5	b/g		b/g	
th24	H	194	9.7	258	12.9	317	15.9	472	23.6	732	36.6	395	19.7	388	19.4
th25	H	773	38.7	673	33.7	539	27.0	-229	-11.5	b/g		b/g		b/g	
th26	H	32	1.6	-81	-4.1	-152	-7.6	-465	-23.2	-604	-30.2	-742	-37.1	-582	-29.1
th27	H	-154	-7.7	-159	-7.9	-172	-8.6	-194	-9.7	-211	-10.5	-233	-11.6	-240	-12.0
th28	H	-42	-2.1	-41	-2.1	-52	-2.6	-61	-3.1	-62	-3.1	-97	-4.9	-105	-5.3
tv1	V	244	12.2	234	11.7	241	12.1	209	10.4	192	9.6	202	10.1	202	10.1
tv2	V	-201	-10.1	-235	-11.8	-244	-12.2	-266	-13.3	-271	-13.5	-267	-13.4	-268	-13.4
tv3	V	371	18.5	321	16.1	278	13.9	222	11.1	270	13.5	315	15.7	339	16.9

Table F-6. continued .....

		Applied shear stress (MPa) and portion of loading cycle (up = loading cycle, dn = unloading)													
		1.00 up		3.00 up		3.75 up		6.00 up		7.00 up		8.00 up		8.50 up	
gauge label	gauge orient. (H or V)	meas. strain (μE)	approx. stress (MPa)	meas. strain (μE)	approx. stress (MPa)	meas. strain (μE)	approx. stress (MPa)	meas. strain (μE)	approx. stress (MPa)	meas. strain (μE)	approx. stress (MPa)	meas. strain (μE)	approx. stress (MPa)	meas. strain (μE)	approx. stress (MPa)
tv4	V	326	16.3	315	15.7	313	15.7	289	14.4	268	13.4	251	12.5	236	11.8
tv5	V	504	25.2	491	24.6	490	24.5	471	23.5	472	23.6	484	24.2	486	24.3
tv6	V	34	1.7	28	1.4	35	1.7	53	2.6	67	3.4	100	5.0	116	5.8
tv7	V	217	10.8	227	11.3	256	12.8	326	16.3	377	18.8	490	24.5	533	26.6
tv8	V	328	16.4	334	16.7	345	17.2	337	16.9	331	16.5	344	17.2	356	17.8
tv9	V	365	18.3	337	16.8	324	16.2	266	13.3	217	10.9	174	8.7	205	10.2
tv10	V	386	19.3	415	20.7	472	23.6	608	30.4	734	36.7	1058	52.9	1139	57.0
tv11	V	392	19.6	396	19.8	392	19.6	372	18.6	390	19.5	435	21.8	440	22.0
tv12	V	535	26.8	483	24.1	433	21.7	322	16.1	305	15.2	345	17.2	355	17.7
tv13	V	417	20.8	366	18.3	312	15.6	262	13.1	244	12.2	198	9.9	211	10.5
tv14	V	53	2.7	29	1.5	30	1.5	41	2.0	72	3.6	136	6.8	147	7.4
tv15	V	156	7.8	80	4.0	39	1.9	-38	-1.9	-35	-1.8	23	1.1	41	2.1
tv16	V	-205	-10.3	-198	-9.9	-180	-9.0	-155	-7.7	-120	-6.0	-27	-1.4	-6	-0.3
tv17	V	183	9.2	121	6.0	100	5.0	50	2.5	53	2.7	77	3.9	90	4.5
tv18	V	b/g		b/g		b/g		b/g		b/g		b/g		b/g	
tv19	V	-270	-13.5	-268	-13.4	-263	-13.2	-271	-13.6	-302	-15.1	-381	-19.1	-417	-20.8
tv20	V	-76	-3.8	-64	-3.2	-56	-2.8	-39	-1.9	-34	-1.7	-31	-1.6	-38	-1.9
tv21	V	-615	-30.8	-577	-28.8	-570	-28.5	-578	-28.9	-552	-27.6	-497	-24.9	-514	-25.7
tv22	V	106	5.3	138	6.9	171	8.6	245	12.2	165	8.3	43	2.1	84	4.2
tv23	V	9	0.5	33	1.6	45	2.2	125	6.3	120	6.0	-40	-2.0	-45	-2.3
tv24	V	203	10.2	199	10.0	205	10.2	190	9.5	145	7.3	57	2.8	13	0.6
tv25	V	101	5.0	97	4.8	104	5.2	117	5.9	175	8.7	316	15.8	307	15.4
tv26	V	130	6.5	132	6.6	154	7.7	162	8.1	149	7.5	128	6.4	125	6.3
tv27	V	152	7.6	141	7.0	146	7.3	115	5.8	78	3.9	61	3.1	48	2.4
tv28	V	195	9.7	245	12.2	288	14.4	325	16.3	318	15.9	350	17.5	339	16.9
tv29	V	274	13.7	305	15.2	332	16.6	379	18.9	400	20.0	436	21.8	443	22.1
tv30	V	b/g		b/g		b/g		b/g		b/g		b/g		b/g	
tv31	V	1822	91.1	1902	95.1	1990	99.5	2075	103.8	1973	98.7	790	39.5	b/g	
tv32	V	827	41.4	823	41.2	816	40.8	742	37.1	587	29.4	295	14.8	214	10.7
tv33	V	b/g		b/g		b/g		b/g		b/g		b/g		b/g	
tv34	V	564	28.2	504	25.2	471	23.6	378	18.9	310	15.5	307	15.4	258	12.9
tv35	V	782	39.1	771	38.6	745	37.2	615	30.7	492	24.6	233	11.7	94	4.7

Table F-6. continued .....

		Applied shear stress (MPa) and portion of loading cycle (up = loading cycle, dn = unloading)											
		8.75 up		9.00 up		9.19 up		9.25 up		9.3 pre failur		9.25 post failur	
gauge label	gauge orient. (H or V)	meas. strain (μE)	approx. stress (MPa)	meas. strain (μE)	approx. stress (MPa)	meas. strain (μE)	approx stress (MPa)	meas. strain (μE)	approx. stress (MPa)	meas. strain (μE)	approx stress (MPa)	meas strain (μE)	approx stress (MPa)
th1	H	b/g		b/g		b/g		b/g		b/g		b/g	
th2	H	-17	-0.8	-38	-1.9	-64	-3.2	-74	-3.7	-70	-3.5	-67	-3.4
th3	H	133	6.7	124	6.2	117	5.9	111	5.5	115	5.7	119	6.0
th4	H	118	5.9	114	5.7	106	5.3	104	5.2	111	5.6	124	6.2
th5	H	203	10.1	191	9.6	179	9.0	181	9.1	208	10.4	240	12.0
th6	H	141	7.1	97	4.8	52	2.6	31	1.5	50	2.5	91	4.6
th7	H	48	2.4	-4	-0.2	-64	-3.2	-113	-5.7	-109	-5.5	-66	-3.3
th8	H	935	46.8	1005	50.2	1112	55.6	1226	61.3	1306	65.3	1338	66.9
th9	H	114	5.7	110	5.5	105	5.3	93	4.6	93	4.6	99	5.0
th10	H	152	7.6	154	7.7	155	7.8	155	7.7	155	7.7	152	7.6
th11	H	635	31.7	660	33.0	684	34.2	702	35.1	714	35.7	705	35.3
th12	H	638	31.9	667	33.3	698	34.9	720	36.0	731	36.6	721	36.0
th13	H	933	46.7	1016	50.8	1113	55.7	1158	57.9	1135	56.8	1077	53.8
th14	H	321	16.1	352	17.6	378	18.9	377	18.9	347	17.3	308	15.4
th15	H	444	22.2	479	23.9	504	25.2	511	25.6	503	25.2	472	23.6
th16	H	81	4.1	81	4.1	80	4.0	79	4.0	83	4.2	98	4.9
th17	H	139	6.9	139	6.9	145	7.3	156	7.8	156	7.8	154	7.7
th18	H	91	4.5	85	4.3	83	4.2	78	3.9	94	4.7	114	5.7
th19	H	-65	-3.3	-71	-3.5	-70	-3.5	-64	-3.2	-60	-3.0	-29	-1.5
th20	H	-94	-4.7	-100	-5.0	-99	-5.0	-103	-5.1	-106	-5.3	-120	-6.0
th21	H	57	2.9	57	2.9	56	2.8	55	2.7	59	2.9	58	2.9
th22	H	354	17.7	352	17.6	446	22.3	602	30.1	726	36.3	711	35.6
th23	H	b/g		b/g		b/g		b/g		b/g		b/g	
th24	H	422	21.1	449	22.5	528	26.4	784	39.2	735	36.7	361	18.1
th25	H	b/g		b/g		b/g		b/g		b/g		b/g	
th26	H	-420	-21.0	-292	-14.6	-193	-9.7	-124	-6.2	-290	-14.5	-695	-34.8
th27	H	-252	-12.6	-258	-12.9	-276	-13.8	-307	-15.4	-358	-17.9	-405	-20.2
th28	H	-109	-5.4	-121	-6.0	-133	-6.7	-158	-7.9	-192	-9.6	-220	-11.0
tv1	V	191	9.5	191	9.5	186	9.3	186	9.3	182	9.1	201	10.1
tv2	V	-264	-13.2	-264	-13.2	-261	-13.1	-261	-13.1	-269	-13.4	-281	-14.0
tv3	V	362	18.1	393	19.6	414	20.7	410	20.5	353	17.7	222	11.1

Table F-6. continued .....

		Applied shear stress (MPa) and portion of loading cycle (up = loading cycle, dn = unloading)											
		8.75 up		9.00 up		9.19 up		9.25 up		9.3 pre failur		9.25 post failur	
gauge label	gauge orient. (H or V)	meas. strain (μE)	approx. stress (MPa)	meas. strain (μE)	approx. stress (MPa)	meas. strain (μE)	approx. stress (MPa)	meas. strain (μE)	approx. stress (MPa)	meas. strain (μE)	approx. stress (MPa)	meas. strain (μE)	approx. stress (MPa)
tv4	V	236	11.8	236	11.8	243	12.2	243	12.1	247	12.3	266	13.3
tv5	V	497	24.9	505	25.3	516	25.8	523	26.2	520	26.0	500	25.0
tv6	V	127	6.4	142	7.1	153	7.7	157	7.8	138	6.9	72	3.6
tv7	V	579	28.9	625	31.2	678	33.9	705	35.2	686	34.3	547	27.4
tv8	V	371	18.6	387	19.3	394	19.7	397	19.9	401	20.1	455	22.7
tv9	V	236	11.8	255	12.7	319	16.0	357	17.9	404	20.2	380	19.0
tv10	V	1189	59.5	1262	63.1	1353	67.7	1411	70.5	1377	68.8	1023	51.2
tv11	V	452	22.6	465	23.3	474	23.7	473	23.7	446	22.3	415	20.7
tv12	V	374	18.7	390	19.5	404	20.2	407	20.4	365	18.2	330	16.5
tv13	V	230	11.5	238	11.9	228	11.4	210	10.5	183	9.2	167	8.3
tv14	V	167	8.4	188	9.4	204	10.2	204	10.2	181	9.0	146	7.3
tv15	V	65	3.2	88	4.4	102	5.1	82	4.1	24	1.2	-8	-0.4
tv16	V	17	0.8	40	2.0	57	2.9	48	2.4	6	0.3	-48	-2.4
tv17	V	98	4.9	108	5.4	111	5.5	107	5.3	95	4.8	84	4.2
tv18	V	b/g		b/g		b/g		b/g		b/g		b/g	
tv19	V	-458	-22.9	-499	-24.9	-576	-28.8	-654	-32.7	-689	-34.4	-702	-35.1
tv20	V	-41	-2.1	-43	-2.2	-47	-2.4	-53	-2.7	-57	-2.8	-61	-3.1
tv21	V	-528	-26.4	-542	-27.1	-572	-28.6	-619	-30.9	-669	-33.4	-686	-34.3
tv22	V	99	5.0	128	6.4	151	7.6	137	6.9	95	4.7	62	3.1
tv23	V	-49	-2.5	-43	-2.2	-39	-2.0	-39	-2.0	-39	-2.0	-37	-1.9
tv24	V	13	0.6	13	0.6	6	0.3	9	0.5	21	1.0	12	0.6
tv25	V	303	15.2	317	15.8	332	16.6	333	16.7	314	15.7	347	17.3
tv26	V	129	6.5	131	6.6	135	6.8	128	6.4	113	5.6	130	6.5
tv27	V	36	1.8	36	1.8	42	2.1	47	2.3	58	2.9	55	2.7
tv28	V	320	16.0	324	16.2	332	16.6	344	17.2	340	17.0	377	18.9
tv29	V	435	21.7	443	22.1	460	23.0	460	23.0	453	22.7	488	24.4
tv30	V	b/g		b/g		b/g		b/g		b/g		b/g	
tv31	V	b/g		b/g		b/g		b/g		b/g		b/g	
tv32	V	160	8.0	79	4.0	-12	-0.6	9	0.5	55	2.8	67	3.3
tv33	V	b/g		b/g		b/g		b/g		b/g		b/g	
tv34	V	270	13.5	277	13.9	303	15.2	291	14.5	35	1.8	-51	-2.6
tv35	V	1	0.1	-97	-4.9	-108	-5.4	-62	-3.1	-62	-3.1	-93	-4.6